FIRST-PRINCIPLES STUDIES OF NUCLEATION OF ATOMIC-LAYERED MOLYBDENUM DISULFIDE BY ATOMIC LAYER DEPOSITION

by

Matthew Lawson

A dissertation

submitted in partial fulfillment

of the requirements for the degree of

Doctor of Philosophy in Materials Science and Engineering

Boise State University

May 2021

BOISE STATE UNIVERSITY GRADUATE COLLEGE

DEFENSE COMMITTEE AND FINAL READING APPROVALS

of the dissertation submitted by

Matthew Lawson

Dissertation Title: First-Principles Studies of Nucleation of Atomic-Layered Molybdenum Disulfide by Atomic Layer Deposition

Date of Final Oral Examination: 25 March 2021

The following individuals read and discussed the dissertation submitted by student Matthew Lawson, and they evaluated the student's presentation and response to questions during the final oral examination. They found that the student passed the final oral examination.

Lan Li, Ph.D.	Co-Chair, Supervisory Committee
Elton Graugnard, Ph.D.	Co-Chair, Supervisory Committee
Dave Estrada, Ph.D.	Member, Supervisory Committee
Winnie Wong-Ng, Ph.D.	Member, Supervisory Committee

The final reading approval of the dissertation was granted by Lan Li, Ph.D. and Elton Graugnard, Ph.D., Co-Chair of the Supervisory Committee. The dissertation was approved by the Graduate College.

DEDICATION

I dedicate this dissertation to my parents, Doug and Pat. I love you both, and I know without your support and words of encouragement during trying times, I would not have had nearly the same success. The love you two share is what I aspire to, and this dissertation is a token of thanks for the incredible job you two did as parents. Of course, Jono, you are part of this dissertation as well. Don't worry, seeing you develop into a professional, while I became an academic, pushed me harder than anything to compete with you like we always do. Finally, this dissertation would not have been possible without the consistent and constant feedback from my best friend, Charles. I love all of you so much.

ACKNOWLEDGMENTS

There are a tremendous number of people I would like to thank and appreciate during my academic journey. To start, Boise State University has always treated me with the ultimate respect and dignity, and I have experienced some of my fondest memories in "The City of Trees". The Micron School of Materials Science and Engineering has provided me with a world-class education, as well as exposed me to many faculty and staff that have not only broadened my knowledge but have built me up as a person.

First and foremost, I want to acknowledge my advisor Dr. Lan Li. I am eternally grateful that you took to a chance on a kid out of college who might not have boasted the most impressive GPA. Between working in your lab as an undergraduate and graduate student, you have taught me how to be persistent, critical, and more than a researcher. I have learned how to challenge myself through you, and have realized that the only challenge in life, is yourself stopping you. Your work ethic and compassion for your students is felt, and I am ever-so thankful for allowing me to take this incredible journey. During my entire time as a graduate career, I always felt as if you were in my corner, ready to fight for me and with me. Thank you so much for not only being my advisor, but for being someone in my life who I will always look up to.

I also want to thank the members of my committee for all the effort they have put into my dissertation. Especially, Dr. Elton Graugnard. Elton, I have never met someone who thinks so critically and deeply about complex topics. You have made me think so deeply my head hurts, and I have loved every moment of that. During all my research,

you never once settled for a simple answer I gave you, and I cannot express how important that became during my last years as a graduate student. You forced me to step outside my academic comfort zone and think incredibly critically of not only my work but the importance of my work. You have helped me realize that research is just the steppingstone to greater things in life. Thank you for all the time and effort gave to me. Third, I want to thank Dr. Winnie Wong-Ng at the National Institute for Standards and Technology (NIST) for all the collaborations with our group at Boise State University. The work we did together has opened opportunities that I could not have had without you. Thank you for being patient with me, especially when I was a young graduate student! I would like to also thank and acknowledge Dr. Dave Estrada for all the time he has poured into my proposal and dissertation.

Next, I want to extend my thanks to Jake Soares as my experimental compadre. It has been so enjoyable working with you and getting to know you as a friend. I think we are finally getting good at ALD! I want to thank the group members of the Materials Theory and Modeling Group. It's been a journey with all of you, and I am proud of all the great work done in our group. Thank you, Izaak Williamson, for showing me how to be a successful graduate student, thank you, Thiago Henrique da Silva and Ember Sikorski, for growing as graduate students with me, and thank you, German Barcenas and Austin Biaggne, for taking the baton. Great things await all of us! I want to thank Jessica Economy for all the guidance through graduate school and talks about life post-graduation. Jamie Hayward, you've been a great friend and you always managed to make me smile during any of the difficult days. Finally, I thank all the incredible people that have become family to me in Boise. Dustin, Cam, Adam, Kody, Dillon, Max, Christian,

and the list goes on. Whenever times in graduate school were tough, I have always been able to lean on all of you.

This work made use of the resources of the High Performance Computing Center at Idaho National Laboratory, which is supported by the Office of Nuclear Energy of the U.S. Department of Energy and the Nuclear Science User Facilities under Contract No. DE-AC07-05ID14517. We would also like to acknowledge high-performance computing support of the R2 compute cluster (DOI: 10.18122/B2S41H) provided by Boise State University's Research Computing Department. This work was supported in part by an NSF CAREER Grant No. 1751268

ABSTRACT

This dissertation implements first-principles calculations to understand the nucleation mechanisms for atomic layer deposition (ALD) of molybdenum disulfide (MoS_2) using MoF_6 and H_2S precursors. ALD is a self-limiting process that can deposit a range of materials at the nanoscale, while maintaining chemical stoichiometry, atomic scale thickness control, and can conform to high-aspect ratio substrate designs. ALD is extremely sensitive to surface chemistry and morphology; therefore, it is critical to understand how these factors control deposition.

Density functional theory (DFT) was used to understand what factors can control the nucleation for ALD of MoS_2 using MoF_6 and H_2S. Surface hydroxyls on oxide substrates help facilitate the formation of ionic MF_x (M = metal, x = 1, 2, 3) species, which thermodynamically drive the first-half cycle of ALD. DFT calculations were supported by experimental measurements to validate computational predictions. DFT and experiment both confirmed that there are different types of nucleation mechanisms during ALD of MoS_2. The types of mechanisms depend on which precursor is introduced, and highlights the complexities during nucleation of MoS_2 during ALD.

TABLE OF CONTENTS

LIST OF TABLES

LIST OF FIGURES

LIST OF ABBREVIATIONS

BSU	Boise State University
GC	Graduate College
TDC	Thesis and Dissertation Coordinator
ALD	Atomic layer deposition
MoS_2	Molybdenum disulfide
DFT	Density functional theory
m	Meter
nm	Nanometer
ICs	Integrated circuits
MoF_6	Molybdenum hexafluoride
H_2S	Hydrogen sulfide
TMDs	Transition metal dichalcogenides
2D	Two-dimensional
CVD	Chemical vapor deposition
Al_2O_3	Alumina oxide
HfO_2	Hafnium oxide
MgO	Magnesium oxide
OH	Hydroxyl groups
AlF_x	Aluminum fluoride compound
QCM	Quartz crystal microbalance

XPS	X-ray photoelectron spectroscopy
RGA	Residual gas analysis
eV	Electronvolt
GPa	Gigapascal
PVD	Physical vapor deposition
FTIR	Fourier transform infrared spectroscopy
HF	Hartree-Fock
LDA	Local density approximation
GGA	Generalized gradient approximation
PAW	Projected-augmented wave
E_{cutoff}	Cutoff energy
PBC	Periodic boundary conditions
k	Wave vector
G	Reciprocal-space
DoS	Density of states
LDoS	Local density of states
GPC	Growth per cycle
FETs	Field effect transistors
VASP	Vienna ab initio Software Package
PBE	Perdew-Burke-Ernzerhof
DFPT	Density functional perturbation theory
DFT + U	Density functional theory with Hubbard U correction
AGF	Atomistic Green's Function

$\Theta(\omega)$	Transmission function
TBC	Thermal boundary conductance
THz	Terahertz
ZnO	Zirconium oxide
TMA	Trimethylaluminum
C	Celsius
cm	Centimeter
mTorr	Millitorr
OMS	Octahedral molecular sieve
CO_2	Carbon dioxide
NIST	National Institute for Standards and Technology
MOF	Metal organic framework
TiO_2	Titanium dioxide

CHAPTER ONE: INTRODUCTION, MOTIVATION, AND SIGNIFICANCE OF DISSERTATION

1.1 Goal of This Dissertation

The project goal is to validate the hypothesis that surface chemistry and atomic-scale morphology can control the nucleation mechanism during the atomic layer deposition (ALD) of thin films used in electronic devices. Specifically, I aim to uncover what specific factors control nucleation during the first two half-cycles for ALD of MoS_2 using MoF_6 and H_2S. Although it is widely known that surface chemistry and morphology are crucial to ALD, their exact role remains unclear, such as how surface chemistry and morphology control ALD, and how these factors can be leveraged to improve the quality of films deposited. In addition, the details of the chemical reaction processes involved are not always clear, thus, the goal of this project is to use computational modeling methods to fully address those issues.

Thin films are classified by their thickness, ranging from one micron (10^{-6} m) to one nanometer (10^{-9} m). Depositing thin films is one cornerstone of electronic device manufacturing, because it facilitates the miniaturization of integrated circuits (ICs). For successful fabrication of ICs thin film deposition must be a repeatable process with little materials property variation. The ALD technique this project focuses on explores the nanometer length scale. Specifically, molybdenum disulfide (MoS_2) is grown by molybdenum hexafluoride (MoF_6) and hydrogen sulfide (H_2S) precursors using ALD. First-principles density functional theory (DFT)-based methods can explore the

nucleation mechanism of MoS_2, which is not easily observed *in-situ*. Understanding the controlling factors of nucleation mechanisms during ALD could provide the necessary insights to achieve higher quality films and enable the integration of the MoS_2 ALD process within the microelectronics industry.

1.2 Background and Motivation

The global economy is intertwined with the semiconductor industry and directly linked to technological advances. Moore's law retains that the number of transistors on an IC doubles every two years[1] and can be correlated to MOSFET scaling[2]. In 1971, the minimum feature size, or process node, was 10μm, and almost 50 years later in 2020 the minimum feature size had shrunk to 7nm[3]. This exponential decrease in minimum feature size has two-fold effects. Firstly, it allows for more complicated ICs that can outperform previous generations. Secondly, it decreases manufacturing cost while the amount of computer memory increases. The next set of challenges is to precisely manufacture high quality thin films at the nanoscale. Graphene is a 2D-material that sparked great interest in the scientific community when it was first synthesized, however, there are several drawbacks. Firstly, graphene possesses an applicable carrier mobility, however, the lack of a bandgap makes it not useable for field effect transistors[4]. Secondly, graphene can be oxidized into graphene oxide when it is exposed to oxygen and heat, which could destroy the advantageous properties[5,6]. Thirdly, graphene is toxic to humans due to the nature of its nanoscale-sharp edges that will tear cell membranes[7,8]. For these reasons, new 2D materials are of great research interest. Transition metal dichalcogenides (TMDs) have a composition MX_2 (M = transition metal, X = chalcogen), with a range of band gaps[9] between 0-2 eV[10]. As seen in Figure 1.1 the transition metal atoms are sandwiched

between two hexagonal sheets of chalcogens resulting in strong covalent bonding within an atomic trilayer, while out-of-plane sheets are held together by weak van der Waals bonds. This unique bonding structure also creates novel properties in the transition from bulk to monolayer[9,11]. Table 1.1 contains a short list of commonly synthesized bulk and 2D-TMDs with applications in semiconducting manufacturing. The MoX_2 and WX_2 (X = S, Se, or Te) TMDs families excellently illustrate the unique shifts in electronic band gaps when transitioning from bulk to monolayer.

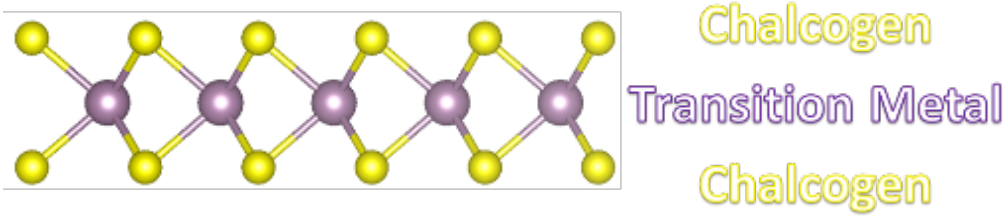

Figure 1.1. Cross-section of a 2D-TMDs where the yellow atoms are chalcogens that sandwich a purple-colored transition metal.

Table 1.1. Two commonly studied TMD compounds MoX_2 and WX_2 with the band gaps in the bulk and monolayer phases[10].

Bulk TMDs	Band Gap (eV)	Monolayer TMDs	Band Gap (eV)
MoS_2	1.2	2D-MoS_2	1.8
$MoSe_2$	1.1	2D-$MoSe_2$	1.5
$MoTe_2$	1.0	2D-$MoTe_2$	1.1
WS_2	1.4	2D-WS_2	1.9
WSe_2	1.2	2D-WSe_2	1.7

Atomic layer deposition is a rapidly growing field that has potential applications in a variety of industries, including but not limited to, electronics manufacturing, energy/battery applications, optical applications, and more. This range of applications

stems from the variety of materials that can be deposited with precise sub-nanometer thickness control. The lower operating temperatures of ALD also allow for easier industrial integration in comparison with traditional chemical vapor deposition (CVD). The first successful ALD experiment occurred in the 1960's by Professor Kol'tsov, and was labeled as "molecular layering"[12]. Since then, the number of ALD studies relative to other deposition techniques remained quite low until 2001. Improvements in ALD equipment and techniques lead to an exponential growth in the number of ALD articles after 2001, as well as number of new authors. In 2018 Alvaro and Yanguas-Gil established that over 11,000 ALD articles have been published due to the work of over 21,500 scientists[12]. During this period, the types of films deposited ranged from oxides to chalcogenides, to metals, and semiconductors, which highlighted the potential for ALD. Specifically, selective-area ALD where substrates could be patterned to deposit specific material on a selective part of the substrate, has become a common method for thin film deposition.

1.3 Research Significance

There are important scientific questions that need to be answered on how nucleation is initiated during ALD. Work needs to be done to understand how surface chemistry can be leveraged to control the deposition process. This would facilitate more ALD of nanoscale semiconducting films and drive the production of the next generation of transistors, memristors, memory arrays, and more. As device manufacturing becomes increasingly smaller the nucleation phase of ALD will begin to dictate device performance. Furthermore, the self-limiting nature of ALD is highly attractive for coating surfaces and features that possess high aspect ratios. Self-limiting deposition alleviates

the mechanical stresses on nanoscale features and ensures uniform deposition. As device manufacturing becomes more architecturally complex, advanced methods like ALD are a viable solution.

This dissertation explores the nucleation process during ALD of MoS_2 using first-principles methods. DFT-based calculations coupled with experiments reveal critical phenomena during deposition, specifically the nucleation mechanics for ALD of 2D-MoS_2. The DFT results also provide insight into how nucleation can be controlled on the atomic scale.

1.4 Dissertation deliverables

This dissertation has four Objectives, discussed in detail below. Chapter 2 of this dissertation contains a literature review of MoS_2 compounds and the ALD process. Chapter 3 explains first-principles method. Chapter 4 is my published work on 2D-TMD lateral heterojunctions, and how small compressive and tensile forces can alter the electrical and thermal properties of 2D-TMDs. Chapter 4 highlights the important relationship between processing and properties. The subsequent chapters address the deliverables of this dissertation as follows:

- **Objective 1:** Determine the effects of surface chemistry and morphology on nucleation of MoF_6 on oxide surfaces

Identifying the effects of different surface chemistries and morphologies is the primary work of this dissertation, because it helps identify which surface chemistries and morphologies could improve or hinder MoF_6 deposition. Coupling reactive and non-reactive surfaces during ALD could be used for area-selective ALD, which is an increasing area of study for additional control over film deposition in complex device structures. Chapter 5 discusses how surface chemistry and morphology change between

Al_2O_3, HfO_2, and MgO oxide substrates. Fully hydroxylated oxide surfaces are compared with non-hydroxylated counterparts. We found that hydroxyl groups (OH) can control deposition on each oxide. The findings indicate there is a significant difference between oxide surface chemistries, while OH groups on the oxide surfaces could improve the reactivity of the substrates. Furthermore, OH groups help facilitate chemical bonds between each surface and an MoF_6 precursor. Without the OH groups weak van der Waals bonds are found. The difference between hydroxylated and non-hydroxylated oxide surfaces may provide a path for area-selective deposition. The presence of hydroxyl groups could ultimately dictate nucleation. The findings in Chapter 5 support the hypothesis of this project that surface chemistry dictates deposition. Further studying how the OH groups facilitate deposition is also crucial. Chapter 6 of this dissertation explores how the OH concentration on Al_2O_3 controls the ALD process of MoS_2. We found that the OH groups alter the surface chemistry by attacking the Al-O bonds, resulting in the formation of AlF_x (x = 1, 2, etc.) bonds. Our results suggested that OH surface chemistry might be able to control deposition.

- **Objective 2:** Explore multiple precursors reacting on the surface

There have been very few DFT studies clearly addressing the deposition of multiple MoF_6 precursors on a surface. Chapter 6 of the dissertation presents an Al_2O_3 surface fully saturated with multiple MoF_6 precursors. A variety of AlF_x (x = 1, 2, etc) bonds are formed between the precursors and Al_2O_3 surface. The analysis of charge density difference allows us to further quantify those chemical interactions.

- **Objective 3:** Validate DFT predictions with experimental measurements

Combining DFT and experimental measurements not only validate the DFT predictions but also provide detailed insight into experimental observations, such as the

initial stage of nucleation of MoS_2.Chapter 6 presents experimental measurements, performed by Jake Soares and supervised by Dr. Elton Graugnard, in couple with DFT calculations. Quartz crystal microbalance (QCM), x-ray photoelectron spectroscopy (XPS), and residual gas analysis (RGA) were combined with DFT calculations to understand the bonding characteristics between MoF_6 molecules hydroxylated Al_2O_3 substrate. Bond lengths were measured using DFT and the Bader charges were calculated to correlate with experimental measurements.

- **Objective 4:** Determine controlling factors and propose nucleation mechanism based on DFT and experimental studies

  Chapter 6 proposes that the first half-cycle of MoF_6 does not follow a ligand-exchange mechanism. The DFT calculations suggested highly ionic AlF_3 formed at the Al_2O_3 surface and no gaseous byproducts formed during the first half-cycle. Residual gas analysis (RGA) data identified H_2O byproducts, but no gas phase HF. The lack of HF byproducts during the first half-cycle for ALD of MoS_2 confirms our hypothesis that the MoF_6 precursor on an Al_2O_3 substrate does not follow a typical ligand-exchange process. We suggest that during the first half-cycle of MoF_6 the precursor undergoes a dissociation chemistry, instead of a ligand-exchange mechanism. This is interesting, because during the growth regime for ALD of MoS_2 the ligand-exchange occurs. We observe two different nucleation mechanisms during the ALD of MoS_2. Chapter 6 also discusses the second half-cycle for ALD of MoS_2. Reaction barriers for H_2S deposition were calculated to understand how S bonds to the film and the required activation energies were calculated.

Finally, chapter 7 summaries the results of the studies reported in this dissertation and offers suggestions for future work aimed toward gaining further understanding of nucleation and growth of 2D materials deposited by ALD.

References

1 Gordon E Moore, (McGraw-Hill New York, NY, USA:, 1965).

2 Kostas Siozios, Dimitrios Anagnostos, Dimitrios Soudris, and Elias Kosmatopoulos, *IoT for Smart Grids*. (Springer, 2019).

3 Sal Dasgupta, Teja Singh, Ashish Jain, Samuel Naffziger, Deepesh John, Chetan Bisht, and Pradeep Jayaraman, presented at the 2020 IEEE International Solid-State Circuits Conference-(ISSCC), 2020 (unpublished).

4 AH Castro Neto, Francisco Guinea, Nuno MR Peres, Kostya S Novoselov, and Andre K Geim, Reviews of modern physics **81** (1), 109 (2009).

5 Karin Gotterbarm, Wei Zhao, Oliver Höfert, Christoph Gleichweit, Christian Papp, and Hans-Peter Steinrück, Physical Chemistry Chemical Physics **15** (45), 19625 (2013).

6 Elena Starodub, Norman C Bartelt, and Kevin F McCarty, The Journal of Physical Chemistry C **114** (11), 5134 (2010).

7 Omid Akhavan and Elham Ghaderi, ACS nano **4** (10), 5731 (2010).

8 Kai Yang, Yingjie Li, Xiaofang Tan, Rui Peng, and Zhuang Liu, Small **9** (9-10), 1492 (2013).

9 Qing Hua Wang, Kourosh Kalantar-Zadeh, Andras Kis, Jonathan N Coleman, and Michael S Strano, Nature nanotechnology **7** (11), 699 (2012).

10 A. Chaves, J. G. Azadani, Hussain Alsalman, D. R. da Costa, R. Frisenda, A. J. Chaves, Seung Hyun Song, Y. D. Kim, Daowei He, Jiadong Zhou, A. Castellanos-Gomez, F. M. Peeters, Zheng Liu, C. L. Hinkle, Sang-Hyun Oh, Peide D. Ye, Steven J. Koester, Young Hee Lee, Ph Avouris, Xinran Wang, and Tony Low, npj 2D Materials and Applications **4** (1), 29 (2020).

[11] Manish Chhowalla, Hyeon Suk Shin, Goki Eda, Lain-Jong Li, Kian Ping Loh, and Hua Zhang, Nature chemistry **5** (4), 263 (2013).

[12] Elsa Alvaro and Angel Yanguas-Gil, Plos one **13** (1), e0189137 (2018).

CHAPTER TWO: MOLYBDENUM DISULFIDE AND DEPOSITION PROCESSES

2.1 Molybdenum Disulfide

2.1.1 Bulk Phase Molybdenum Disulfide

Molybdenum disulfide (MoS_2) naturally occurs as the mineral molybdenite[1] and is comprised of molybdenum atoms sandwiched between two layers of sulfur atoms. MoS_2 in Figure 2.1 is a layered structure with strong in-plane covalent bonds between the S-Mo-S atoms, and weaker van der Waals bonding between the layers.

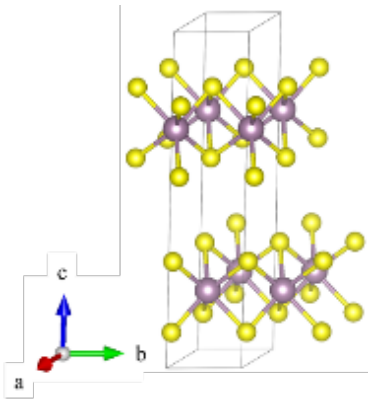

Figure 2.1. Bulk MoS_2 where the yellow atoms are S and the purple atoms are Mo. A unit cell for the trigonal prismatic 2H phase of bulk MoS_2 is shown.

This unique bonding structure allows the mineral to be easily flaked and used as a lubricant. Bulk phase MoS_2 is a diamagnetic semiconductor with an indirect band gap of 1.3 eV[2-4], and can be found in two separate crystalline phases. The first phase is 2H-MoS_2 where the crystal structure is $P6_3/mmc$, while the second phase is 3R-MoS_2 with a crystal structure of R3m (where H = hexagonal and R = rhombohedral). Like graphene, mechanical exfoliation techniques can separate the weakly bound van der Waals forces

between the layered S-Mo-S structures, leading to the driving motivation to form free-standing single-layered MoS_2.

2.1.2 Two-Dimensional Molybdenum Disulfide

This project focuses on two-dimensional (2D) MoS_2 due to a wide range of its novel properties. Single-layered MoS_2, or 2D MoS_2 was first synthesized in 2010 by Mak *et al.*[5] by mechanical exfoliation. Radisavljevic *et al*. later demonstrated MoS_2 possessing a mobility large enough for practical application and similar to that of graphene[6]. First-principles calculations predicted a shift in band structure when transitioning from bulk to monolayer. In bulk MoS_2, there is an indirect band gap transition of 1.2 eV. In monolayer MoS_2 there is a direct transition of 1.8 eV at the K-point. The indirect-to-direct band gap transition plays an important role in the optical and electrical properties of 2D-MoS_2. For example, in bulk phase MoS_2 photoluminescence is negligible, but at reduced dimensionality strong photoluminescence is observed[7]. Quantum confinement of electrons in 2D-MoS_2 affects the electrical properties by resulting in direct-band exitonic transitions[8] as well as an improvement in the electron mobility. Spatial confinement at low dimensionalities also alters thermal transport properties by restricting phonon vibration modes in-plane. In addition, 2D-MoS_2 also possesses exceptional mechanical properties. Defect-free monolayer MoS_2 has demonstrated a Young's modulus of 270 GPa, which is higher than stainless steel (205 GPa)[9]. All the properties discussed above are dominated by the dimensionality of MoS_2. 2D-MoS_2 requires an extremely precise deposition technique to capture and leverage these novel properties at the reduced dimensionalities. Therefore, it is imperative to control the deposition and nucleation of low dimensional MoS_2 during ALD to maintain these advantageous materials properties.

2D-MoS_2 can be found in two crystal phases of 2H (P63/*mmc* space group)[10] or 1T (P$\bar{3}$*m*1 space group)[11], as seen in Figure 2.2. The properties of 2D-MoS_2 depend on its crystal structure and symmetry. The 2H phase of 2D-MoS_2 has a direct band gap of 1.8 eV, while the 1T phase is metallic. The crystal structure of 2D-MoS_2 will dictate the application of the material. If a device is expecting the semiconducting 2H phase of MoS_2 but metallic 1T is deposited instead, that will be detrimental for many device performances. For this specific reason, it is imperative to know how to deposit or grow the appropriate crystal structure of 2D-MoS_2 in order to maintain its semiconducting properties. The transition to a direct band gap semiconductor of 1.8 eV at low dimensions provides a wealth of new properties when compared to its bulk phase, resulting in a wide range of applications[12], such as electrocatalysis[13-16], photocatalysis[17-20], batteries[21-24], biological applications[25-28], sensors[29-34], and electronic devices[4,35-38].

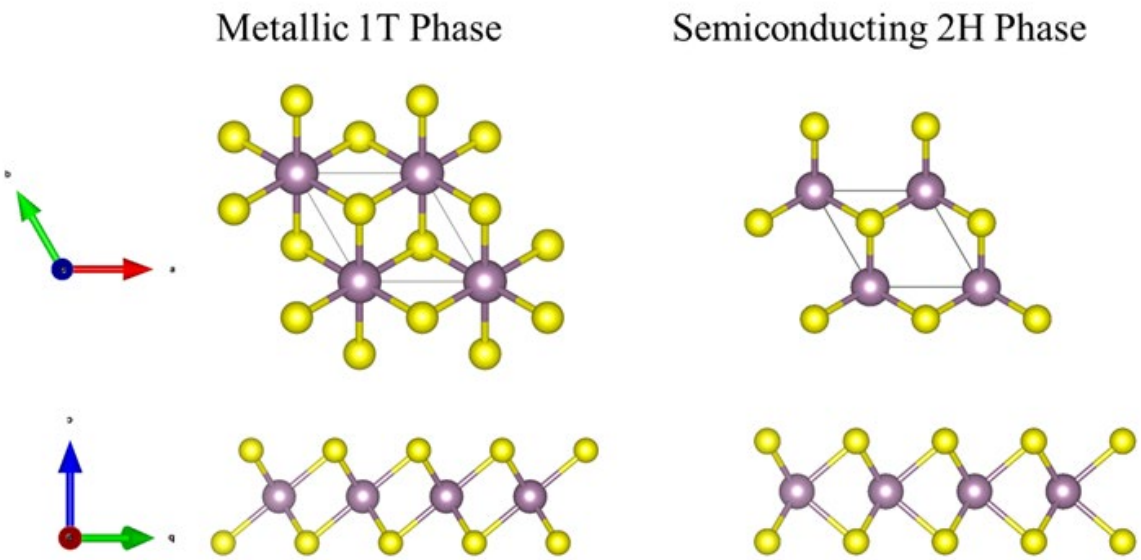

Figure 2.2. Two different crystal phases of 2D-MoS_2. The left phase is semiconducting 2H (P63/*mmc* space group) and the right is metallic 1T (P$\bar{3}$*m*1 space group).

2.2 Deposition Techniques for 2D-MoS_2

There are several methods to prepare 2D-MoS_2 such as mechanical exfoliation, liquid exfoliation, chemical vapor deposition (CVD), and atomic layer deposition (ALD). Table 2.1 contains a quick synopsis of the advantages and disadvantages for each method used to synthesize 2D-MoS_2. The following sections will elaborate on each of these fabrication techniques.

Table 2.1 The various advantages and disadvantages of fabricating 2D-MoS_2 with different deposition processes.

Deposition	Fabrication Type	Advantages	Disadvantages
Exfoliation (liquid and mechanical)	Top-down	Cheap, relatively defect free[36]	Low yield, not integrated process[5]
CVD	Bottom-up	High deposition rate, high quality film, integrated process[42-44]	Vulnerable to substrate features, high operation temperatures, continuous growth mode[46-47]
ALD	Bottom-up	Atomic precision, conformality, low temperature, self-limiting growth mode[42-44]	Growth mechanisms still under investigation[46-47]

2.2.1 Mechanical and Liquid Exfoliation

Both mechanical and liquid exfoliation are forms of top-down fabrication processes because they are subtractive techniques where material is removed to obtain a desired size and shape. Mechanical exfoliation is a proven and effective method for generating high-quality free-standing graphene[39]. This is done by placing a piece of graphite on an adhesive tape, folding the tape over on itself, and rubbing the folded tape

to generate friction. The shear force generated by this friction is enough to cleave graphene flakes held together by the weak van der Waals forces between the graphite layers. This same process is adopted for 2D-MoS_2[5], and adaptations and improvements of the process result in high-quality 2D-MoS_2 with limited defects[36]. Liquid exfoliation operates in slightly different fashion. Bulk MoS_2 is suspended in a liquid solution and then sonicated, and the dispersions are put in a centrifuge and 2D-MoS_2 is then extracted[40]. Both liquid and mechanical exfoliation can generate large, relatively defect free, sheets of 2D-MoS_2. However, the yield of these processes is relatively low, making both exfoliation techniques difficult to implement in large-scale 2D-MoS_2 manufacturing.

2.2.2 Chemical Vapor Deposition

Chemical vapor deposition (CVD) is a bottom-up fabrication technique because atoms and molecules are assembled on a surface to generate a new material. Unlike physical vapor deposition (PVD) techniques that use evaporation or sputtering, CVD is a chemically driven process. Films are grown by chemical reactions that occur at and above the substrate. When compared to PVD, CVD has a higher deposition rate and ability to operate at lower vacuum levels[41]. CVD operates as follows: (1) transporting precursors to substrate, (2) transporting reactants from main gas stream though the boundary layer to the substrate surface, (3) substrate adsorbs precursors, (4) chemical reactions between the precursors and substrate, (5) deposition of by-products, (6) transport of excess and un-needed by-products away from substrate. Steps (2) through (5) are the most important for determining deposition rate.

The driving force for CVD is to reach some state of chemical equilibrium where the concentrations of each chemical species is constant, and temperature plays a critical

role to reach this equilibrium. The substrate must provide enough thermal energy to overcome the activation energy barrier that initiates the chemical reactions between the gas phase precursors. 2D-MoS_2 has been grown via CVD, but the high substrate temperatures[42-44] (over 400^o C) are beyond the operation temperatures of any "Back End of The Line" applications[45]. The disadvantages of CVD are not only high operation temperature but also the lack of self-limiting growth,[46,47] providing unwanted challenges during fabrication. These two reasons lead further investigation of an alternative process – atomic layer deposition (ALD). ALD is a subset of CVD that alleviates some issues associated with CVD.

2.3 ALD Process

ALD exploits the volatility of gas phase precursors to deposit a range of thin films on a variety of substrates. Although both ALD and CVD are conducted in a chamber under vacuum with a heated substrate, unlike CVD, the gas phase precursors used for ALD are never mixed simultaneously in the reactor and are introduced in a sequential fashion[48]. A typical ALD workflow is modeled in Figure 2.3 using example precursors A and B. Precursor A is introduced into the chamber for a preprogramed amount of time and it reacts with the surface. When all the available surface sites are satisfied, the reactions terminate and the film growth stops. This results in uniform and conformal thin films with atomic thickness control. Purge cycles are required to remove the byproducts between each precursor pulse. Excess Precursor A molecules that do not react with the surface are also removed during this purge cycle. This completes the first half-cycle of ALD. The second half-cycle begins by introducing Precursor B into the chamber. Precursor B undergoes the same process as Precursor A and creates its own unique

surface. The self-limiting chemical reactions of the precursors limit the growth during the cycles, and results in precise atomic layer control. Figure 2.3 depicts the ALD process modelled by two half-reactions created by each precursor and its respective surface. These two half-reactions are the focus of this dissertation.

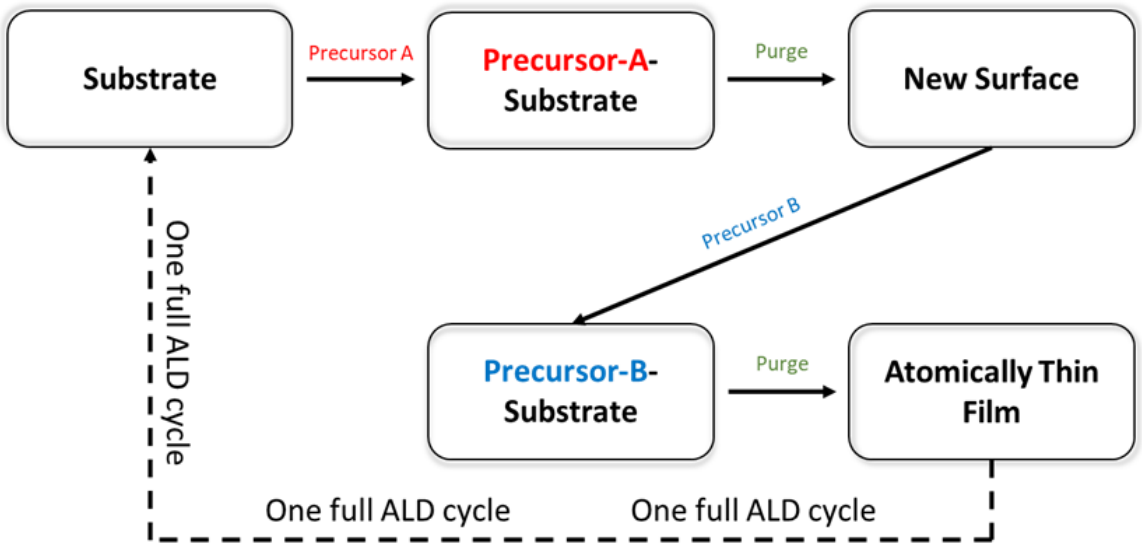

Figure 2.3. A full ALD cycle starts with a bare substrate and is exposed precursor-A. Once the all the available surface sites have been satisfied a purge step removes excess precursors and hazardous byproducts. The newly deposited film serves as the substrate for precursor-B, and the reactions ensue until all reaction sites are satisfied. Another purge step begins to remove excess precursor and byproduct. This process represents one full ALD cycle.

2.3.1 *In-Situ* Measurements

There are several methods to study ALD *in-situ*, including but not limited to quartz crystal microbalance (QCM), residual gas analysis (RGA), Fourier transform infrared spectroscopy (FTIR), and x-ray photoelectron spectroscopy (XPS). Our experimental collaborators combine these different methods during ALD for process characterization and development. QCM measures the mass change during deposition. When mass deposits on the QCM this registers a change in frequency of a quartz resonator and can be correlated to mass change in an area during *in-situ* ALD. The

growth per cycle (GPC) is calculated using QCM and can determine if self-limiting growth has been achieved. Figure 2.4 demonstrates the temperature sensitive "ALD window" and the importance of calculating the GPC. At both low and high temperatures ALD will not be constant. The blue region in Figure 2.4 is the "ALD growth window," where deposition remains constant and self-limiting. QCM is specifically used to calculate the GPC to ensure that self-limiting growth is achieved, and self-limiting growth is foundational for ALD.

Another *in-situ* method used to understand ALD is RGA. RGA is an apparatus attached an end of a chamber that captures byproducts and excess precursors at the end of each half-cycle. The RGA employs mass spectrometry and measures the mass to charge ratio of gas phase molecules. This is useful for ALD, because based on the masses and charges of the collected gaseous species, reaction equations can be constructed. Possible reaction pathways can be predicted. Complementary to RGA, surface FTIR is another diagnostic tool that provides chemical information for bound surface species. *In-situ* FTIR can be used to measure the vibrational modes of surface atoms. This *in-situ* FTIR scans the infrared energy range during ALD cycles, which can identify the adsorption and desorption of surface molecules.

Once self-limiting growth has been established, there are other methods used to verify the quality of the film. Specifically, XPS is a surface characterization technique that measures the binding energy between atoms and allows users to analyze the chemical composition of the thin film and validate the purity of the ALD films[49,50]. A range of other techniques are used to further characterize ALD films.

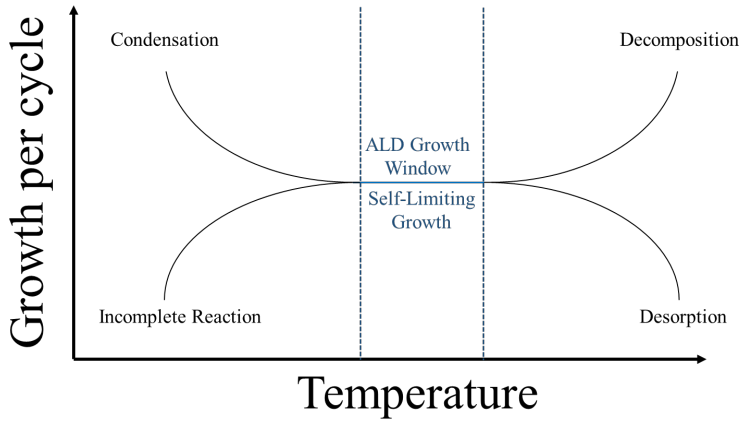

Figure 2.4. Schematic of the ALD growth window.

2.3.2 First-Principles Calculations

First-principles methods are effective for understanding the thermodynamics involved during ALD. Specifically, density functional theory (DFT) calculates the ground state of the system and can explain the unobservable phenomena at the atomic scale that cannot be studied *in-situ*. DFT studies of ALD consist of atomic orbital basis set and plane wave basis set calculations. Atomic orbital basis set calculations can only contain fewer than 100 atoms and are used to model reaction coordinates and calculate accurate transition states by using small portions of the surface with a single precursor[51-55]. Atomic orbital basis sets are ideal for calculating geometries and vibrational frequencies of known chemical precursors[56], as well as reactions that undergo a stable intermediate complex or hydrolysis[55,56]. These targeted calculations examine various bonding formations and can identify the exothermic or endothermic pathways during a reaction[51,54]. Atomic orbital basis set calculations have identified precursor candidates for selective ALD[53] while maintaining accurate reaction barriers that align with experiment[57].

Conversely, plane wave basis set calculations can contain up to 1000 atoms (1 cubic nanometer). Unlike atomic orbital basis set calculations, plane wave basis sets can improve accuracy by exploring many possibly reaction pathways. DFT has been extensively used to simulate the ALD growth of various thin films[58-75], including but not limited to Al_2O_3[58-60,63,64,68,69,71,76,77] (including ordered and disordered), HfO_2[66,70,71], Si-based[61,62,65], TiO_2[75], W[67] and MoS_2[72,73]. Periodic boundary condition is used in a variety of DFT calculations to understand ALD. Plane wave basis set studies have examined how surfaces can be passivated or fully saturated after exposure[76,77], as well as estimated charge transfer, which can quantify bond strength, and identify type of electronic interaction and how precursor bonding originates[78-81]. However, a majority of these DFT studies for ALD only focused on the thermodynamics of a single precursor on a surface and did not clearly address the nucleation and growth mechanisms of the thin films.

2.3.3 ALD of MoS_2

2D-MoS_2 has been grown via CVD, but the high operating temperatures[42-44] and lack of self-limiting growth[46,47] have prompted further investigations into alternative methods like ALD. Table 2.2 contains a collection of the known precursor chemistries and temperatures ranges used for ALD of bulk MoS_2.

Table 2.2 Sample of some of the up-to-date chemistries and temperatures used for ALD of MoS_2 (not including any post-treatment to achieve crystallinity). CO = carbonyl, Me = Methyl group, thd = 2,2,6,6-tetramethylheptane-3,5-dionato.

Mo-Source	S-Source	Temperature (°C)	Ref.
$MoCl_5$	H_2S	375-475	[82]
$MoCl_5$	H_2S	350-450	[83]
$MoCl_5$	H_2S	300	[84]
$MoCl_5$	H_2S	250-325	[85]
$Mo(CO)_6$	H_2S	170	[86]
$Mo(CO)_6$	$CH_3S_2CH_3$	100	[87]
$Mo(NMe_2)_4$	H_2S	60	[88]
$Mo(CO)_6$	H_2S	175-225	[89]
$MoCl_5$	H_2S	450	[90]
$Mo(thd)_3$	H_2S	300	[91]
$Mo(NMe_2)_4$	$CH_3S_2CH_3$	50	[92]
MoF_6	H_2S	150-250	[49,50]

These low deposition temperatures for MoS_2 have potential for industrial integration. However, post processing treatments, such as annealing, are required to achieve crystallinity[49,50,82,84,85,87,88,92]. Therefore, it is imperative to fundamentally understand the nucleation mechanisms for ALD of MoS_2. This dissertation focuses on the molybdenum hexafluoride (MoF_6) and hydrogen disulfide (H_2S) chemistry, which both are extremely volatile. MoF_6 has a high vapor pressure and a liquid phase at room temperature, allowing for a simpler delivery system into the chamber. Unlike other Mo

sources, MoF_6 does not grow films with C or Cl contamination, and strong Al-F bonds improve deposition. H_2S precursor is commonly used as a sulfur source.

However, knowledge gaps remain regarding the ALD process of MoS_2:

- Can the surface chemistry and morphology control nucleation and help develop free-standing MoS_2?
- How do the MoF_6 precursors interact with the surfaces? What types of reaction pathways can be expected?
- Do the bonds between the precursor and surface change with additional precursors? If so, how?
- How does S from H_2S deposit onto the film? What kinds of reaction pathways should be expected?

This dissertation aims to understand the nucleation mechanisms for ALD of MoS_2 to facilitate the growth of 2D-MoS_2. The primary focus is on the first half-cycle using MoF_6 as a precursor, and Chapter 6 investigates the second half-cycle using H_2S. The hypothesis of this research is that nucleation can be controlled by altering the surface chemistry and morphology of oxide substrates. Hydroxyl groups (OH) on the surface is a possible method to alter the surface chemistry, as discussed in detail below.

References

[1] Roger F Sebenik, A Richard Burkin, Robert R Dorfler, John M Laferty, Gerhard Leichtfried, Hartmut Meyer-Grünow, Philip CH Mitchell, Mark S Vukasovich, Douglas A Church, and Gary G Van Riper, Ullmann's Encyclopedia of Industrial Chemistry (2000).

[2] Katsuyoshi Kobayashi and Jun Yamauchi, Physical Review B **51** (23), 17085 (1995).

[3] Manish Chhowalla, Hyeon Suk Shin, Goki Eda, Lain-Jong Li, Kian Ping Loh, and Hua Zhang, Nature chemistry **5** (4), 263 (2013).

[4] Qing Hua Wang, Kourosh Kalantar-Zadeh, Andras Kis, Jonathan N Coleman, and Michael S Strano, Nature nanotechnology **7** (11), 699 (2012).

[5] Kin Fai Mak, Changgu Lee, James Hone, Jie Shan, and Tony F Heinz, Physical review letters **105** (13), 136805 (2010).

[6] Branimir Radisavljevic, Aleksandra Radenovic, Jacopo Brivio, i V. Giacometti, and A. Kis, Nature nanotechnology **6** (3), 147 (2011).

[7] Goki Eda, Hisato Yamaguchi, Damien Voiry, Takeshi Fujita, Mingwei Chen, and Manish Chhowalla, Nano letters **11** (12), 5111 (2011).

[8] Andrea Splendiani, Liang Sun, Yuanbo Zhang, Tianshu Li, Jonghwan Kim, Chi-Yung Chim, Giulia Galli, and Feng Wang, Nano letters **10** (4), 1271 (2010).

[9] Simone Bertolazzi, Jacopo Brivio, and Andras Kis, ACS nano **5** (12), 9703 (2011).

[10] Can Ataca, Hasan Sahin, and Salim Ciraci, The Journal of Physical Chemistry C **116** (16), 8983 (2012).

[11] Joy Heising and Mercouri G Kanatzidis, Journal of the American Chemical Society **121** (4), 638 (1999).

[12] Xiao Zhang, Zhuangchai Lai, Chaoliang Tan, and Hua Zhang, Angewandte Chemie International Edition **55** (31), 8816 (2016).

[13] Min-Rui Gao, Maria KY Chan, and Yugang Sun, Nature communications **6**, 7493 (2015).

[14] Jakob Kibsgaard, Zhebo Chen, Benjamin N Reinecke, and Thomas F Jaramillo, Nature materials **11** (11), 963 (2012).

[15] Junfeng Xie, Hao Zhang, Shuang Li, Ruoxing Wang, Xu Sun, Min Zhou, Jingfang Zhou, Xiong Wen Lou, and Yi Xie, Advanced materials **25** (40), 5807 (2013).

[16] Shengjie Xu, Dian Li, and Peiyi Wu, Advanced Functional Materials **25** (7), 1127 (2015).

[17] Junze Chen, Xue-Jun Wu, Lisha Yin, Bing Li, Xun Hong, Zhanxi Fan, Bo Chen, Can Xue, and Hua Zhang, Angewandte Chemie International Edition **54** (4), 1210 (2015).

[18] Yang Hou, Zhenhai Wen, Shumao Cui, Xiaoru Guo, and Junhong Chen, Advanced materials **25** (43), 6291 (2013).

[19] Anders B Laursen, Søren Kegnæs, Søren Dahl, and Ib Chorkendorff, Energy & Environmental Science **5** (2), 5577 (2012).

[20] Weijia Zhou, Zongyou Yin, Yaping Du, Xiao Huang, Zhiyuan Zeng, Zhanxi Fan, Hong Liu, Jiyang Wang, and Hua Zhang, small **9** (1), 140 (2013).

[21] Kun Chang and Weixiang Chen, ACS nano **5** (6), 4720 (2011).

[22] Shujiang Ding, Jun Song Chen, and Xiong Wen Lou, Chemistry–A European Journal **17** (47), 13142 (2011).

[23] Yun-Xiao Wang, Shu-Lei Chou, David Wexler, Hua-Kun Liu, and Shi-Xue Dou, Chemistry–A European Journal **20** (31), 9607 (2014).

[24] Fei Zhou, Sen Xin, Hai-Wei Liang, Lu-Ting Song, and Shu-Hong Yu, Angewandte Chemie International Edition **53** (43), 11552 (2014).

[25] Liang Cheng, Jingjing Liu, Xing Gu, Hua Gong, Xiaoze Shi, Teng Liu, Chao Wang, Xiaoyong Wang, Gang Liu, and Huaiyong Xing, Advanced materials **26** (12), 1886 (2014).

[26] Stanley S Chou, Bryan Kaehr, Jaemyung Kim, Brian M Foley, Mrinmoy De, Patrick E Hopkins, Jiaxing Huang, C Jeffrey Brinker, and Vinayak P Dravid, Angewandte Chemie International Edition **52** (15), 4160 (2013).

[27] Teng Liu, Chao Wang, Xing Gu, Hua Gong, Liang Cheng, Xiaoze Shi, Liangzhu Feng, Baoquan Sun, and Zhuang Liu, Advanced materials **26** (21), 3433 (2014).

[28] Wenyan Yin, Liang Yan, Jie Yu, Gan Tian, Liangjun Zhou, Xiaopeng Zheng, Xiao Zhang, Yuan Yong, Juan Li, and Zhanjun Gu, ACS nano **8** (7), 6922 (2014).

[29] Jong-Seon Kim, Hae-Wook Yoo, Hyung Ouk Choi, and Hee-Tae Jung, Nano letters **14** (10), 5941 (2014).

[30] F Keith Perkins, Adam L Friedman, Enrique Cobas, PM Campbell, GG Jernigan, and Berend T Jonker, Nano letters **13** (2), 668 (2013).

[31] Yang Tan, Ruiyun He, Chen Cheng, Dong Wang, Yanxue Chen, and Feng Chen, Scientific reports **4**, 7523 (2014).

[32] Zongyou Yin, Hai Li, Hong Li, Lin Jiang, Yumeng Shi, Yinghui Sun, Gang Lu, Qing Zhang, Xiaodong Chen, and Hua Zhang, ACS nano **6** (1), 74 (2011).

[33] Zhiyuan Zeng, Zongyou Yin, Xiao Huang, Hai Li, Qiyuan He, Gang Lu, Freddy Boey, and Hua Zhang, Angewandte Chemie International Edition **50** (47), 11093 (2011).

[34] Changfeng Zhu, Zhiyuan Zeng, Hai Li, Fan Li, Chunhai Fan, and Hua Zhang, Journal of the American Chemical Society **135** (16), 5998 (2013).

[35] Rudren Ganatra and Qing Zhang, ACS nano **8** (5), 4074 (2014).

[36] Xiao Huang, Zhiyuan Zeng, and Hua Zhang, Chemical Society Reviews **42** (5), 1934 (2013).

[37] Kangho Lee, Hye-Young Kim, Mustafa Lotya, Jonathan N Coleman, Gyu-Tae Kim, and Georg S Duesberg, Advanced materials **23** (36), 4178 (2011).

[38] Juqing Liu, Zhiyuan Zeng, Xiehong Cao, Gang Lu, Lian-Hui Wang, Qu-Li Fan, Wei Huang, and Hua Zhang, Small **8** (22), 3517 (2012).

[39] Min Yi and Zhigang Shen, Journal of Materials Chemistry A **3** (22), 11700 (2015).

[40] Jonathan N Coleman, Mustafa Lotya, Arlene O'Neill, Shane D Bergin, Paul J King, Umar Khan, Karen Young, Alexandre Gaucher, Sukanta De, and Ronan J Smith, Science **331** (6017), 568 (2011).

[41] Jong-Hee Park and TS Sudarshan, *Chemical vapor deposition*. (ASM international, 2001).

[42] Yi-Hsien Lee, Xin-Quan Zhang, Wenjing Zhang, Mu-Tung Chang, Cheng-Te Lin, Kai-Di Chang, Ya-Chu Yu, Jacob Tse-Wei Wang, Chia-Seng Chang, and Lain-Jong Li, Advanced materials **24** (17), 2320 (2012).

[43] Jianping Shi, Donglin Ma, Gao-Feng Han, Yu Zhang, Qingqing Ji, Teng Gao, Jingyu Sun, Xiuju Song, Cong Li, and Yanshuo Zhang, ACS nano **8** (10), 10196 (2014).

[44] Yongjie Zhan, Zheng Liu, Sina Najmaei, Pulickel M Ajayan, and Jun Lou, Small **8** (7), 966 (2012).

[45] Hyungjun Kim, Journal of Vacuum Science & Technology B: Microelectronics and Nanometer Structures Processing, Measurement, and Phenomena **21** (6), 2231 (2003).

[46] Yu-Chuan Lin, Wenjing Zhang, Jing-Kai Huang, Keng-Ku Liu, Yi-Hsien Lee, Chi-Te Liang, Chih-Wei Chu, and Lain-Jong Li, Nanoscale **4** (20), 6637 (2012).

[47] Xi Ling, Yi-Hsien Lee, Yuxuan Lin, Wenjing Fang, Lili Yu, Mildred S Dresselhaus, and Jing Kong, Nano letters **14** (2), 464 (2014).

[48] Steven M George, Chemical reviews **110** (1), 111 (2009).

[49] Steven Letourneau, Matthias J Young, Nicholas M Bedford, Yang Ren, Angel Yanguas-Gil, Anil U Mane, Jeffrey W Elam, and Elton Graugnard, ACS Applied Nano Materials **1** (8), 4028 (2018).

[50] Anil U Mane, Steven Letourneau, David J Mandia, Jian Liu, Joseph A Libera, Yu Lei, Qing Peng, Elton Graugnard, and Jeffrey W Elam, Journal of Vacuum Science & Technology A: Vacuum, Surfaces, and Films **36** (1), 01A125 (2018).

[51] Min Dai, Jinhee Kwon, Mathew D. Halls, Roy G. Gordon, and Yves J. Chabal, Langmuir **26** (6), 3911 (2010).

[52] Maxim Deminsky, Andrei Knizhnik, Ivan Belov, Stanislav Umanskii, Elena Rykova, Alexander Bagatur'yants, Boris Potapkin, Matthew Stoker, and Anatoli Korkin, Surface Science **549** (1), 67 (2004).

[53] Wonyoung Lee, Neil P. Dasgupta, Orlando Trejo, Jung-Rok Lee, Jaeeun Hwang, Takane Usui, and Fritz B. Prinz, Langmuir **26** (9), 6845 (2010).

[54] Kejing Li, Shenggang Li, Ning Li, David A. Dixon, and Tonya M. Klein, The Journal of Physical Chemistry C **114** (33), 14061 (2010).

[55] Yuniarto Widjaja and Charles B. Musgrave, Applied Physics Letters **80** (18), 3304 (2002).

[56] Magdalena Siodmiak, Gernot Frenking, and Anatoli Korkin, The Journal of Physical Chemistry A **104** (6), 1186 (2000).

[57] Kejing Li, Shenggang Li, Ning Li, Tonya M Klein, and David A Dixon, The Journal of Physical Chemistry C **115** (38), 18560 (2011).

[58] Simon D Elliott, Computational materials science **33** (1-3), 20 (2005).

[59] Simon D Elliott and Henry P Pinto, Journal of electroceramics **13** (1-3), 117 (2004).

[60] S. D. Elliott, G. Scarel, C. Wiemer, M. Fanciulli, and G. Pavia, Chemistry of Materials **18** (16), 3764 (2006).

[61] Liang Huang, Bo Han, Bing Han, Agnes Derecskei-Kovacs, Manchao Xiao, Xinjian Lei, Mark L O'Neill, Ronald M Pearlstein, Haripin Chandra, and Hansong Cheng, Physical Chemistry Chemical Physics **16** (34), 18501 (2014).

[62] Yong-Chan Jeong, Seung-Bin Baek, Dae-Hee Kim, Ji-Su Kim, and Yeong-Cheol Kim, Applied Surface Science **280**, 207 (2013).

[63] Dae-Hee Kim, Seung-Bin Baek, and Yeong-Cheol Kim, Applied Surface Science **258** (1), 225 (2011).

[64] Dae-Hee Kim, Seung-Bin Baek, Hwa-Il Seo, and Yeong-Cheol Kim, Applied Surface Science **257** (15), 6326 (2011).

[65] Kyungtae Lee, Woojin Lee, Hyo Sug Lee, Jaikwang Shin, Jieun Park, Seongsuk Lee, Samjong Choi, Sueryeon Kim, Jinseong Kim, and Youngseon Shim, Physical Chemistry Chemical Physics **18** (42), 29139 (2016).

[66] Atashi B. Mukhopadhyay, Javier Fdez Sanz, and Charles B. Musgrave, Chemistry of Materials **18** (15), 3397 (2006).

[67] Hwanyeol Park, Sungwoo Lee, Ho Jun Kim, Daekwang Woo, Jong Myeong Lee, Euijoon Yoon, and Gun-Do Lee, RSC Advances **8** (68), 39039 (2018).

[68] Aditya Shankar Sandupatla, Konstantinos Alexopoulos, Marie-Françoise Reyniers, and Guy B Marin, The Journal of Physical Chemistry C **119** (32), 18380 (2015).

[69] Aditya Shankar Sandupatla, Konstantinos Alexopoulos, Marie-Françoise Reyniers, and Guy B Marin, The Journal of Physical Chemistry C **119** (23), 13050 (2015).

[70] Mahdi Shirazi and Simon D Elliott, Chemistry of Materials **25** (6), 878 (2013).

[71] Mahdi Shirazi and Simon D Elliott, Nanoscale **7** (14), 6311 (2015).

[72] M Shirazi, WMM Kessels, and AA Bol, APL Materials **6** (11), 111107 (2018).

[73] M Shirazi, WMM Kessels, and AA Bol, Physical Chemistry Chemical Physics **20** (24), 16861 (2018).

[74] D. Elliott Simon, Semiconductor Science and Technology **27** (7), 074008 (2012).

[75] Aleksandra Zydor, Vadim G Kessler, and Simon D Elliott, Physical Chemistry Chemical Physics **14** (22), 7954 (2012).

[76] Jaesoo Ahn, Tyler Kent, Evgueni Chagarov, Kechao Tang, Andrew C Kummel, and Paul C McIntyre, Applied Physics Letters **103** (7), 071602 (2013).

[77] AJ Kerr, E Chagarov, S Gu, T Kaufman-Osborn, S Madisetti, J Wu, PM Asbeck, S Oktyabrsky, and AC Kummel, The Journal of chemical physics **141** (10), 104702 (2014).

[78] Cameron Bjelkevig, Zhou Mi, Jie Xiao, PA Dowben, Lu Wang, Wai-Ning Mei, and Jeffry A Kelber, Journal of Physics: Condensed Matter **22** (30), 302002 (2010).

[79] Lin Chen, Robert E Warburton, Kan-Sheng Chen, Joseph A Libera, Christopher Johnson, Zhenzhen Yang, Mark C Hersam, Jeffrey P Greeley, and Jeffrey W Elam, Chem **4** (10), 2418 (2018).

[80] Sylwia Klejna and Simon D Elliott, The Journal of Physical Chemistry C **116** (1), 643 (2012).

[81] Kevin Leung, Yue Qi, Kevin R Zavadil, Yoon Seok Jung, Anne C Dillon, Andrew S Cavanagh, Se-Hee Lee, and Steven M George, Journal of the American Chemical Society **133** (37), 14741 (2011).

[82] Arturo Valdivia, Douglas J Tweet, and John F Conley Jr, Journal of Vacuum Science & Technology A: Vacuum, Surfaces, and Films **34** (2), 021515 (2016).

[83] Robert Browning, Prasanna Padigi, Raj Solanki, Douglas J Tweet, Paul Schuele, and David Evans, Materials Research Express **2** (3), 035006 (2015).

[84] Lee Kheng Tan, Bo Liu, Jing Hua Teng, Shifeng Guo, Hong Yee Low, and Kian Ping Loh, Nanoscale **6** (18), 10584 (2014).

[85] Thi Anh Ho, Changdeuck Bae, Seonhee Lee, Myungjun Kim, Josep M Montero-Moreno, Jong Hyeok Park, and Hyunjung Shin, Chemistry of Materials **29** (17), 7604 (2017).

[86] Dip K Nandi, Uttam K Sen, Devika Choudhury, Sagar Mitra, and Shaibal K Sarkar, Electrochimica Acta **146**, 706 (2014).

[87] Zhenyu Jin, Seokhee Shin, Do Hyun Kwon, Seung-Joo Han, and Yo-Sep Min, Nanoscale **6** (23), 14453 (2014).

[88] Titel Jurca, Michael J Moody, Alex Henning, Jonathan D Emery, Binghao Wang, Jeffrey M Tan, Tracy L Lohr, Lincoln J Lauhon, and Tobin J Marks, Angewandte Chemie International Edition **56** (18), 4991 (2017).

[89] Yujin Jang, Seungmin Yeo, Hyungjun Kim, and Soo-Hyun Kim, Applied Surface Science **365**, 160 (2016).

[90] Lei Liu, Yazhou Huang, Jingjie Sha, and Yunfei Chen, Nanotechnology **28** (19), 195605 (2017).

[91] Miika Mattinen, Timo Hatanpää, Tiina Sarnet, Kenichiro Mizohata, Kristoffer Meinander, Peter J King, Leonid Khriachtchev, Jyrki Räisänen, Mikko Ritala, and Markku Leskelä, Advanced Materials Interfaces **4** (18), 1700123 (2017).

92 Stéphane Cadot, Olivier Renault, Mathieu Frégnaux, Denis Rouchon, Emmanuel Nolot, Kai Szeto, Chloé Thieuleux, Laurent Veyre, Hanako Okuno, and François Martin, Nanoscale **9** (2), 538 (2017).

CHAPTER THREE: FIRST-PRINCIPLES SOLID STATE THERMODYNAMICS USING DENSITY FUNCTIONAL THEORY

3.1 Overview of DFT

First-principles solid state thermodynamic computations is based in quantum mechanics using Schrödinger's wave function (ψ) to calculate the total energy, *E*, of the system:

$$\hat{H}\boldsymbol{\psi}(\boldsymbol{r_i}, \boldsymbol{r_I}, \boldsymbol{t}) = \boldsymbol{E}\boldsymbol{\psi}(\boldsymbol{r_i}, \boldsymbol{r_I}, \boldsymbol{t}) \quad (1)$$

Where $\hat{H}$ is the Hamiltonian operator, ψ is the wavefunction, r_i and r_I are the coordinates of the electron and nucleus, respectively, and t is time. In a many body system, the number of electron-electron and electron-ion interactions begins to increase exponentially. As the number of electrons in a system become insurmountable several approximations must be applied to make the calculations feasible. Firstly, gravity and relativity should be neglected for electrons because their masses are negligible, and they move much slower than the speed of light. Secondly, first-principles studies restrict the system to only its ground state and therefore solving the time-independent Schrödinger equation:

$$\hat{H}\boldsymbol{\psi}(\boldsymbol{r_i}, \boldsymbol{r_l}) = \boldsymbol{E}\boldsymbol{\psi}(\boldsymbol{r_i}, \boldsymbol{r_l}) \quad (2)$$

The next step is to decouple the dynamics between the nucleus of the atom and the electrons surrounding it which is known as the Born-Oppenheimer approximation.

The Born-Oppenheimer approximation stems from the idea that the nucleus of the atom is so much larger than electrons that any movement of the nucleus does not affect the electrons' relative positions. The wavefunction then becomes a function of electron coordinates, and allows us to further simplify equation (2) into the time-independent wave equation:

$$\hat{\mathrm{H}}(\boldsymbol{r})\boldsymbol{\psi}(\boldsymbol{r}) = \boldsymbol{E}\boldsymbol{\psi}(\boldsymbol{r}) \tag{3}$$

Where $\hat{\mathrm{H}}(r)$ is the Hamiltonian operator, $\psi(r)$ is the wave function, E is the total energy of the system, and r is now the electron coordinate[1].

3.2 Density Functional Theory

Density functional theory (DFT) simplifies many of the mathematical challenges associated with calculating the quantum effects in a many body system. In the n-electron system, the calculation is dictated by the number of electrons, and thereby can drastically increase the computational demand. In order to understand the DFT, framework the Hamiltonian Operator needs to be defined.

3.2.1 The Hamiltonian Operator

The Hamiltonian Operator ($\hat{\mathrm{H}}$) incorporates all the energy terms used in first-principles calculations and is as follows:

$$\hat{\mathrm{H}} = \boldsymbol{E_{kin}} + \boldsymbol{E_{ext}} + \boldsymbol{E_H} + \boldsymbol{E_{xc}} \tag{4}$$

The first term E_{kin} considers the kinetic energy of the electrons in the system:

$$\boldsymbol{E_{kin}} = -\frac{\hbar^2}{2\boldsymbol{m}}\sum_{\boldsymbol{i}}^{\boldsymbol{n}}\boldsymbol{\nabla^2} = \frac{\mathbf{1}}{\mathbf{2}}\sum_{\boldsymbol{i}}^{\boldsymbol{n}}\boldsymbol{\nabla^2} \tag{5}$$

Later sections will address how Equation 5 simplifies from an all *n*-electron system into a non-interaction *n*-electron system. The second term in the Hamiltonian is the potential energies E_{ext} arising from the Coulombic interactions between the nucleus and electrons ($U_{electron-nucleus}$), and the interactions between the electrons themselves $U_{electron-electron}$. Thus, E_{ext} can be expressed as:

$$\boldsymbol{E_{ext} = U_{electron-nucleus} + U_{electron-electron}}$$

The next task is to break down E_{ext} into its two separate portions. First, the $U_{electron-nucleus}$ is broken down as the sum of all nucleus-electrons interactions within the system where *N* and *n* represent the number of nuclei and electrons, respectively, and Z_l is the charge on the nuclei:

$$\boldsymbol{U_{electron-nucleus} = -\sum_{l}^{N}\sum_{i}^{n}\frac{Z_l}{|r_{li}|}}$$

The interactions between the electrons themselves ($U_{electron-electron}$) can be written as:

$$\boldsymbol{U_{electron-electron} = \frac{1}{2}\sum_{i\neq j}^{n}\frac{1}{|r_{li}|}}$$

The combination of $U_{electron-nucleus}$ and $U_{electron-electron}$ gives E_{ext}:

$$\boldsymbol{E_{ext}} = -\sum_{\boldsymbol{l}}^{\boldsymbol{N}}\sum_{\boldsymbol{i}}^{\boldsymbol{n}}\frac{\mathbf{Z}_{\boldsymbol{l}}}{|\boldsymbol{r_{li}}|} + \frac{\mathbf{1}}{\mathbf{2}}\sum_{\boldsymbol{i}\neq\boldsymbol{j}}^{\boldsymbol{n}}\frac{\mathbf{1}}{|\boldsymbol{r_{li}}|} \quad (6)$$

The third term in the Hamiltonian is the Hartree energy (E_H). E_H improves the accuracy of the Hamiltonian energy term because it helps describe how electrons interact with one another. The Hartee-Fock (HF) model takes a simplified approach where election interactions are not considered individually but as an average density with respect to position. The resulting E_H is defined in Equation 7:

$$\boldsymbol{E_{ext}} = \frac{\mathbf{1}}{\mathbf{2}}\int\int\frac{\boldsymbol{\rho(r)\rho(r')}}{\boldsymbol{|r-r'|}}\boldsymbol{drdr'} \quad (7)$$

The final term in the Hamiltonian is the exchange correlation energy (E_{xc}). E_{xc} takes into account the differences in energy between interacting electrons with the same and different spins and plays an important role in the accuracy of the calculation. It can be modeled by the local density approximation (LDA) or general gradient approximation (GGA). LDA provides an intuitive solution for describing the electron density of a system[2]. In a real system there are large variations in the electron density. To counteract these variations LDA treats the electron density as a homogenous gas system. It partitions localized areas of similar charge densities into a homogenous gas where the electron density is fixed in that localized area. This results in sections of the electron density being constant in terms of energy and allows for an accurate and fast energy calculation. Due to the nature of treating the electron density as a homogenous gas, materials that are not homogenous in charge density will suffer in accuracy. Therefore, the LDA functional should be used when examining systems containing only one atom type. When dealing

with complex materials systems containing dramatically varying charge densities, GGA is the improved exchange correlation function. Although GGA uses the same framework from LDA to describe the electron density, there is one critical difference. GGA implements an additional factor to correct the difference in electron densities[3]. Equations 8 and 9 represent LDA and GGA, respectively. The important "S" factor included in GGA.

$$\boldsymbol{E_{xc}^{LDA}} = \int \boldsymbol{\rho(r)\,\epsilon_{xc}\,[\rho(r)]dr} \tag{8}$$

$$\boldsymbol{E_{xc}^{GGA}} = \int \boldsymbol{\rho(r)\,\epsilon_{xc}\,[\rho(r)]F(s)dr} \tag{9}$$

where

$$\boldsymbol{s = C\,\frac{|\nabla\rho(r)|}{\rho^{4/3}(r)}}$$

Figure 3.1 is a schematic representation of how LDA and GGA consider the charge density of a solid material. If we are partitioning the charge density into homogenous electron gases with LDA we describe the charge density using the orange partitions. There is no change in charge density relative to the location of the wavefunction. GGA changes the charge density with respect to position of the wavefunction as seen in green. The $F(s)$ factor in Equation 9 accounts for changes in the charge density and leads to more accurate models. GGA is therefore a superior method to estimate the exchange correlation energy and was used for all DFT calculations presented in this dissertation[1].

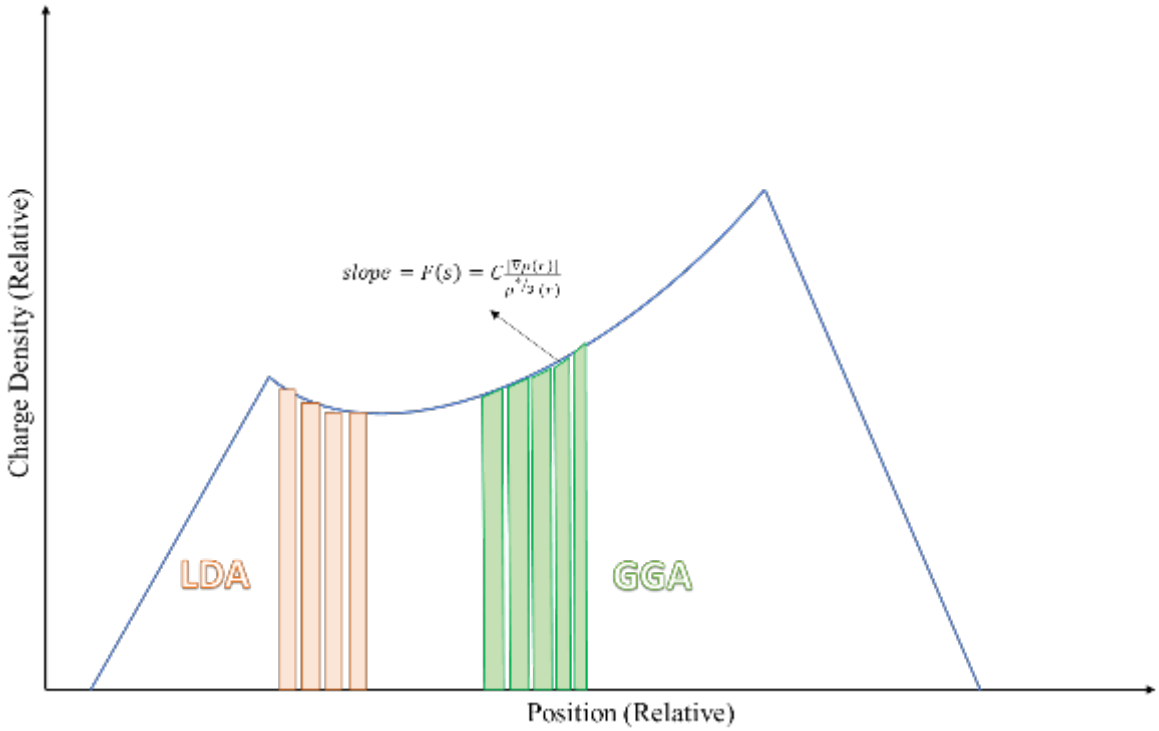

Figure 3.1. The schematic differences between calculating E_{xc} using the LDA and GGA functionals.

3.2.2 Implementing and Solving the Kohn-Sham Approach

The Kohn-Sham approach allows for an intuitive method that solves the *n*-electron problem and calculates the energy of the system. Unlike the first-principles approach, the Kohn-Sham equation uses the electron density $\rho(r)$ of the system which has several advantages. First and foremost, the Kohn-Sham approach disregards the *n*-electron interacting system for a one-electron non-interacting system. This results in a reformulation of the energy equations that leverages the $\rho(r)$ of individual electrons and therefore reduces the computational complexity. The Kohn-Sham approach can be seen in Equation 10 for the Kohn-Sham orbital (ϕ_i) and the density for an N-particle system:

$$\boldsymbol{\rho(r) = \sum_{i}^{N} |\, \phi_i(r)|^2} \qquad (10)$$

This equation becomes the basis for how Kohn-Sham orbitals form the charge density used in DFT calculations in this dissertation. With the Kohn-Sham approach the energy of the system can be calculated using the iterative self-consistency loop, as seen in Figure 3.2. This self-consistency loop implements an iterative diagonalization of the Kohn-Sham Hamiltonian matrix that works as follows:

1. Start with an initial (or trial) $\rho(r)$ by superimposing that initial $\rho(r)$ on each atom
2. Solve the Kohn-Sham equations to find a new $\rho(r)$
3. Compare the new $\rho(r)$ with the initial $\rho(r)$ against a predetermined convergence criteria
4. If $\rho(r)$ doesn't meet criteria solve the Kohn-Sham equations until criteria is met
5. Once $\rho(r)$ meets convergence criteria calculate atomic forces and update ion positions to predetermined atomic forces criteria
6. Repeat steps 2-5 until the ground state of the material is calculated then obtain materials properties

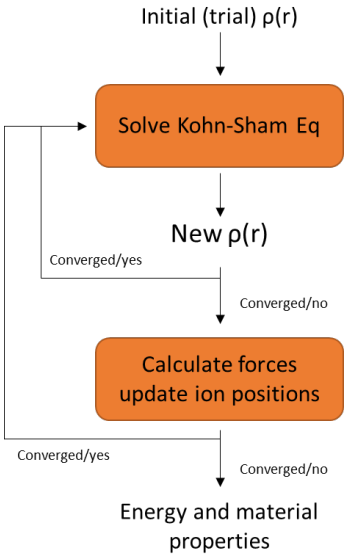

Figure 3.2. Iterative self-consistent loop used in density functional theory.

3.2.3 Simplifying Equations for Solids and Surfaces

When using DFT to calculate properties of solids and surfaces the Kohn-Sham equations can be overwhelmed by the sheer number of electrons in a system. In an effort to counteract the computational strain of millions upon millions of electrons, clever assumptions and approximations are made for DFT method. The first adaptation is the pseudopotential approach, as seen in Figure 3.3, separating electrons into two categories: electrons that participate in bonding or other chemical functions, and electrons close to nuclei that are rather inert. The pseudopotential approach works by "freezing" the core electrons and not including them in the DFT calculations. This results in only the outer valence electrons being used in the DFT calculations, which dramatically reduces the computational time while maintaining accuracy. When one considers all the electrons in the system (ψ_{AE}), there are significant fluctuations in the wavefunction close to the nucleus. These fluctuations are extremely difficult to compute and make it nearly impossible to reach the ground state due to the electron potential (U_{AE}). In order to alleviate these issues, the pseudopotential approach smooths the wavefunction close to

the nucleus (ψ_{PP}) and simulates a fictitious potential energy (U_{PP}) that substantially reduces the computational effort.

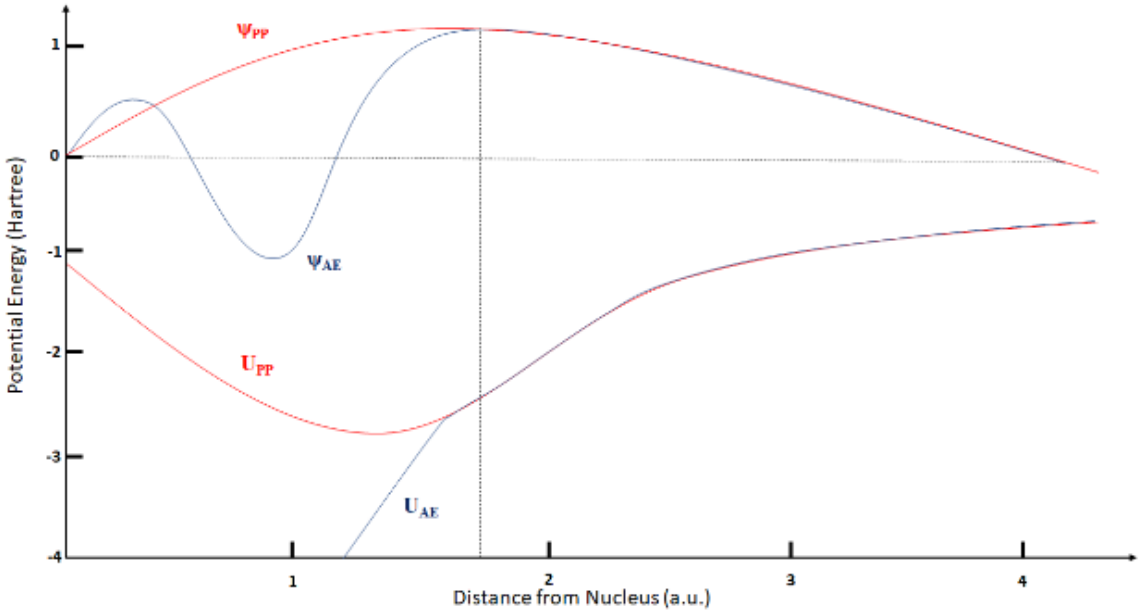

Figure 3.3. The pseudopotential approach is illustrated with the red lines. Fictitious wavefunctions and potential energies are incorporated when close to the nucleus to facilitate the calculations.

This dissertation uses a linear combination of plane wave expansion known as projected-augmented wave (PAW) potentials[4]. The PAW potentials function under the premises that wavefunctions are mapped from the core of the atom outwards in a radial fashion. The total number of wavefunctions used in the calculation is set by the cutoff energy (E_{cutoff}), where wavefunctions with energies larger than the E_{cutoff} are not incorporated. This results in wavefunctions of the valence electrons being consider in the DFT calculations. The second adaptation applied to the DFT method is periodic boundary condition (PBC), which can reduce the size of the cell considered in the DFT calculations by simulating a small atomic-scale portion of a material and extrapolating those results to the properties bulk of the material. This is also accomplished by implementing the Bloch

theorem, which allows one to treat real systems in terms of wave vector (k) and reciprocal-space (G).

3.3 DFT Methods Implemented in this Dissertation

Several DFT methods were implemented in this project to understand ALD of MoS_2, as shown in Figure 3.4. Surfaces were created with varying surface chemistries. Partial charge density and local density of states calculations were then applied to the surface. Partial charge density shows where electrons localize while local density of states identifies electronic states available for bonding. Next, precursors were introduced above the surface. Bond strengths were quantified between the surface and the precursor using the Bader charge analysis. The types of chemical bonding were determined by calculating the local density of states. Combining these different DFT methods with experimental measurements could reveal a possible nucleation mechanism for ALD of MoS_2. More details on each DFT method are discussed below.

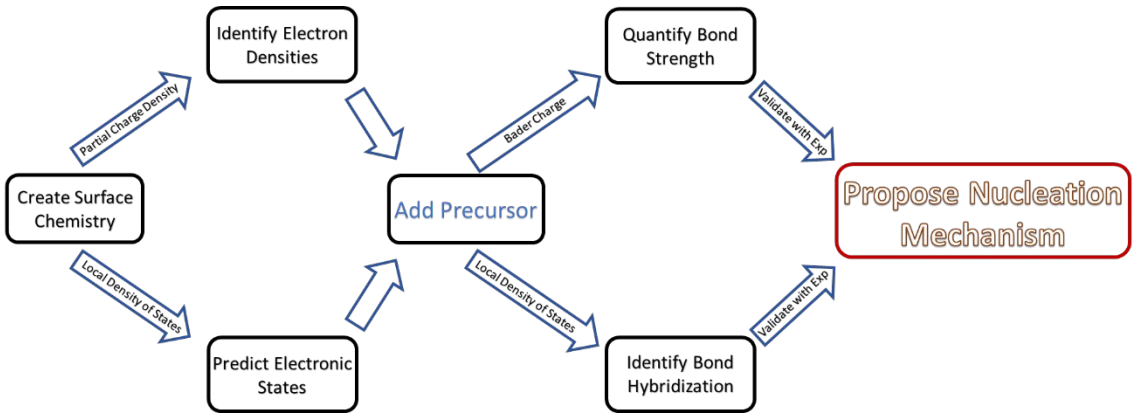

Figure 3.4. Workflow of the DFT calculations used to understand the nucleation mechanism for ALD of MoS_2.

3.3.1. Density of States

Density of States (DoS) can be used to determine if chemical bonds form between a gas phase precursor and solid surface during ALD. There are two possible types of

interactions: van der Waals and chemical. Van der Waals bonding is a purely physical type of bonding where electrons are not shared between the gas phase molecule and the surface. Typically, these bonds are weak, and can easily be broken mechanically or chemically. Van der Waals bonding is derived from instantaneous dipole moments and is characterized by short-range attractive forces. For these reasons, van der Waals bonding is catastrophic for ALD of thin films because the deposited films are not self-limiting. Conversely, chemical bonding requires the sharing or exchanging of electrons between the gas phase precursor and surface. Chemical bonds are far stronger than the van der Waals counterpart, and can occur as ionic or covalent bonds. As discussed earlier, ALD exploits a self-limiting form of chemical bonding, resulting in film composition and thickness control. Therefore, it is imperative to understand when chemical bonding occurs, how the chemical bonding functions, and which atoms between the precursor and substrate bond together. Calculating the DoS can reveal those features.

The DoS is a probability density function used in solid state physics. It quantifies the number of available states per unit volume at a given energy level. The DoS can be calculated using Equation 11:

$$\boldsymbol{D(E) = N(E)/V} \tag{11}$$

Where $N(E)$ and V represent the number of states in a system of volume V. Calculating the DoS of a solid material can give important information on its electronic properties. Specifically, the DoS can identify whether a material is insulating, semiconducting, or conducting. DoS has been widely used to study ALD. It determines when a surface has been fully saturated with precursors[5] or if surfaces can be passivated

by surface termination[6]. This dissertation aims to understand at what energies electrons from the precursor can bond to the substrate, suggesting what surface chemistries can promote deposition. Figure 3.5 is the calculated DoS for alumina surface without and with hydroxyl groups respectively. A single MoF_6 precursor is bonded to each surface. By partitioning electronic contributions created by the surface (red) and precursor (blue) it is possible to interpret the differences bonding behavior. Without hydroxyl groups there is little overlap between the surface and precursor electronic states which indicates van der Waals forces. The hydroxylated alumina DoS contains mid gap states populated by the surface and precursor, suggesting the formation of chemical bonds and therefore successful deposition using MoF_6.

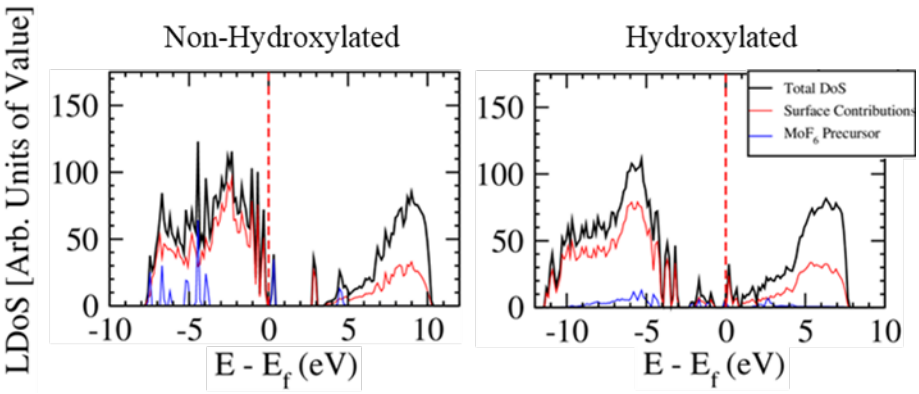

Figure 3.5. Calculated DoS for non-hydroxylated and hydroxylated Al_2O_3 surfaces with a single MoF_6 precursor above each.

3.3.2. Partial Charge Densities

Partial charge densities can help interpret the DoS results discussed above. Previous works have used partial charge densities to understand specific occupied states[7] or map where these occupied states are localized in the atomic structures of interest[8]. According to the analysis of DOS, the energy range considered for the partial charge densities should include the electronic interactions between the precursor and the

substrate. Figure 3.6 provides a cross section for the calculated partial charge densities for a non-hydroxylated and hydroxylated Al_2O_3 surface. We found an increase in electron density at the Al_2O_3 surfaces with the presence of hydroxyls. This indicates that hydroxyl groups could improve deposition, when compared to a non-hydroxylated surface.

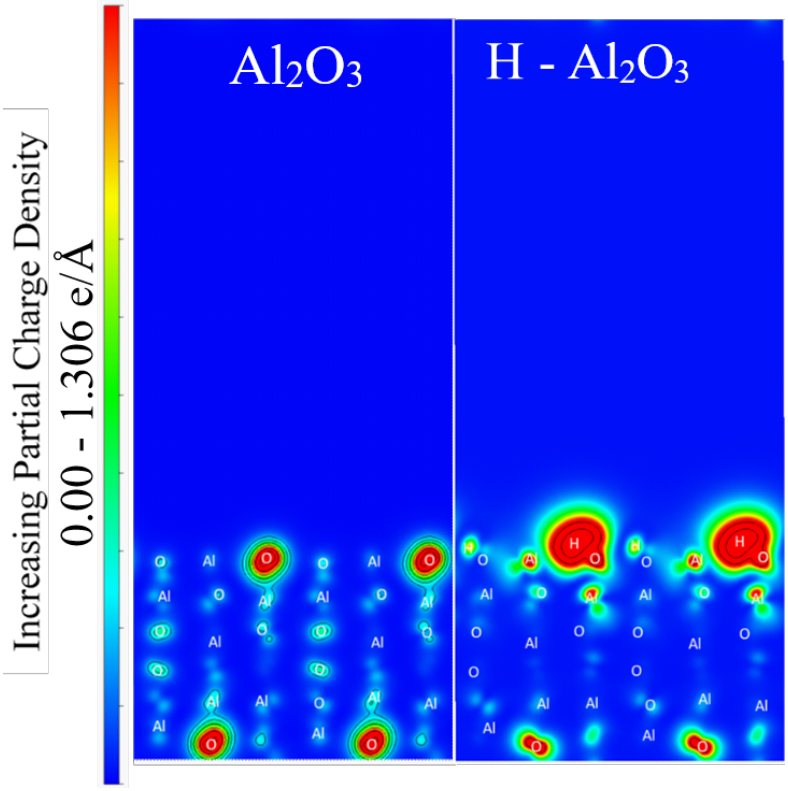

Figure 3.6. Calculated partial charge densities for non-hydroxylated and hydroxylated Al_2O_3.

3.3.3. Bader Charge Analysis

Bader charge analysis is commonly used to understand charge transfer in a system[9]. It takes an intuitive approach to partition atoms in a system in order to capture the specific charge on individual atoms, particularly useful when attempting to understand charge transfer between an adsorbate and a surface[10-13]. For example, Table 3.1 compares the Bader charge analysis for three substrates (Al_2O_3, HfO_2, and MgO) with and without hydroxyl groups in order to quantify the strength of MoF_6 precursor

adsorption. The metal Mo atom on the MoF_6 precursor has a more positive Bader charge above the hydroxylated surface when compared to the non-hydroxylated counterpart. The change in Bader charge indicated that the Mo atom has a stronger bond to hydroxylated surface.

Table 3.1 Calculated Bader charge analysis for non-hydroxylated and hydroxylated Al_2O_3, HfO_2, and MgO with a single MoF_6 molecule.

	Al_2O_3			HfO_2			MgO		
	Non-hydroxylated	Hydroxylated		Non-hydroxylated	Hydroxylated		Non-hydroxylated	Hydroxylated	
Atomic Species	**Bader Charge**		***Δ Bader***	**Bader Charge**		***Δ Bader***	**Bader Charge**		***Δ Bader***
Mo	-2.75	-1.53	*1.22*	-2.46	-1.94	*0.51*	-2.44	-2.09	*0.35*
F	0.45	0.70	*0.25*	0.47	0.63	*0.16*	0.44	0.62	*0.18*
F	0.45	0.92	*0.46*	0.42	0.62	*0.20*	0.44	0.62	*0.18*
F	0.46	0.86	*0.40*	0.50	0.70	*0.19*	0.58	0.79	*0.21*
F	0.46	0.85	*0.39*	0.57	0.69	*0.12*	0.53	0.81	*0.28*
F	0.47	0.85	*0.39*	0.47	0.70	*0.23*	0.53	0.79	*0.26*
F	0.45	0.71	*0.25*	0.49	0.72	*0.24*	0.44	0.61	*0.17*
Total F	2.75	4.88	*2.13*	2.93	4.07	*1.14*	2.95	4.24	*1.29*

3.3.4. Charge Density Difference

Charge density difference examines the electron densities only participating in adsorption, calculated using Equation 12:

$$\boldsymbol{\rho_{diff} = \rho_{total\ system} - \rho_{surface} - \rho_{adsorbate}} \quad (12)$$

where $\rho_{total\ system}$, $\rho_{surface}$, and $\rho_{adsorbate}$ represent the charge densities of the total system, surface, and adsorbate, respectively. Charge density difference can be projected onto the atomistic models, visualizing chemical bonding. Isosurfaces indicates a gain or loss of electrons. For example, Figure 3.7 demonstrates the charge density difference for an MoF_6 precursor above hydroxylated Al_2O_3 surfaces where blue and yellow isosurfaces indicate a gain and loss of electrons, respectively. Above the

hydroxylated surface more chemical bonds form between the precursor and the surface, indicating successful ALD deposition.

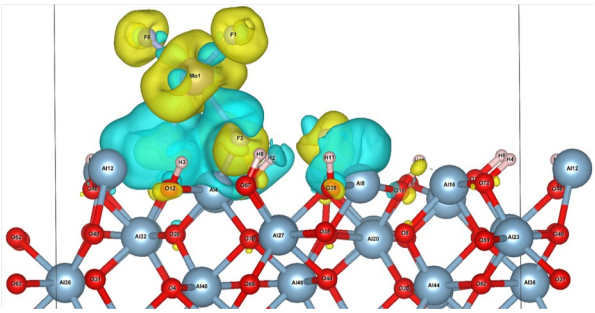

Figure 3.7. Calculated charge density difference for an MoF_6 precursor above a hydroxylated Al_2O_3 surface. Blue and yellow isosurfaces indicate a gain and loss of electrons, respectively.

References

1 June Gunn Lee, Computational materials science: an introduction. (CRC press, 2016).

2 Walter Kohn and Lu Jeu Sham, Physical review **140** (4A), A1133 (1965).

3 John P Perdew, Kieron Burke, and Matthias Ernzerhof, Physical review letters **77** (18), 3865 (1996).

4 G Kresse, Phys. Rev. B **54**, 11 (1996).

5 Jaesoo Ahn, Tyler Kent, Evgueni Chagarov, Kechao Tang, Andrew C Kummel, and Paul C McIntyre, Applied Physics Letters **103** (7), 071602 (2013).

6 AJ Kerr, E Chagarov, S Gu, T Kaufman-Osborn, S Madisetti, J Wu, PM Asbeck, S Oktyabrsky, and AC Kummel, The Journal of chemical physics **141** (10), 104702 (2014).

7 Ç Kaderoğlu, Z Ayduğan, B Alkan, and MEHMET Cakmak, The European Physical Journal B **76** (3), 359 (2010).

8 Yuanda Liu, Yongqing Cai, Gang Zhang, Yong-Wei Zhang, and Kah-Wee Ang, Advanced Functional Materials **27** (7), 1604638 (2017).

[9] W Tang, E Sanville, and G Henkelman, Journal of Physics: Condensed Matter **21** (8), 084204 (2009).

[10] Cameron Bjelkevig, Zhou Mi, Jie Xiao, PA Dowben, Lu Wang, Wai-Ning Mei, and Jeffry A Kelber, Journal of Physics: Condensed Matter **22** (30), 302002 (2010).

[11] Lin Chen, Robert E Warburton, Kan-Sheng Chen, Joseph A Libera, Christopher Johnson, Zhenzhen Yang, Mark C Hersam, Jeffrey P Greeley, and Jeffrey W Elam, Chem **4** (10), 2418 (2018).

[12] Sylwia Klejna and Simon D Elliott, The Journal of Physical Chemistry C **116** (1), 643 (2012).

[13] Kevin Leung, Yue Qi, Kevin R Zavadil, Yoon Seok Jung, Anne C Dillon, Andrew S Cavanagh, Se-Hee Lee, and Steven M George, Journal of the American Chemical Society **133** (37), 14741 (2011).

CHAPTER FOUR: FIRST-PRINCIPLES ANALYSIS OF STRUCTURAL STABILITY, ELECTRONIC AND PHONON TRANSPORT PROPERTIES OF LATERAL MOS_2-WX_2 HETEROSTRCUTURES

This chapter is published by Elsevier in *Computational Condensed Matter* and should be referenced appropriately.

Reference:

M. Lawson, I. Williamson, Z. Y. Ong, and L. Li, "First-principles analysis of structural stability, electronic and phonon transport properties of lateral MoS_2-WX_2 heterostructures", *Computational Condensed Matter.* **19**, e00389 (2019).

Reproduced from *Computational Condense Matter*, **19** e00389 (2019), with the permission of Elsevier

First-principles analysis of structural stability, electronic and phonon transport properties of lateral MoS_2-WX_2 heterostructures

Matthew Lawson[a]

Izaak Williamson[a]

Zhun-Yong Ong[b]

Lan Li[a, c]

Published in:

Computational Condensed Matter

June 2019

[a]*Micron School of Materials Science and Engineering,*

Boise State University, Boise, ID 83706, USA

[b]*Institute of High Performance Computing,*

*A*STAR, Singapore 138632, Singapore*

[c]*Center for Advanced Energy Studies,*

Idaho Falls, ID 83401, USA

Abstract

We performed first-principles-based methods to study the structural stability, electronic and phonon transport properties of lateral transition metal dichalcogenides. Specifically, we focused on the interface at the MoS_2-WX_2 heterostructures, where X= S or Se. The structures underwent pseudo uniaxial strain testing for compression and tension from 0 – 10% at 2% intervals. The electronic and phonon densities of states were calculated at each interval in comparison with the unstrained structure. Computational results provide insight into the effect of uniaxial strain on structure, electronic and phonon transport processes, causing a crucial impact of use of the materials in electronic devices. In addition, combining the calculated force constants with the atomistic Green's function method reveals interfacial thermal transport at the heterostructure and its underlying phonon mechanisms.

4.1 Introduction

Transition metal dichalcogenides (TMDs) have rapidly emerged in the electronic industry due to novel physical properties. Their composition is commonly written as MX_2 (M = transition metal, X = chalcogen), and they can exist as bulk, bilayer, and monolayer structures. In a monolayer sheet, two chalcogens sandwich each transition metal atom, and the in-plane covalent bonds supply stability while the weak out-of-plane van der Waals bonding allows individual sheets to be self-standing[1,2]. Unlike graphene, many two-dimensional (2D) TMDs possess band gaps with high electron mobilities suitable for use in semiconducting devices[1,3,4] . As the dimensionality decreases, e.g. from bulk MoS_2 to monolayer MoS_2, its electronic band gap shifts from an indirect 1.2 eV[5] to a direct 1.8 eV[1,6]. This finding has been observed in experiments[2,7,8] and density functional theory

(DFT) calculations[9-11]. Needless to say, MoS_2 is not the only TMD with an increased band gap as a monolayer structure[3].

Although single-layer TMDs have been extensively studied, TMD heterostructures have been much less explored in spite of their potential for tunable properties through combining various materials with different band gaps, electron mobilities, and work functions. Heterostructures can be either lateral or vertical. Lateral heterostructures are comprised of two different in-plane MX_2 monolayers to form a lateral configuration while vertical heterostructures stack two MX_2 monolayers in a vertical configuration. Unlike the weak van der Waal forces that hold vertical heterostructures together, lateral heterostructures have strong in-plane covalent bonds along their boundaries that exert significant effects on the transport properties of the heterostructure at the interface. Two common lateral heterostructures are MoS_2-WS_2 and MoS_2-WSe_2, which can be grown through chemical vapor deposition[12] (CVD), in which heteroepitaxy techniques facilitate the growth mechanics[13]. resulting in high-quality heterostructures with limited defects at the interface[14,15]. The MoS_2-WS_2 lateral heterostructure forms a straight interface that runs down the zig-zag direction[13]. Although the individual MoS_2 and WS_2 TMDs are n-type semiconductors[16], their lateral heterostructure is proven to act as an intrinsic p–n junction where WS_2 serves as the p-side while MoS_2 serves as the n-side[13,17] and electron-hole recombination can occur[13]. Like MoS_2-WS_2, the MoS_2-WSe_2 interface, which has a lattice mismatch of 5 percent, is also an ideal p – n junction as its I/V curve demonstrates good rectification character with a threshold voltage of about 0.9 V (forward biased)[18].

Given the increasing importance of TMD-based field effect transistors (FETs) that utilize the band-to-band tunneling effect[19], the ability to control interfacial properties, which include structure, electronic and phonon transport at the interface, can be highly advantageous for optimizing their device performance. To tune and control the band gap in TMDs, structural modification techniques like doping and alloying have been utilized [20] and may be analogously employed for heterostructures. The calculated formation energies of monolayer MoS_2-WS_2 indicate a stable structure[21], while the composition of the heterostructure has been shown to play a role in the band gap energy[22]. DFT calculations have identified a type-II band alignment for both MoS_2-WS_2 and MoS_2-WSe_2[22,23] which further suggests their potential for optoelectronics applications. Recent studies of the strain effects have also revealed how the band gap and band edges change under compression and tension. First-principles calculations of monolayer MoS_2 demonstrate a shift from a direct to indirect band gap at 0.3% tension and 1.3% compression[24]. Similar studies have also found that when MoS_2 undergoes 1.9% compression, the band gap increases by 0.13 eV. Tension uniformly decreases the band gap until the band gap vanishes at 9.8% tension and the structure becomes metallic. These findings imply that the electrical properties of the MoS_2-WS_2 lateral heterostructure are also sensitive to strain. The transition from type-II to type-I band alignment when a 8 percent tensile strain is applied to the WS_2-side of the MoS_2-WS_2 interface has been predicted using first-principles modeling[25]. In addition, first-principles calculations have also been used to investigate the power conversion efficiency of MoS_2-WS_2 lateral heterostructures, and demonstrate a 35% increase at 4% uniaxial strain[26].

Due to the significant effects of interface and uniaxial strain on the TMD heterostructure performance, this paper firstly presents our studies of the electronic and interfacial phonon transport properties of MX_2-MX_2 lateral heterostructures and how those properties can be manipulated through uniaxial strain. It then provides detailed insight into how the interface of the MX_2-MX_2 heterostructure plays a key role in the phonon scattering mechanisms that dictates thermal boundary conductance and transport processes.

4.2 Methods

Density functional theory (DFT)-based calculations were used to accurately model the ground state of the system. The Vienna Ab initio Simulation Package (VASP)[27] and Perdew-Burke-Ernzerhof (PBE)[28] pseudopotentials were implemented with the generalized gradient approximation (GGA) exchange correlation functions. A cut-off energy of 400 eV was chosen for the plane waves. The initial screening involved 88 heterojunctions and was used to identify viable lateral heterostructures. The structures were relaxed until the residual forces were reduced to 0.01 eV/Å while an energy convergence of $1x10^{-7}$ was achieved. The on-site Coulombic potentials were accounted for each transition metal. A Γ-centered 1x9x1 k-point mesh was selected, because both MX_2 leads were zig-zag terminated, and this was shown to lead to an accurate analysis at the band edges[29]. The long-range effect was also considered with lattice convergence test. In order to simulate a monolayer, 20 Å of vacuum was included in the unit cell to avoid interlayer interaction. Figure 4.1 shows an atomic structure of lateral MX_2-MX_2 heterostructure where the periodicity is applied parallel to the interface in the *b* direction.

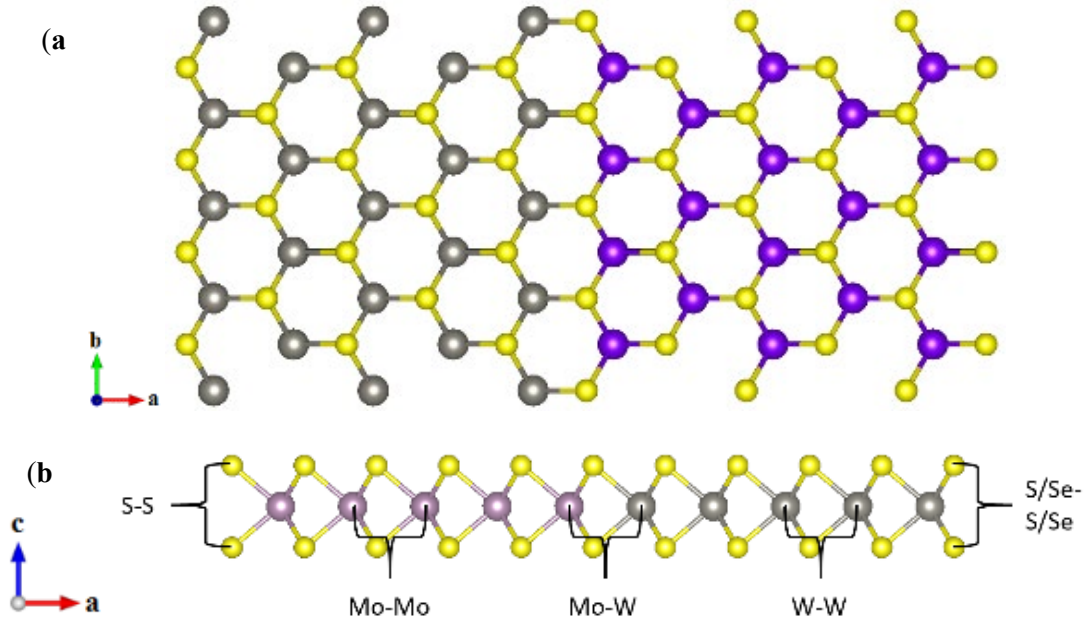

Figure 4.1. Atomic structure for lateral MX_2-M'X"$_2$ down the c axis (a) and b axis (b). Figure (b) also depicts how the distances are measured later in the manuscript. The grey and purple atoms correspond to transition metals while yellow atoms are chalcogenide. (Color online)

Our previous studies examined 18 combinations of MX_2 structures evaluated using a previously developed "criticality score"[30,31]. This "criticality score" was developed to gauge which transition metals could be used in mass production by comparing their supply risk, vulnerability to supply restriction, and environmental implications[31]. The lattice constants were determined for the 18 monolayer MX_2 structures. Given that a large difference between the lattice constants of the two MX_2 constituents in a lateral heterostructure would induce defects and strain at the interface, resulting in structural instability, it was determined that a lateral heterostructure with a difference in individual lattice constants greater than 7% was unsuitable for use in a FET.

The formation energy of each heterostructure was calculated with the following equation:

$$E_f = E_{total-hetero} - n\left(E_{total-left}\right) + m(E_{total-right}) \quad (1)$$

The formation energy is equal to difference between the total energy of the heterostructure and that of the individual MX_2 components. The *n* and *m* coefficients represent the number of unit cells for each MX_2 components. A negative formation energy indicates a stable heterostructure, while a positive formation energy suggests an energy penalty to form the heterostructure. This effective screening method narrowed the list of candidates for energetically favor lateral heterostructures. Using a converged supercell size and a denser k-point mesh we then performed density functional perturbation theory (DFPT)-based phonon calculations to validate the stabilities of the selected heterostructures. We found that both MoS_2-WS_2 and MoS_2-WSe_2 were stable.

Given that inducing strain on a lateral heterostructure has been shown to alter electronic properties[25] and that flexible electronic devices constantly undergo compression and tension, it is important from a fundamental and technological perspective to understand how strain affects the transport properties. In our studies, MoS_2-WS_2 and MoS_2-WSe_2 heterostructures underwent uniaxial compression and tension ranging from 0 to 10% in 2% increments applied perpendicular to the interface. To create the strained structure, the relaxed heterojunction structure was simulated. The length along the heterostructure was either increased or decreased using the following expression:

$$\varepsilon = \frac{L' - L}{L} = \frac{\Delta L}{L} \quad (2)$$

where ε refers to strain. L' is the calculated length of the strained heterostructure while L is the original, or relaxed, length of the heterostructure. With a denser k-point mesh, we calculated electronic density of states (DoS) and band structure to reveal the

effect of strain on the electronic properties. The DFT + U[32] scheme was applied with an on-site potential of 4.38 eV and 8.0 eV for Mo and W, respectively. Phonon density of states calculations were also performed to determine the strain effect on phonon scattering, suggesting a change in lattice thermal conductivity. To account for long-range effect 1x3x1 supercells were generated for the phonon calculations. Second-order force constants were generated using DFPT[33].

The calculated force constants were then used as inputs into the Atomistic Green's Function (AGF) code[34], which calculates the phonon transmission function for the interface of two materials and the transmission coefficients of individual phonon modes. For the phonon transmission function $\Theta(\omega)$, the system of interest consists of three components, including semi-infinite left lead, interfacial region, and semi-infinite right lead. $\Theta(\omega)$ corresponds to the total phonon transmission across the interface region and is computed from the AGF and depends on the phonon dispersion of the leads and the atomistic structure of the interface. The thermal boundary conductance (TBC) $G(T)$ can be computed as follows:[35]

$$G(T) = \frac{1}{2\pi}\int_0^\infty d\boldsymbol{\omega}\hbar\boldsymbol{\omega}\frac{dN(\omega,T)}{dT}\Theta(\omega) \qquad (3)$$

where *N* and *T* are the Bose-Einstein function and the temperature, respectively. This method has been implemented to graphene/BN system for validation[35].

4.3 Results and Discussion

4.3.1 Structural Features

MoS_2-WS_2 and MoS_2-WSe_2 heterostructures have been successfully fabricated by experiments[17,18] and have potential application in flexible electronics[36]. The calculated formation energies of MoS_2-WS_2 and MoS_2-WSe_2 are -0.0146 eV/atom and -0.13525 eV/atom, respectively. Our simulations revealed no significant structural distortion nor defect is observed at the interface, agreeing with the sharp interface observed in experiment[18,37]. The difference in lattice constants between individual monolayers MoS_2 and WS_2 is only 0.03%, while the MoS_2-WSe_2 lateral heterostructure has a lattice mismatch of 4.06%, which would easily induce a strain at the interface. The various bond lengths for MoS_2-WS_2 and MoS_2-WSe_2 heterostructures were calculated, and the results are summarized in Table 4.1. Comparing the bulk regions of MoS_2-WS_2 and MoS_2-WSe_2, the Mo-Mo distances are 3.18 Å and 3.19 Å while the W-W distances are 3.18 and 3.31, respectively. The distances between chalcogen pairs on the Mo side are smaller than those on the W side because the larger Se chalcogen atoms push the W atoms further apart from one another. Similarly, the Mo-W distances at the interface of MoS_2 – WS_2 are smaller than those at the interface of MoS_2-WSe_2.

Table 4.1 Computed bond lengths in the bulk and interfacial regions of lateral MoS_2-WS_2 and MoS_2-WSe_2 heterostructures, as well as the isolated MoS_2 and WS_2 materials, referred to Figure 1(b).

	Mo-Mo Å	W-W Å	S-S (Mo Side) Å	S /Se-S/Se (W Side) Å	Mo-W (Interface) Å
MoS_2 – WS_2	3.185	3.182	3.125	3.140	3.177
MoS_2 – WSe_2	3.189	3.310	3.107	3.374	3.312

MX_2	Band Gap (eV)	Band Alignment	M-M (Å)	X-X (Å)
MoS_2	1.69	Direct	3.182	3.138
WS_2	1.85	Direct	3.181	3.139
WSe_2	1.58	Direct	3.317	3.355

4.3.2 Electronic Properties

We induce compression and tension in each heterostructure to examine how uniaxial strain affects its electronic properties. The unstrained MoS_2-WS_2 has a direct band gap of 1.644 eV while the unstrained MoS_2-WSe_2 structure has a direct band gap of 1.351 eV, potentially advantageous for optoelectronic applications. Both band gaps are sensitive to uniaxial strain. Table 4.2 contains a summary of the electronic properties of the two heterostructures under tension and compression. Both heterostructures can undergo small amounts of compression and tension without significant degradation of their performance. The band gap in MoS_2-WS_2 reaches its maximum (1.736 eV) at 2% compression although it is highly sensitive to tensile forces. There is a dramatic drop in band gap for MoS_2 – WS_2 under tension. At 8% tension the band gap decreases by over

half of its original value. In contrast, a 10% compression decreases the band gap by only 10.22%. At all calculated strains, the band alignment of the MoS_2-WSe_2 lateral heterostructure shifts from direct to indirect. For MoS_2-WSe_2, the band gap variation for compression is 0.093 eV, implying that the band gap is relatively stable under compressive forces while the band gap variation for tension is 0.586 eV, implying that its band gap is more sensitive to tension. For both lateral heterostructures there is a dramatic drop in the band gap under tension, as can be seen in Table 2. Unlike the MoS_2-WS_2 lateral heterostructure, MoS_2-WSe_2 can sacrifice 25.24% of its band gap, and briefly return to a direct band gap alignment at 6% tension. The band gap will remain direct up to 2% compression, and benefits from 9.40% increase in band gap. It can be concluded that for both structures increasing amounts tension decreases the band gap while small compressive forces can increase the band gap. For device applications compression is best suited for band gap refinement for non-optoelectronic devices. The small amounts of tension can be applied on the structure without sacrificing its optoelectronic properties like band gap alignment.

Table 4.2 Summary on the calculated band gap for the lateral MoS_2-WS_2 and MoS_2 – WSe_2 heterostructures with tension and compression

MoS_2 – WS_2							
Unstrained Band gap: 1.644 eV (Direct)							
Tension				**Compression**			
Strain Percentage	E_g (eV)	% Change	Type	Strain Percentage	E_g (eV)	% Change	Type
2%	1.412	-14.11%	Indirect	2%	1.736	5.60%	Indirect
4%	1.192	-27.49%	Indirect	4%	1.677	2.01%	Indirect
6%	0.986	-40.02%	Indirect	6%	1.617	-1.64%	Indirect
8%	0.794	-51.70%	Indirect	8%	1.551	-5.66%	Indirect
10%	0.623	-62.10%	Indirect	10%	1.476	-10.22%	Indirect

MoS_2-WSe_2							
Unstrained Band gap: 1.351 eV (Direct)							
Tension				**Compression**			
Strain Percentage	E_g (eV)	% Change	Type	Strain Percentage	E_g (eV)	% Change	Type
2%	1.234	-8.66%	Indirect	2%	1.468	8.66%	Direct
4%	1.117	-17.32%	Indirect	4%	1.478	9.40%	Indirect
6%	1.01	-25.24%	Direct	6%	1.433	6.07%	Indirect
8%	0.899	-34.20%	Indirect	8%	1.384	2.44%	Indirect
10%	0.736	-45.52%	Indirect	10%	1.324	-2.00%	Indirect

Our band structure calculations further reveal the electronic band alignments with the induced strain. Figure 4.2 contains the band alignment and individual atomic contributions for the unstrained and strained MoS_2-WS_2 and MoS_2-WSe_2 lateral heterostructures. For the unstrained MoS_2-WS_2 heterostructure, a direct band gap is observed at the K point. The valence band maximum and conduction band minimum are contributed by the W and Mo atoms, respectively. It suggests that the band gap and band alignment are dominated by the choice of transition metals rather than chalcogen elements. We compare the unstrained band structure with 10% tension and 2% compression, which both significantly impact the band alignments. Figure 4.2(**a**) illustrates the drastic change in band structure MoS_2-WS_2 under 10% tension (red dashed curves) plotted against the unstrained heterostructure (black solid curves) as well as the individual atomic contributions at the band gaps. The valence bands shift to higher energies at the Γ and M points and become the valence band maximum. The Mo, W, and S atoms all contribute to the valence band shift, thereby closing the band gap. Conversely, the conduction band minimum at the Γ point splits into two new local minimums. This shift from a direct band gap to an indirect gap requires phonon displacement to excite an electron from the valence band to the conduction band. From 2 – 10% tension the band alignment remains indirect. Similar to tension, applying compression to the material shifts the band alignment from direct to indirect. Figure 4.2(**b**) is the band structure of MoS_2-WS_2 under 2% compression, compared to that of the unstrained heterostructure. The valence band of the structure with 2% compression (red dashed curves) shifts to the lower energy level, and opens up the band gap. The conduction band has a minimum between Γ and M points, which shifts the band gap to

indirect. Our computational results suggest that the MoS_2-WS_2 heterojunction can undergo slight compressive forces without sacrificing a large reduction in band gap size, but it shifts from direct to indirect.

Unlike MoS_2-WS_2, the band structure of MoS_2-WSe_2 is switched between direct and indirect with the induced strain. For the unstrained MoS_2-WSe_2 heterostructure, a direct band gap is observed at the K point, as seen in Figure 4.2. We compare it with 6% tension and 4% compression, which both manipulate the transition between direct and indirect band gaps. Figure 4.2(**c**) shows the band structure of the MoS_2-WSe_2 heterostructure at 6% tension (red dashed curves) in comparison to that of the unstrained band structure (black solid curves). The valence band is controlled by the metal W and Mo atoms under tension and towards the Fermi level, i.e. decreasing the band gap. The valence band maximum returns to the Γ point resulting in a direct band alignment. Small tensile forces can shift the band alignment of MoS_2-WSe_2 and dominate the overall performance if it is used in the flexible electronics. When MoS_2-WSe_2 induces compression its band gap increases and converges at 8% compression. It reaches a maximum band gap of 1.478 eV at 4% compression. Although compression increases the band gap, the direct band alignment is only maintained until 2% compression. Figure 4.2(**d**) is the band structure of MoS_2-WSe_2 under 4% compression, demonstrating the shift from a direct to indirect band gap. The conduction band splits at the Γ point, creating a new conduction band minimum. Compressive forces play a large role in the conduction band alignment while tensile forces dictate the valence band alignment.

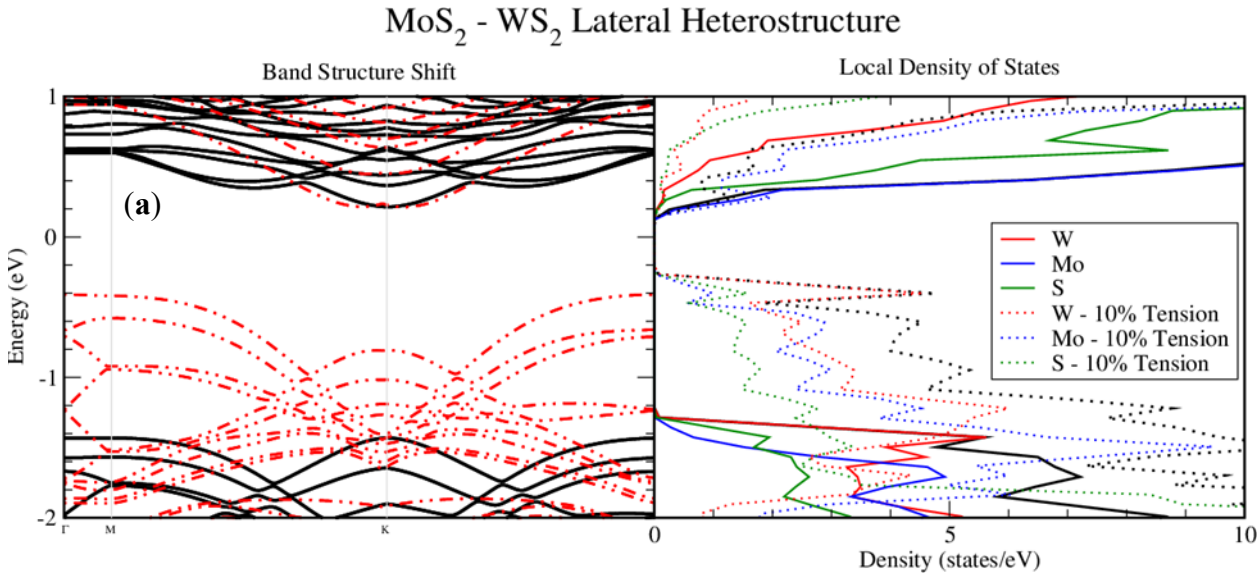
MoS2 - WS2 Lateral Heterostructure
Band Structure Shift
Local Density of States
(a)
Energy (eV)
Γ
M
K
Density (states/eV)
W
Mo
S
W - 10% Tension
Mo - 10% Tension
S - 10% Tension

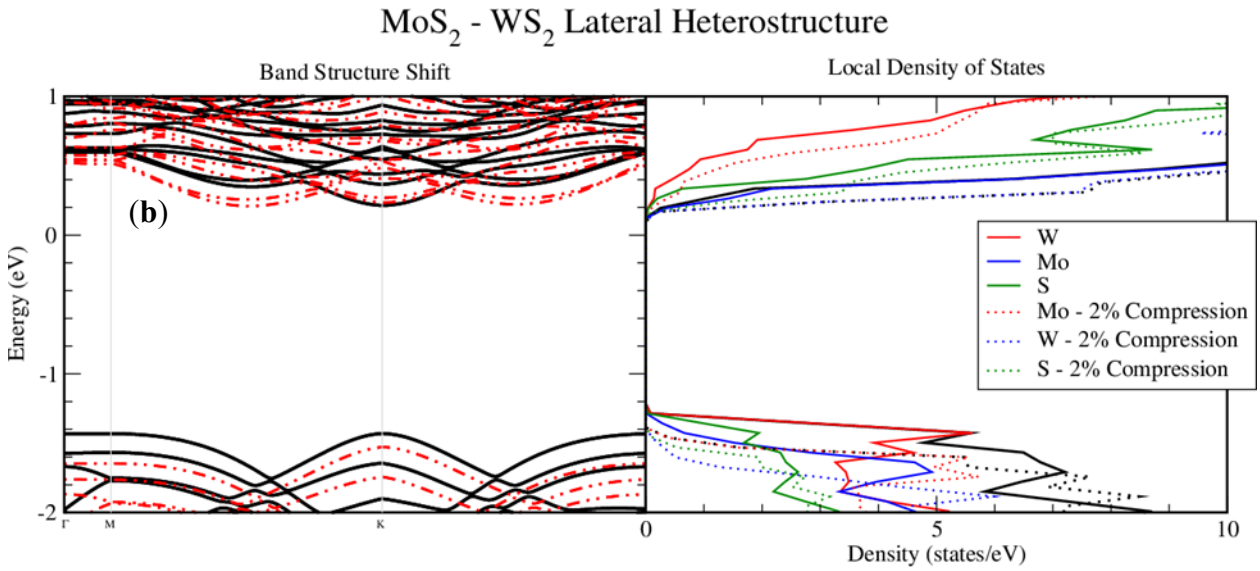
MoS2 - WS2 Lateral Heterostructure
Band Structure Shift
Local Density of States
(b)
Energy (eV)
Γ
M
K
Density (states/eV)
W
Mo
S
Mo - 2% Compression
W - 2% Compression
S - 2% Compression

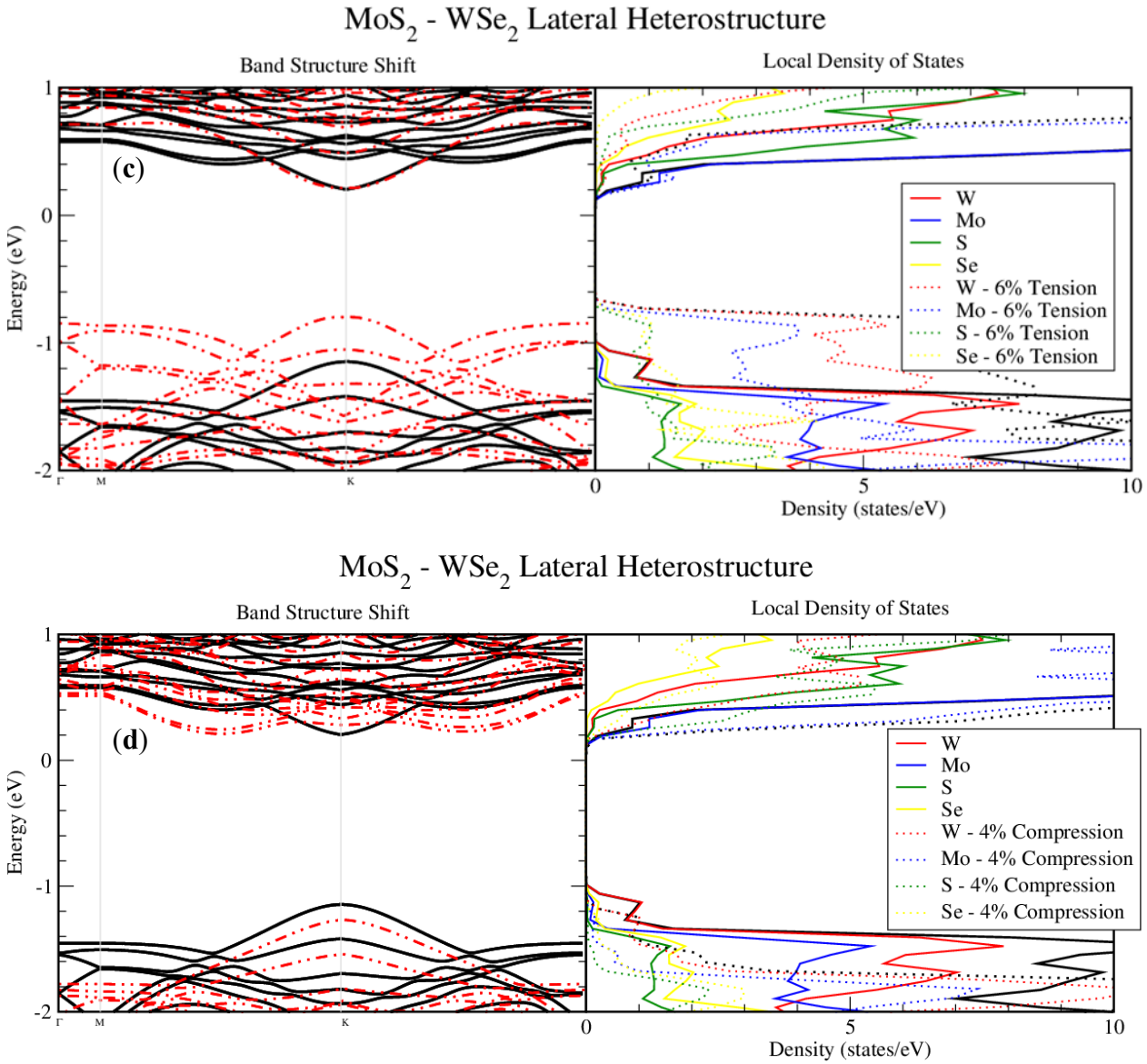

Figure 4.2. Calculated band structure of the MoS_2-WS_2 heterostructure undergoing (a) 10% tension and (b) 2% compression, in comparison with that of the MoS_2-WSe_2 heterostructure when undergoing (c) 6% tension and (d) 4% compression. The solid black line indicates the unstrained heterostructure while the dashed red line represents the same structure under strain.

4.3.3 Phonon Properties

Phonon calculations could reveal phonon scattering phenomenon and predict the lattice thermal conductivity changes of the heterostructures under tension and compression. We found that applying either tension or compression to the lateral MoS_2-WS_2 heterostructure does not generate negative phonon frequencies, suggesting its

structural stability. Its unstrained structure has a phonon frequency gap of 0.83 THz between the acoustic and optical regions, as seen in Figure 4.3(**a**). Increasing the amounts of tension and compression closes the phonon frequency gap, suggesting an increase in phonon scattering. The phonon frequencies are projected along the armchair and zigzag (i.e. along *a* and *b* directions in Figure 4.1, respectively) directions to understand the strain effect on the phonon modes. Figure 4.3(**a**) shows an isotropic feature along the two directions of the unstrained structure. The armchair and zigzag directions contribute relatively equally to the in-plane phonon DoS. To highlight the effects of strain both 10% tension and 10% compression are also plotted. In Figure 4.3(**b**) the phonon frequencies are no longer isotropic. The acoustic and optical modes split at approximately 4 and 9 THz, respectively. Phonon vibrations along the armchair direction dominate the lower frequencies of the acoustic and optical modes. Compressive forces reveal the opposite trend. The acoustic and optical modes split around 5 and 11 THz, respectively, and the zigzag direction dominates the lower frequencies of the acoustic and optical modes, as seen in Figure 4.3(**c**). We found that strain splits the directionality of the phonon contributions, where tensile forces shifts the armchair direction contribution to the lower frequencies, while compressive forces shifts the zigzag direction contribution to the lower frequencies. In both tension and compression we found that the zigzag direction peak in the optical mode remains at 11 THz. The interface is aligned in the armchair direction, which explains how sensitive the phonon contributions are along the armchair direction.

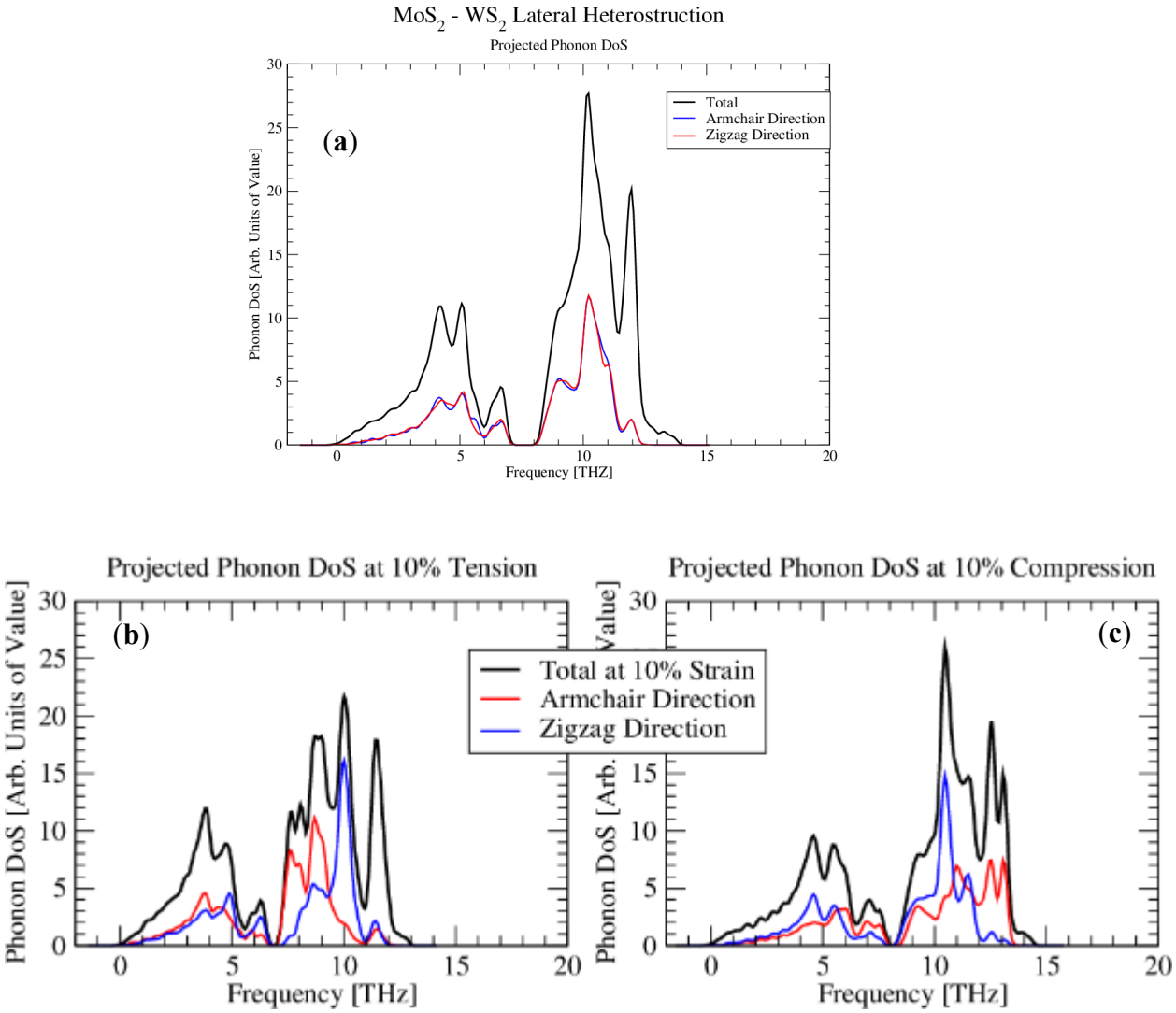

Figure 4.3. The projected the phonon density of states of the lateral MoS_2 – WS_2 heterostructure along the armchair and zigzag direction for the (a) unstrained, (b) 10% tension, and (c) 10% compression structures.

The lateral MoS_2-WSe_2 heterostructure is composed of two chalcogens with different atomic weights. Figure 4.3-4.4 shows no negative phonon frequencies with tension and compression, indicating that MoS_2-WSe_2 is stable under strain. There is also no phonon frequency gap between the acoustic and optical modes, suggesting the higher phonon scattering and lower lattice thermal conductivity than those in MoS_2-WS_2 due to atomic weight difference. Projecting the phonon DoS along the armchair and zigzag

directions of the lateral MoS_2 – WSe_2 heterostructure reveals the effects of the different chalcogens. In the unstrained structure (Figure 4.4(**a**)) the armchair and zigzag directions do not contribute as equally to the total phonon DoS due to the atomic weight difference of two chalcogen elements. Applying tension creates a sharp peak at approximately 7 THz, but it does not create any significant further distortion in the phonon density of states, as seen in Figure 4.4(**b**). With compression the phonon DoS has the fewer fluctuations, as seen in Figure 4.4(**c**). One significant change with the induced compression is a sharp peak at 12 THz in the highest-frequency of the optical mode. The acoustic mode of the unstrained structure has the armchair direction dominating the lowest frequencies. However, under compression zigzag direction switches and overpowers the lower frequencies. Clearly, the different atomic weights of the chalcogen species play a significant role in the directionality of the phonon DoS, resulting in phonon scattering mechanism and lattice thermal conductivity.

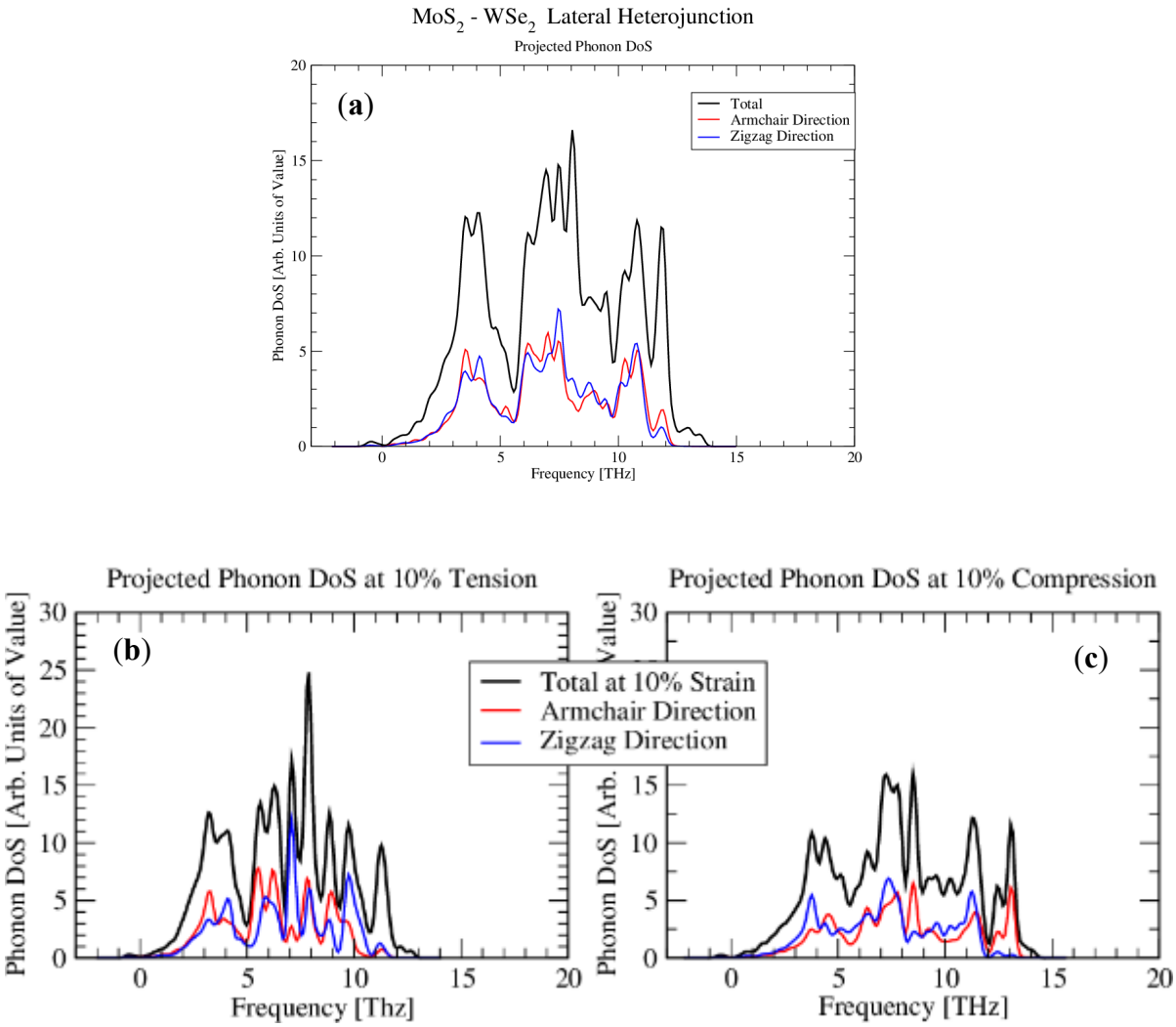

Figure 4.4. The projected the phonon density of states of the lateral MoS_2 – WSe_2 heterostructure along the armchair and zigzag direction for the (a) unstrained, (b) 10% tension, and (c) 10% compression structures.

4.3.4 Interfacial Thermal Resistance

With a phonon frequency gap, MoS_2 – WS_2 heterostructure is expected to have the higher lattice thermal conductivity than MoS_2 – WS_2, and its interface plays a crucial role to control phonon scattering mechanism. We used the extended AGF to investigate interfacial phonon transmission and thermal transport at the MoS_2-WS_2 interface. Figure 4.5 shows the transmission coefficient spectra for the longitudinal (LA), transverse (TA) and flexural (ZA) acoustic phonons at the MoS_2-WS_2 interface. The different colors

indicate the transmission coefficient or fraction of energy transmitted across the interface by each phonon mode. The gray-shaded points correspond to phonon modes that do not impinge on the interface and do not contribute to the interfacial heat flux. Figure 4.5 (a, c & e) show the rightward interfacial heat flux contribution from MoS_2 phonons while Figure 4.5 (b, d &f) show the leftward interfacial heat flux contribution from WS_2 phonons. In general, the phonons with long wavelengths and low frequencies, closing to the center of the Brillouin zone, have transmission coefficients of 1, i.e. 100% transmitted across the interface. As we move away from the center of the Brillouin zone towards the zone boundaries, the phonon have higher frequencies and smaller transmission coefficients, i.e. the they become more strongly scattered at the interface. Interestingly, for the phonon transmission from the WS_2 side, we observe a "critical angle" beyond which no transmission is observed. This "critical angle" is akin to that in optics and is due to the heavier W atoms, which leads to lower acoustic phonon group velocities in WS_2. In addition, the transmission coefficients also depend on the frequency alignment of phonons with similar polarizations in MoS_2 and WS_2. As phonon velocities in MoS_2 are generally higher than those in WS_2, we have a wider angular distribution of phonon modes that contributes to the heat flux.

Figure 4.6 shows the total boundary conductance (TBC) as a function of temperature. The TBC increases with temperature because of more populated phonon modes that contribute to interfacial thermal transport. The acoustic phonons dominate the TBC for all temperatures. At 300 K, the contribution from the optical phonons, i.e. the difference between the overall and acoustic phonon-dominated TBC curves in Figure 4.6, only comprises about 16% of the TBC. Even though the optical phonon contribution is

small, it can be a source of discrepancy if not considered in the computation of the TBC, specifically at high temperatures. The MoS_2-WS_2 TBC converges to ~351MWK^{-1}m^{-2} at 300K, an order of magnitude smaller than the graphene/*h*-BN TBC of 2.5 GWK^{-1}m^{-2}.[30] This is the consequence of the lower acoustic phonon velocities in MoS_2 and WS_2, which limit their maximum interfacial heat flux. Although this currently only applies to the unstrained MoS_2-WS_2 interface we plan on extending the code to include the MoS_2-WSe_2 heterostructure. The code will also calculate the photo transmission coefficient on the two heterostructures at 10% compression and tension to understand how uniaxial strain affects the interfacial properties in our future work.

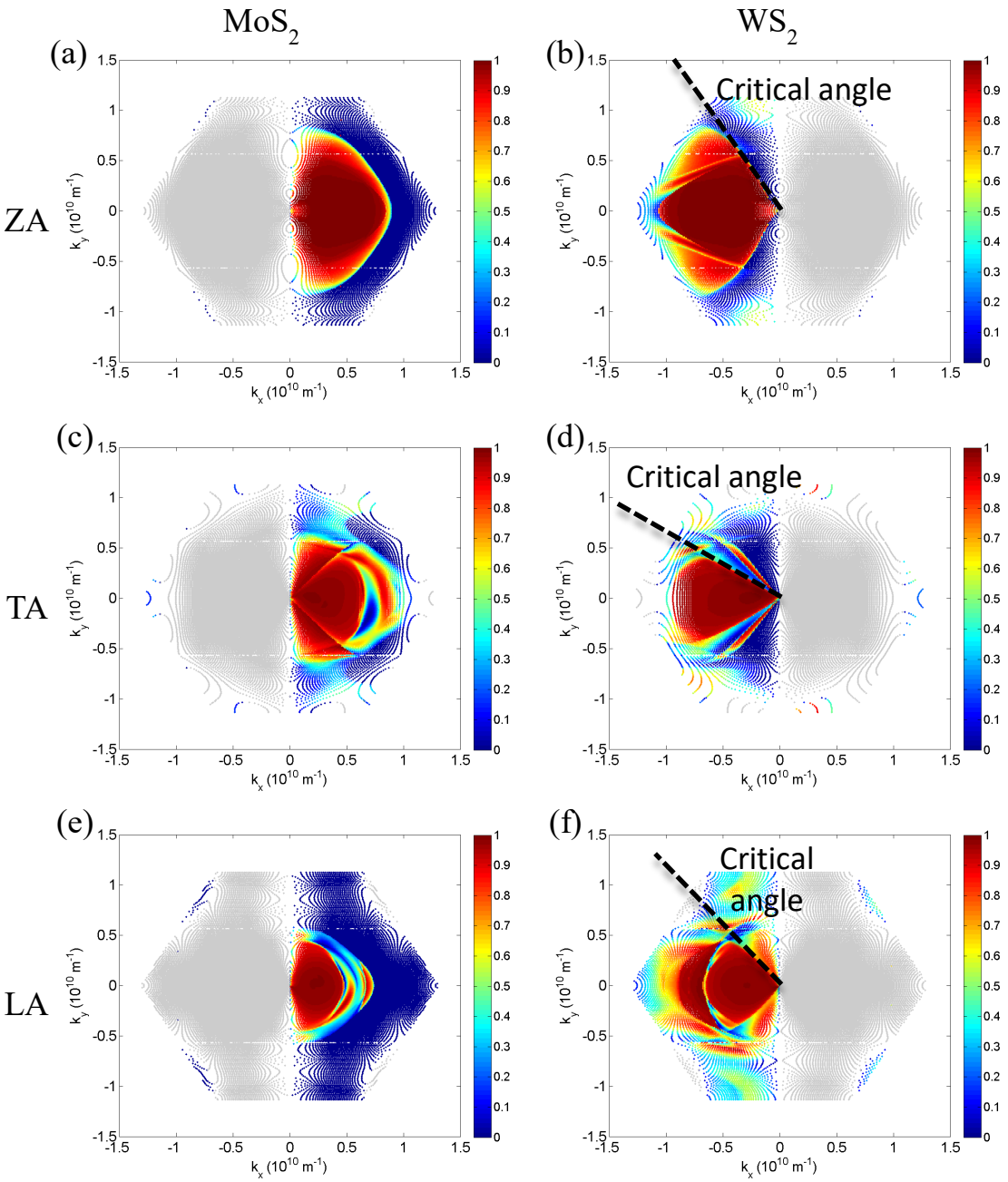

Figure 4.5. Phonon transmission coefficients across the MoS_2-WS_2 interface for the ZA (a and b), TA (c and d), and LA (e and f) acoustic phonon modes. The left column (a, c, and e) represents MoS_2 phonons contributing to leftward interfacial heat flux whereas the right column (b, d, and f) represents WS_2 phonons contributing to rightward interfacial heat flux.

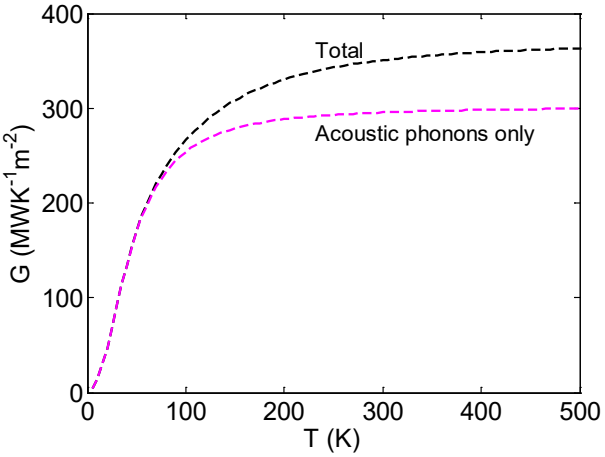

Figure 4.6. Thermal boundary conductance (TBC) for MoS_2-WS_2 lateral interface. The dotted black plot represents the total TBC for the system and the dotted pink plot represents the TBC contribution from the acoustic phonon modes.

4.4 Conclusions

We utilized DFT-based methods to examine a stain effect on the electronic and phonon properties of lateral MoS_2-WS_2 and MoS_2-WSe_2 heterostructures. They were strained from 0 -10% for compression and tension at 2% intervals. The unstrained MoS_2-WS_2 heterostructure has an indirect band gap of 1.649 eV. Small compressive forces, such as< 4%, slightly increase the band gap while the band gap decreases with the compression of > 4%. Tension also decreases the band gap, but at a much faster rate. The unstrained MoS_2-WSe_2 heterostructure has a direct band gap of 1.316 eV. The compressive forces not only increase the band gap size but also switch between direct and indirect. Further studies on the strain effect on the structural stability and phonon scattering were conducted using phonon density of states calculations. No imaginary phonon frequencies occur for MoS_2-WS_2 or MoS_2-WSe_2 heterostructures under compression and tension, indicating the structures remain stable. Increasing the compressive forces applied to MoS_2-WS_2 shifts its acoustic mode to the higher frequencies, and minimizes its phonon gap between the acoustic and optical modes,

suggesting an increase in the phonon scattering and a decrease in the lattice thermal conductivity. Increasing tensile forces achieves the opposite scenario, where the optical mode shifts to the lower frequencies. The in-plane phonon contributions can also be manipulated through tension and compression. Different types of chalcogenide elements in the MoS_2-WSe_2 heterostructure induce the stronger phonon scattering than that in the MoS_2-WS_2. Increasing both compressive and tensile forces also creates the higher frustrations in the phonon modes, leading to an increase in the phonon mean free path. The projected phonon DoS highlights the anisotropy of the MoS_2 – WSe_2 heterostructure, derived from the different chalcogen species. Our studies show that the TBC at the MoS_2-WS_2 interface is dominated by the acoustic phonons. The optical phonons have a small but significant contribution to the TBC at high temperatures. In comparison with the graphene/*h*-BN interface, the calculated TBC of the MoS_2-WS_2 heterostructure is an order of magnitude smaller due to the lower acoustic phonon velocities. This may potentially be a source of impediment to efficient heat dissipation in nanoelectronic devices with such interfaces. Our studies can guide flexible electronic and photovoltaic material and device design.

Data Availability and Acknowledgements:

The raw/processed data required to reproduce these findings cannot be shared at this time as the data also forms part of an ongoing study. This research made use of the resources of the High Performance Computing Center at Idaho National Laboratory, which is supported by the Office of Nuclear Energy of the U.S. Department of Energy and the Nuclear Science User Facilities under Contract No. DE-AC07-05ID14517. We would also like to acknowledge high-performance computing support of the R2 compute

cluster (DOI: 10.18122/B2S41H) provided by Boise State University's Research Computing Department.

References

1 Branimir Radisavljevic, Aleksandra Radenovic, Jacopo Brivio, i V. Giacometti, and A. Kis, Nature nanotechnology **6** (3), 147 (2011).

2 K. F. Mak, C. Lee, J. Hone, J. Shan, and T. F. Heinz, Phys Rev Lett **105** (13), 136805 (2010).

3 H. Terrones, F. Lopez-Urias, and M. Terrones, Scientific reports **3**, 1549 (2013).

4 Weijie Zhao, Ricardo Mendes Ribeiro, Minglin Toh, Alexandra Carvalho, Christian Kloc, AH Castro Neto, and Goki Eda, Nano letters **13** (11), 5627 (2013).

5 KK Kam and BA Parkinson, The Journal of Physical Chemistry **86** (4), 463 (1982).

6 Kin Fai Mak, Changgu Lee, James Hone, Jie Shan, and Tony F Heinz, Physical review letters **105** (13), 136805 (2010).

7 Wencan Jin, Po-Chun Yeh, Nader Zaki, Datong Zhang, Jerzy T Sadowski, Abdullah Al-Mahboob, Arend M van Der Zande, Daniel A Chenet, Jerry I Dadap, and Irving P Herman, Physical review letters **111** (10), 106801 (2013).

8 Andrea Splendiani, Liang Sun, Yuanbo Zhang, Tianshu Li, Jonghwan Kim, Chi-Yung Chim, Giulia Galli, and Feng Wang, Nano letters **10** (4), 1271 (2010).

9 Jason K Ellis, Melissa J Lucero, and Gustavo E Scuseria, Applied Physics Letters **99** (26), 261908 (2011).

10 S Lebegue and O Eriksson, Physical Review B **79** (11), 115409 (2009).

11 Agnieszka Kuc, Nourdine Zibouche, and Thomas Heine, Physical Review B **83** (24), 245213 (2011).

12 Y. Yoo, Z. P. Degregorio, and J. E. Johns, Journal of the American Chemical Society **137** (45), 14281 (2015).

[13] Yongji Gong, Junhao Lin, Xingli Wang, Gang Shi, Sidong Lei, Zhong Lin, Xiaolong Zou, Gonglan Ye, Robert Vajtai, and Boris I Yakobson, Nature materials **13** (12), 1135 (2014).

[14] R. D. Vispute, V. Talyansky, S. Choopun, R. P. Sharma, T. Venkatesan, M. He, X. Tang, J. B. Halpern, M. G. Spencer, Y. X. Li, L. G. Salamanca-Riba, A. A. Iliadis, and K. A. Jones, Applied Physics Letters **73** (3), 348 (1998).

[15] Christian Teichert, Physics Reports **365** (5), 335 (2002).

[16] R. S. Sundaram, M. Engel, A. Lombardo, R. Krupke, A. C. Ferrari, P. Avouris, and M. Steiner, Nano Lett **13** (4), 1416 (2013).

[17] Kun Chen, Xi Wan, Jinxiu Wen, Weiguang Xie, Zhiwen Kang, Xiaoliang Zeng, Huanjun Chen, and Jian-Bin Xu, ACS nano **9** (10), 9868 (2015).

[18] Ming-Yang Li, Yumeng Shi, Chia-Chin Cheng, Li-Syuan Lu, Yung-Chang Lin, Hao-Lin Tang, Meng-Lin Tsai, Chih-Wei Chu, Kung-Hwa Wei, and Jr-Hau He, Science **349** (6247), 524 (2015).

[19] A. Nourbakhsh, A. Zubair, M. S. Dresselhaus, and T. Palacios, Nano Lett **16** (2), 1359 (2016).

[20] Izaak Williamson, Shasha Li, Andres Correa Hernandez, Matthew Lawson, Yue Chen, and Lan Li, Chemical Physics Letters **674**, 157 (2017).

[21] Qianwen Wang, Ping Wu, Gengyu Cao, and Min Huang, Journal of Physics D: Applied Physics **46** (50), 505308 (2013).

[22] Wei Wei, Ying Dai, and Baibiao Huang, Physical Chemistry Chemical Physics **18** (23), 15632 (2016).

[23] Yuzheng Guo and John Robertson, Applied Physics Letters **108** (23), 233104 (2016).

[24] Won Seok Yun, S. W. Han, Soon Cheol Hong, In Gee Kim, and J. D. Lee, Physical Review B **85** (3) (2012).

[25] Jun Kang, Hasan Sahin, and François M. Peeters, The Journal of Physical Chemistry C **119** (17), 9580 (2015).

[26] Jaekwang Lee, Jingsong Huang, Bobby G Sumpter, and Mina Yoon, 2D Materials **4** (2), 021016 (2017).

[27] G Kresse, Phys. Rev. B **54**, 11 (1996).

[28] John P Perdew, Kieron Burke, and Matthias Ernzerhof, Physical review letters **77** (18), 3865 (1996).

[29] Weijie Zhao, Ricardo Mendes Ribeiro, Minglin Toh, Alexandra Carvalho, Christian Kloc, AH Neto, and Goki Eda, arXiv preprint arXiv:1309.0923 (2013).

[30] Izaak Williamson, Andres Correa Hernandez, Winnie Wong-Ng, and Lan Li, JOM **68** (10), 2666 (2016).

[31] TE Graedel, EM Harper, NT Nassar, Philip Nuss, and Barbara K Reck, Proceedings of the National Academy of Sciences **112** (14), 4257 (2015).

[32] AI Liechtenstein, VI Anisimov, and J Zaanen, Physical Review B **52** (8), R5467 (1995).

[33] Atsushi Togo and Isao Tanaka, Scripta Materialia **108**, 1 (2015).

[34] Zhun-Yong Ong, Journal of Applied Physics **124** (15), 151101 (2018).

[35] Z. Y. Ong and G. Zhang, Phys Rev B **91** (17), 174302 (2015).

[36] Deep Jariwala, Vinod K Sangwan, Lincoln J Lauhon, Tobin J Marks, and Mark C Hersam, ACS nano **8** (2), 1102 (2014).

[37] Kun Chen, Xi Wan, Weiguang Xie, Jinxiu Wen, Zhiwen Kang, Xiaoliang Zeng, Huanjun Chen, and Jianbin Xu, Advanced materials **27** (41), 6431 (2015).

CHAPTER FIVE: FIRST-PRINCIPLES STUDIES OF MOF_6 ABSORPTION ON HYDROXYLATED AND NON-HYDROXYLATED METAL OXIDE SURFACES AND IMPLICATIONS FOR ATOMIC LAYER DEPOSITION OF MOS_2

This chapter is published by Elsevier in *Applied Surface Science* and should be referenced appropriately.

Reference:

M. Lawson, E. Graugnard, L. Li, "First-principles studies of MoF_6 absorption on hydroxylated and non-hydroxylated metal oxide surfaces and implications for atomic layer deposition of MoS_2" *Applied Surface Science*. **541** 148461 (2021).

First-principles studies of MoF_6 absorption on hydroxylated and non-hydroxylated metal oxide surfaces and implications for atomic layer deposition of MoS_2

Matthew Lawson[a]

Elton Graugnard[a]

and Lan Li[a,b]

Published In:

Applied Surface Science

2021

[a]*Micron School of Materials Science and Engineering,*

Boise State University, Boise, ID 837062

[b]*Center for Advanced Energy Studies,*

Idaho Falls, ID 83401

Abstract

Significant interest in two-dimensional transition metal dichalcogenides has led to numerous experimental studies of their synthesis using scalable vapor phase methods, such as chemical vapor deposition (CVD) and atomic layer deposition (ALD). ALD typically allows lower deposition temperatures, and nucleation of chemical precursors requires reactions with surface functional groups. A common first-principles method used to study ALD modeling is the calculation of activation energy for a proposed reaction pathway. In this work we calculated the partial charge densities, local density of states (LDoS), Bader charge analysis, adsorption energies, and charge density difference using density functional theory (DFT) to investigate the nucleation of MoF_6 on three oxide surfaces, including Al_2O_3, HfO_2, and MgO. Our findings indicate that hydroxyl groups (OH) help lower the reaction barrier during the first half-cycle of MoF_6 and promote the chemisorption of a precursor on the oxide substrates. This discovery is supported by the formation of highly ionic MF_x (M = metal, x = 1, 2, 3) bonds at the oxide surfaces. By comparing surfaces with and without hydroxyl groups, we highlight the importance of surface chemistry.

5.1 Introduction

Due to their atomic structures and unique properties, there has been tremendous interest in semiconducting two-dimensional (2D) materials, especially transition metal dichalcogenides (TMDs), which have a composition MX_2 (M = transition metal, X = chalcogen), with a range of band gaps[1] and unique properties[1-7]. An interesting feature of certain TMD materials is the shift of electronic bands when transitioning from bulk to monolayer[1,8]. Specifically, monolayer MoS_2 becomes a direct band gap semiconductor

with a gap of 1.8 eV, whereas its bulk phase has an indirect band gap of 1.3 eV[1,8]. Due to its novel physical and chemical properties, 2D MoS_2 has drawn attention for its wide range of applications[9] such as electrocatalysis[10-13], photocatalysis[14-17], batteries[18-21], biological applications[22-25], sensors[26-31], and electronic devices[1,32-35].

2D-MoS_2 has been grown via chemical vapor deposition (CVD), but the high substrate temperatures[36-38] and lack of self-limiting growth[39,40] have prompted further investigations into alternative methods, such as atomic layer deposition (ALD). Unlike more common CVD techniques, the highly reactive precursor gases for ALD are introduced sequentially into the reactor and never mixed simultaneously[41]. This results in two half-reactions created by each precursor species and its respective surface. The reactions are limited by the number of available surface sites. Sequential cycling of the precursors limits the growth during cycles, and results in precise atomic thickness control. In semiconductor device manufacturing, low *k* dielectric materials are used for interconnect or "Back End of the Line" applications. Their low melting temperatures restrict the process temperature to around 400 °C[42]. In CVD of TMDs, the substrate temperature is typically much higher than this upper limit, making it impractical for integration into semiconductor device fabrication[43]. However, ALD can operate at a much lower temperature making it feasible[41].

A number of studies have reported the ALD processes of TMDs, such as MoS_2 and WS_2, using a variety of precursors[44-58]. Most of these processes yield amorphous as-deposited films, which can be crystallized upon annealing. One such process uses MoF_6 and H_2S to grow amorphous MoS_2 at 200 °C[52,53]. The initial half reaction of this process introduces MoF_6 to an oxide surface (e.g., atomic layer deposited aluminum oxide,

Al_2O_3). Critically, this first half reaction controls the nucleation of the film, only forming a three-atom thick monolayer. Complementary to in situ quartz crystal microbalance (QCM) and Fourier transform infrared (FTIR) spectroscopy characterization, density functional theory (DFT) calculations can be employed to gain insight into various reaction pathways that occur during initial ALD growth[59]. Specifically, DFT can not only explore potential reaction pathways efficiently but also investigate precursor-substrate interactions and quantify electron exchange[60,61]. Here, we report the use of DFT method to investigate the electronic interactions of a single MoF_6 precursor and three surfaces, including Al_2O_3, HfO_2, and MgO. These oxide materials are widely used in the semiconducting industry ranging from optical applications[62], high-*k* gate dielectrics[63], to catalysis[64]. To simulate the surface reactions, the bulk structures of the substrates were cleaved to expose both oxygen and metal atoms in the vacuum. Recent DFT studies on ALD have found that hydroxylated SiO_2 can facilitate MoS_2 growth[65,66]. Hydroxyl groups also facilitate ALD of Si[67], Hf[68], ZnO[69], and more[70]. Building from this insight, we explored nucleation reactions on surfaces without hydroxyl groups (non-hydroxylated) and those with hydrogen atoms terminating the oxygen atoms (hydroxylated). The results indicated that hydroxyl groups are crucial for the nucleation of MoS_2 on these oxide surfaces.

5.2 Methods

We employed DFT calculations using the Vienna Ab initio Simulation Package (VASP)[71] and Perdew-Burke-Enzerhof (PBE)[72] pseudopotentials with the generalized gradient approximation (GGA) exchange correlation functions. Projector-augmented wave (PAW) pseudopotentials were used. In order to improve the accuracy of the

calculations, a cut-off energy of 400 eV was chosen, and residual forces were reduced to 0.01 eV/atom. A vacuum greater than 15 Å was introduced to mitigate spurious interactions. The surfaces were cleaved from relaxed bulk structures, and supercells were generated to increase surface area and underwent another full relaxation. A Γ-centered 5x5x1 k-point mesh was implemented on all surfaces during geometry optimization.

Our initial results and cited literature indicated that ALD simulations converged within a reasonable timeframe when both metal and O atoms terminated at the surface, thus the (110), (100), and (100) surfaces for HfO_2 [73], MgO[74-76], and Al_2O_3 [77,78] respectively were cleaved from their bulk counterparts. Dimensions and images of the relaxed surfaces were generated using the VESTA[79] program, and are provided in Appendix A. The potential reactivities of surfaces with and without hydroxyl groups were compared by calculating partial charge densities. Next, an MoF_6 precursor was introduced at least 5 Å above the surfaces and underwent a full geometry optimization. To investigate the electronic interactions between precursor and surfaces, local density of states (LDoS) was calculated. The rotationally invariant LSDA+U[80] on site coulombic potentials of 4.38 eV and 4.0 eV were included for the Mo and Hf atoms respectively, and a denser 10x10x1 k-point mesh was implemented. To quantify and compare MoF_6 interactions between the hydroxylated and non-hydroxylated surfaces, Bader charge analysis was employed. Bader charge analysis quantifies the degree of chemical interaction between atoms[81], and is a quantitative method that allows us to study the effect of hydroxyl groups on precursor decomposition[60,61]. Finally, the adsorption energy of the MoF_6 precursor was calculated to determine the degree of physisorption or chemisorption. The adsorption energy (E_{ads}) was calculated, as follows:

$$E_{ads} = E_{total\ system} - E_{surface} - E_{MoF_6}$$

where $E_{total\ system}$ is the total energy of the surface with precursor, $E_{surface}$ is the total energy of a surface, and E_{MoF_6} is the total energy of a single isolated MoF_6 precursor.

5.3 Results and Discussion

5.3.1 Surface Reactivity

To explore surface reactivities, the partial charge densities of the initial surfaces were computed. In Figure 5.1, the partial charge densities are projected along the *a* axis for the non-hydroxylated Al_2O_3, HfO_2, and MgO substrates. The color scale shows charge density integrated for each material from -1 eV to the Fermi energy. This energy range examines the edge states of the valence band, where electrons participate in chemical bonding. The calculated partial charge densities for the non-hydroxylated surfaces demonstrate the chemically stable surfaces. The charge densities are uniform in each surface and localized around the lattice atoms of all three substrates. The contour lines indicate the regions of equal partial charge densities. Our results suggest that the non-hydroxylated surfaces are not highly reactive. They cannot facilitate MoF_6 deposition, because the charge densities are distributed evenly around the atoms.

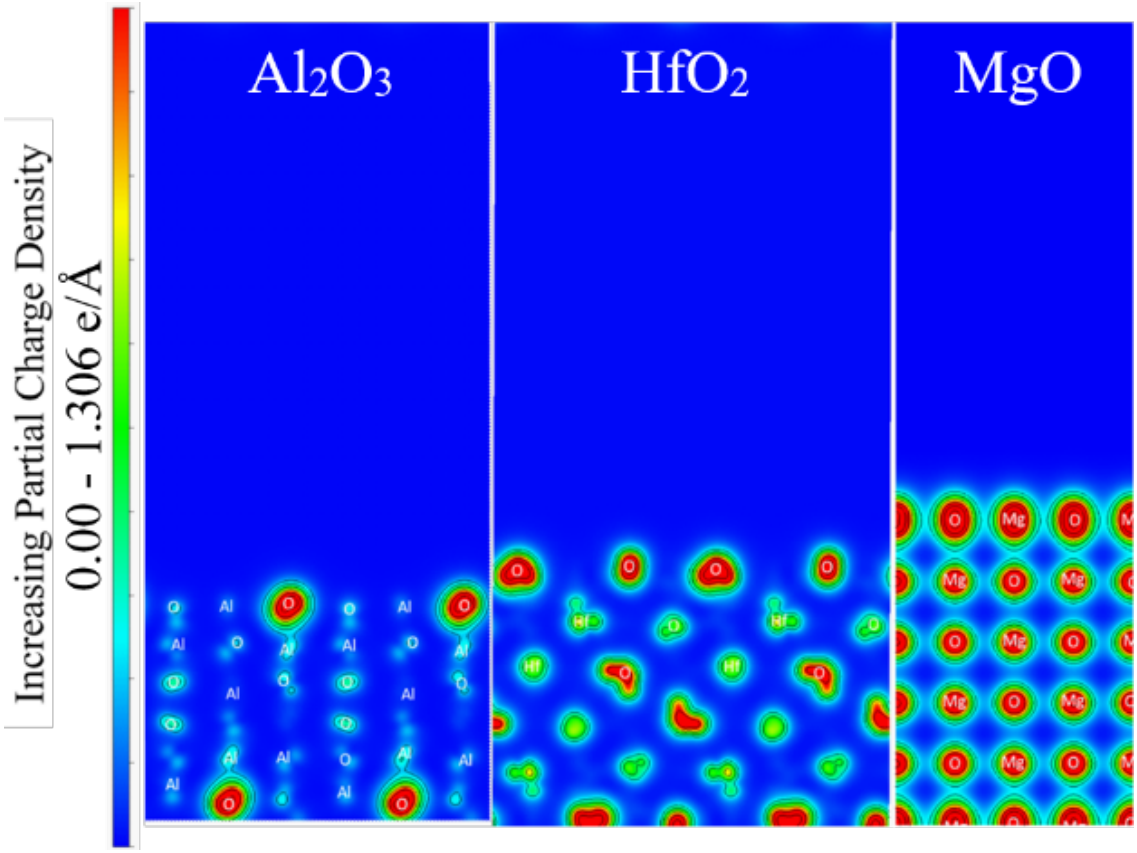

Figure 5.1. A cross section of the partial charge densities projected along the *a* axis for the non-hydroxylated Al_2O_3, HfO_2, and MgO substrates from -1 eV to the Fermi energy (color online).

Adding hydroxyl groups clearly changes the profile of partial charge densities. Figure 5.2 plots the partial charge densities along the *a* axis for the hydroxylated Al_2O_3, HfO_2, and MgO substrates from -1 eV to the Fermi energy, where the densities are concentrated at the surfaces. The profile at the surface varies across substrates. The partial charge densities for hydroxylated Al_2O_3 substrate is localized in small "pockets" close to the O atoms at the surface, and the same phenomenon is observed with the HfO_2 substrate. The electron "pockets" extend to the OH groups, but they are concentrated at the terminating Hf atoms. The partial charge densities for MgO contains a uniform electron cloud extending across the hydroxyl groups at the surface. Our results highlight the importance of the hydroxyl groups, which could redistribute electrons at the surfaces.

Hydroxyl groups appear to increase the reactivity of the surface and provide an increase in electron density. Furthermore, the electrons become delocalized, which could promote the chemical bonding of the MoF_6 precursor to the surface.

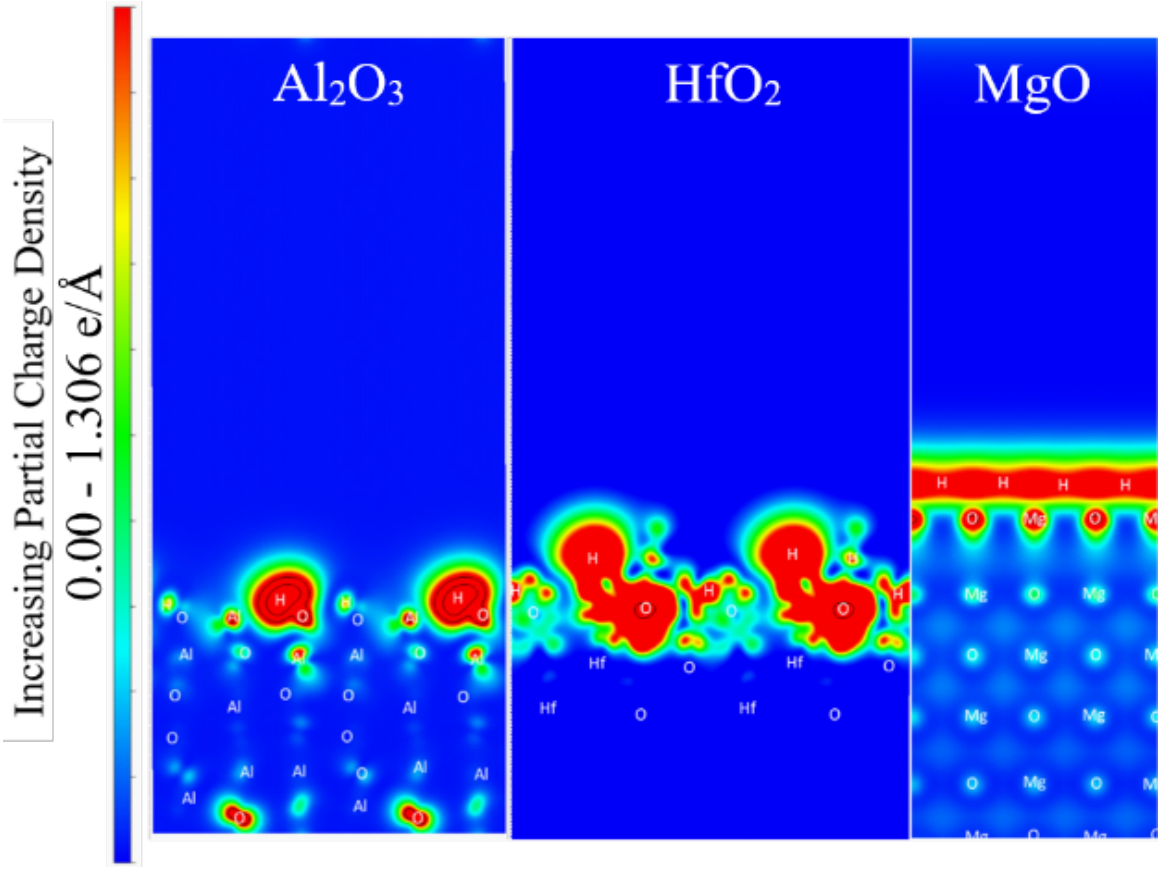

Figure 5.2. A cross section of the partial charge densities projected along the *a* axis for the hydroxylated Al_2O_3, HfO_2, and MgO substrates from -1 eV to the Fermi energy (color online).

5.3.2 Precursor Adsorption

To understand the interactions between the non-hydroxylated substrates and the precursor, a single MoF_6 molecule was introduced into the system and underwent a full geometry relaxation. There was no significant structural distortion on any of the surfaces. The LDoS was calculated for each substrate to explore bonding characteristics and electronic interactions. Figure 5.3 splits the electronic contributions of the surface (in red)

and precursor (in blue) for all three non-hydroxylated substrates. The Fermi energy is shifted to 0, and negative energy E states below the Fermi energy are primarily occupied by the surface. The surfaces do not have overlapping states with the MoF_6 precursor at the Fermi energy. These findings suggest little electronic interaction between the non-hydroxylated surfaces and the MoF_6 precursor. Physisorption is the dominant surface mechanism for the non-hydroxylated surfaces. Later sections will quantify these interactions[82].

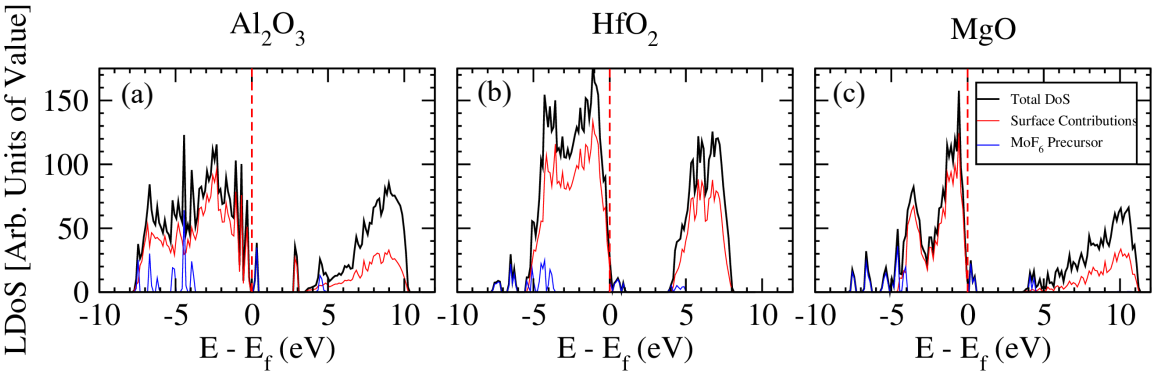

Figure 5.3. The LDoS for the fully relaxed MoF_6 above the non-hydroxylated (a) Al_2O_3, (b) HfO_2, and (c) MgO substrates. The legend applies to all three substrates.

The partial charge density calculations suggest that the presence of hydroxyl groups enhances the surface reactivity. The LDoS for each hydroxylated substrate with the MoF_6 precursor is plotted in Figure 5.4, revealing the electronic interactions during deposition. We hypothesized that the electron "pockets" above the hydroxylated Al_2O_3 and HfO_2 substrates in Figure 5.2 would promote chemical reactions. Figure 5.4 (a) and (b) show small mid gap states forming below the Fermi energy, and the broadening of the LDoS peaks, which indicates hybridization and chemical bond formation[82]. The hydroxylated MgO substrate in Figure 5.4 (c) demonstrates similar behavior, however,

the MoF_6 precursor creates two small mid gap states, above and below the Fermi energy, at -0.5 and 0.5 eV, and the surface also contributes to these mid gap states.

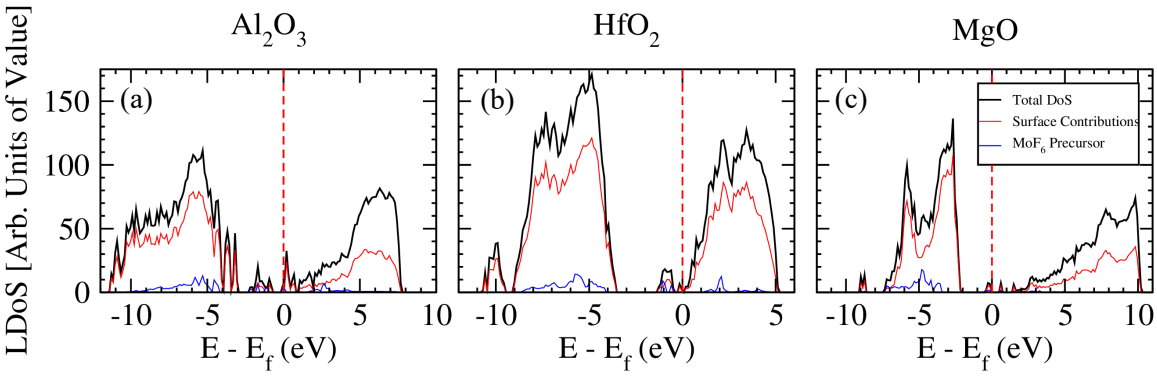

Figure 5.4. The LDoS for the fully relaxed MoF_6 above the (a) Al_2O_3, (b) HfO_2, and (c) MgO hydroxylated substrates. The legend applies to all three substrates.

In comparison between Figures 5.3 and 5.4, the LDoS results for the non-hydroxylated substrates do not show an overlap at the Fermi energy, suggesting no chemical interaction. The LDoS results for the hydroxylated substrates demonstrate the strong surface-precursor interactions stemming from the formation and overlapping of mid gap states. Specifically, Figures 5.4 (a) and (b) indicate that the surface and precursor both contribute to the states at and near the Fermi energy and show increased bond hybridization, resulting in a strong precursor-surface chemisorption interaction. Figure 5.4 (c) has fewer overlapping states at the Fermi energy between the surface and precursor. Overall, these mid gap states are derived from the precursor, so further investigation is needed to quantify the physisorption and chemisorption interactions. The LDoS calculations for the non-hydroxylated and hydroxylated substrates reveal two important findings. The first is that non-hydroxylated substrates experience physisorption

with the precursor and little electronic interaction. The second is that the hydroxylated surfaces hybridization occurs, leading to chemisorption.

5.3.3 Electronic Interaction Between Precursor and Surface

The partial charge densities reveal that hydroxylated substrates have an increased surface reactivity and confirm our hypothesis that hydroxyl groups facilitate chemical reactions with MoF_6. The LDoS results suggest precursor-surface physisorption on the non-hydroxylated substrates and precursor-surface chemisorption on the hydroxylated substrates. To better quantify the interactions, we employed Bader charge analysis and calculated the adsorption energies of the precursor on three surfaces. Both can serve as the methods to discern between physical versus chemical interactions as well as quantify the strength of adsorption[81]. Table 5.1 lists the Bader charge analysis and adsorption energies for the non-hydroxylated and hydroxylated substrates with a single MoF_6 precursor. The Δ Bader is calculated by subtracting the hydroxylated Bader charge values by the non-hydroxylated Bader charge values.

Table 5.1 The calculated Bader charge analysis for the non-hydroxylated and hydroxylated substrates in presence of a single MoF_6 precursor. A negative Bader charge value means the atomic species is donating valence electrons while a positive value means the atomic species is gaining valence electrons. The adsorption energy of a single MoF_6 precursor E_{ads} is also calculated to quantify the strength of the interaction.

	Al2O3			HfO2			MgO		
Atomic Species	Non-hydroxylated Bader Charge	Hydroxylated	Δ Bader	Non-hydroxylated Bader Charge	Hydroxylated	Δ Bader	Non-hydroxylated Bader Charge	Hydroxylated	Δ Bader
Mo	-2.75	-1.53	1.22	-2.46	-1.94	0.51	-2.44	-2.09	0.35
F	0.45	0.70	0.25	0.47	0.63	0.16	0.44	0.62	0.18
F	0.45	0.92	0.46	0.42	0.62	0.20	0.44	0.62	0.18
F	0.46	0.86	0.40	0.50	0.70	0.19	0.58	0.79	0.21
F	0.46	0.85	0.39	0.57	0.69	0.12	0.53	0.81	0.28
F	0.47	0.85	0.39	0.47	0.70	0.23	0.53	0.79	0.26
F	0.45	0.71	0.25	0.49	0.72	0.24	0.44	0.61	0.17
Total F	2.75	4.88	2.13	2.93	4.07	1.14	2.95	4.24	1.29
Eads (eV/MoF6)	-0.07	-9.95		-0.45	-6.42		-0.57	-20.56	

For complete physisorption we would expect the sum of the Bader charges for the six F atoms from the precursor to be equal to the Bader charge of the central metal Mo atom. Thus, the Mo atom would distribute its available electrons to the surrounding F atoms, and weak van der Waals forces would hold the precursor to the surface. In Table 5.1, Total F is the sum of the Bader charge for the F atoms from the MoF_6 precursor. The Bader charge for the metal Mo atom is more negative above the non-hydroxylated surfaces than the hydroxylated surface and is equal to the sum Bader charge for the F atoms. These results indicate Mo-F bonds in the precursor are stronger than the chemical bonds formed between the F atoms and the non-hydroxylated surfaces, suggesting physisorption. The opposite trend is observed above the hydroxylated surfaces. The Mo atom above the hydroxylated surface has a less negative Bader charge than the non-hydroxylated surface, and the sum Bader charge for the F atoms also increases. The Mo-F bonds become weaker while the F-surface bonds become stronger, suggesting chemisorption. We attribute the formation of the F-surface bonds due to the electrons contributed by the hydroxylated surfaces.

Chemisorption occurs with the hydroxylated surfaces, because the Bader charge for the F atoms becomes more positive and the metal Mo becomes less negative. To further determine the magnitude of chemisorption, we calculated the adsorption energies in Table 5.1. The adsorption energy is negative above the non-hydroxylated and hydroxylated surfaces, which implies that for all systems the precursor will be adsorbed to the surface. However, the adsorption energy varies greatly between the non-hydroxylated and hydroxylated surfaces. The adsorption energies for the MoF_6 precursor above the non-hydroxylated surfaces are all less than 0.50 eV/MoF_6. This result, coupled

with the LDoS in Figure 5.3 and Bader charge in Table 5.1, confirms our hypothesis that physisorption is the dominant mechanism on these non-hydroxylated surfaces. Conversely, the adsorption energies of the MoF_6 precursor above the hydroxylated Al_2O_3, HfO_2, and MgO are -9.95 eV/MoF_6, -6.42 eV/MoF_6, and -20.56 eV/MoF_6, respectively. We attribute the extremely negative adsorption energy for MoF_6 on hydroxylated MgO to the H_2 gas that forms above the surface as seen in SI 4. These significantly more negative adsorption energies, coupled with the hybridization in the LDoS in Figure 5.4 and Bader charge analysis in Table 5.1, indicate chemisorption, caused by the changes in the surface electronic properties in the presence of hydroxyl groups.

To map the location and redistribution of the electron densities, the charge density difference is plotted in Figure 5.5 for the non-hydroxylated and hydroxylated Al_2O_3 with a single MoF_6 precursor. The charge density difference is calculated using the equation provided in Appendix A and supplies the residual charge density for the electrons contributing upon adsorption. Blue and yellow regions indicate a gain or loss of electrons, respectively. Upon the adsorption of MoF_6, the non-hydroxylated Al_2O_3 reveals an increase in charge density (blue isosurfaces) between the bonds of the Mo-F atoms while there is a decrease in charge density (yellow isosurfaces) at the bonds between the F atoms and surface (Figure 5.5 (a)). The charge density at the surface redistributes around the surface Al atoms, but it does not appear to participate in bonding. These findings indicate that the non-hydroxylated surface has a weak interaction with an MoF_6 precursor, evidencing that physisorption occurs. The hydroxylated Al_2O_3 surface in Figures 5.5 (b) shows a sharp contrast in charge density. Upon the adsorption of MoF_6, there is a large increase in the charge density between the surface and F atoms (blue

isosurfaces) that extends to the metal Mo atom. This drastic increase in the charge density suggests the covalent bonding characteristics observed during the ALD process. The partial charge density findings are consistent with the HfO_2 and MgO substrates, and those partial charge density plots can be found in the Appendix A.

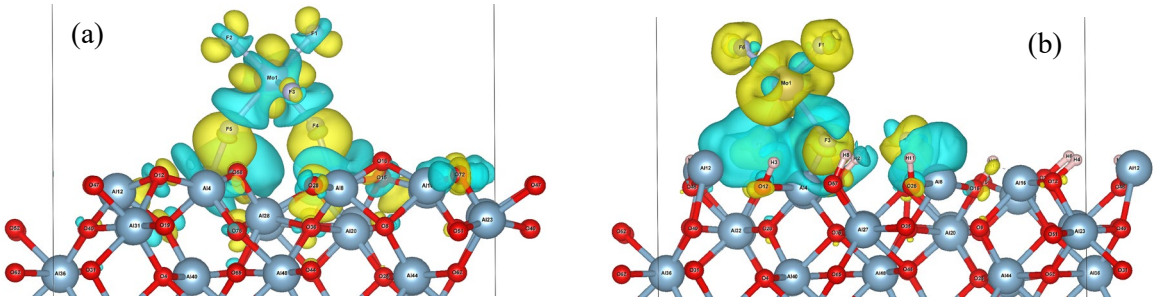

Figure 5.5. Charge density difference for the non-hydroxylated (a) and hydroxylated (b) Al_2O_3 with MoF_6. The yellow and blue regions indicate a loss and gain of electrons, respectively. The plotted charge density difference highlights the covalent behavior that forms with hydroxylated surfaces.

5.4 Discussions

Our work highlights the importance of hydroxyl groups in consistent with prior DFT works[65,67-70,83]. Hydroxyl groups control the first half-cycle for ALD of MoS_2. Treated Al_2O_3, HfO_2, and MgO substrates without hydroxyl groups are less reactive and do not appear to facilitate deposition. Precursor-surface chemisorption is observed on the hydroxylated substrates, but the precursor bonds do not form with the hydroxyl groups. Differences between the oxide surfaces could also play an important role in deposition. While all three oxides have high melting temperatures and large band gaps the crystal structures vary. The highly ionic MgO has a cubic structure where the valence states of Mg and O are 2^+ and 2^- respectively. The Mg and O exchange electrons and form inherently strong Mg-O bonds. The addition of hydroxyl groups at the surface could

break these inherently strong bonds and facilitate deposition. The valence state of HfO_2 is similar to MgO. The valence states of Hf and O are 2^+ and 2^- respectively, but HfO_2 has a distinctly different crystal structure. HfO_2 has a more complicated bonding structure with 7-coordinated Hf atom centers. ALD on HfO_2 could depend on the surface termination due to the number of O atoms, and therefor hydroxyls. The Al_2O_3 substrate has valence states of 3^+ and 2^- for Al and O respectively, which resulted in a different bonding structure. Al_2O_3 was extremely sensitive to the hydroxyl groups, and two F atoms dissociated onto the surface. The 3^+ valence state of Al helped form highly ionic AlF_3.

This work is unique because we identify highly ionic MF_x-surface bonds during the first half cycle of MoF_6. We attribute this to an increase in the electron densities around the Mo atom of the precursor and the surface O atoms which forms chemical bonds. For the MoF_6 precursor, a low operation temperature (i.e., or a high hydroxyl concentration) could result in the ionic MF_x surface bonds that appear to be a driving thermodynamic factor and potentially could control nucleation. Ultimately, Mo-O bonds are present in experimental growth, and they play an important role forming low dimensional MoS_2. We propose that the formation of Mo-O bonds is controlled by the hydroxyl concentration. Hydroxyl groups and their densities can vary surface reactivity and change surface chemistry, leading to a controlling nucleation of ALD. The quality of the grown films is dependent on the choice of substrate. Our computational results indicate that an area-selective ALD can be achieved through surface chemistry modification.

5.5 Conclusions

We present a comprehensive first-principles study of the substrates with and without hydroxyl groups for ALD of MoS_2 using MoF_6 on Al_2O_3, HfO_2, and MgO. DFT-based methods were used to calculate quantum interactions during the first half-cycle with MoF_6 in order to gain detailed insight into the nucleation process. We studied the precursor and surface interactions by calculating their partial charge densities, LDoS, Bader charge analysis, and adsorption energies. The partial charge densities reveal that the surfaces become more reactive in the presence of hydroxyl groups. The surface composition also affects the partial charge density distribution. The LDoS results demonstrate that the non-hydroxylated surfaces have little to no electronic interactions with the MoF_6 precursor while the hydroxylated surfaces experience some degree of bond hybridization. The Bader charge analysis quantitatively demonstrates that the non-hydroxylated surfaces form a weak interaction with the precursor through physisorption while the hydroxylated surfaces strongly interact with the MoF_6 precursor through chemisorption. Finally, the calculated adsorption energies highlight this difference. Substrates without hydroxyl groups have low adsorption energies of -0.45, -0.57, and -0.07 eV/MoF_6 for HfO_2, MgO, and Al_2O_3, respectively. Coupling these low adsorption energies with their respective LDoS calculations and Bader charge values, we suggest that physisorption is the dominant mechanism on the non-hydroxylated surfaces. Conversely, the adsorption energies of the fully hydroxylated surfaces increase to -9.95, -6.42, and -20.56 eV/MoF_6 for Al_2O_3, HfO_2, and MgO, respectively. Coupling their respective LDoS calculations, Bader charge values, and adsorption energies with the charge density difference figures, we suggest that chemisorption is the dominant

mechanism above hydroxylated surfaces. Our study also highlights the importance of substrate choice and how different substrates react with the precursor, and indicate the potential for area-selective ALD.

Acknowledgments

This research made use of the resources of the High Performance Computing Center at Idaho National Laboratory, which is supported by the Office of Nuclear Energy of the U.S. Department of Energy and the Nuclear Science User Facilities under Contract No. DE-AC07-05ID14517. We would also like to acknowledge high-performance computing support of the R2 compute cluster (DOI: 10.18122/B2S41H) provided by Boise State University's Research Computing Department. This work was supported in part by an NSF CAREER Grant No. 1751268. We thank Jake Soares, JD Hues, Steve Hues, and Jeffrey Elam for valuable discussions.

References

[1] Qing Hua Wang, Kourosh Kalantar-Zadeh, Andras Kis, Jonathan N Coleman, and Michael S Strano, Nature nanotechnology **7** (11), 699 (2012).

[2] Yongji Gong, Junhao Lin, Xingli Wang, Gang Shi, Sidong Lei, Zhong Lin, Xiaolong Zou, Gonglan Ye, Robert Vajtai, and Boris I Yakobson, Nature materials **13** (12), 1135 (2014).

[3] Wen Huang, Xin Luo, Chee Kwan Gan, Su Ying Quek, and Gengchiau Liang, Physical Chemistry Chemical Physics **16** (22), 10866 (2014).

[4] Xiaokun Gu and Ronggui Yang, Applied Physics Letters **105** (13), 131903 (2014).

[5] Matthew Lawson, Izaak Williamson, Zhun-Yong Ong, and Lan Li, Computational Condensed Matter, e00389 (2019).

[6] Izaak Williamson, Shasha Li, Andres Correa Hernandez, Matthew Lawson, Yue Chen, and Lan Li, Chemical Physics Letters **674**, 157 (2017).

[7] Izaak Williamson, Andres Correa Hernandez, Winnie Wong-Ng, and Lan Li, JOM **68** (10), 2666 (2016).

[8] Manish Chhowalla, Hyeon Suk Shin, Goki Eda, Lain-Jong Li, Kian Ping Loh, and Hua Zhang, Nature chemistry **5** (4), 263 (2013).

[9] Xiao Zhang, Zhuangchai Lai, Chaoliang Tan, and Hua Zhang, Angewandte Chemie International Edition **55** (31), 8816 (2016).

[10] Min-Rui Gao, Maria KY Chan, and Yugang Sun, Nature communications **6**, 7493 (2015).

[11] Jakob Kibsgaard, Zhebo Chen, Benjamin N Reinecke, and Thomas F Jaramillo, Nature materials **11** (11), 963 (2012).

[12] Junfeng Xie, Hao Zhang, Shuang Li, Ruoxing Wang, Xu Sun, Min Zhou, Jingfang Zhou, Xiong Wen Lou, and Yi Xie, Advanced materials **25** (40), 5807 (2013).

[13] Shengjie Xu, Dian Li, and Peiyi Wu, Advanced Functional Materials **25** (7), 1127 (2015).

[14] Junze Chen, Xue-Jun Wu, Lisha Yin, Bing Li, Xun Hong, Zhanxi Fan, Bo Chen, Can Xue, and Hua Zhang, Angewandte Chemie International Edition **54** (4), 1210 (2015).

[15] Yang Hou, Zhenhai Wen, Shumao Cui, Xiaoru Guo, and Junhong Chen, Advanced materials **25** (43), 6291 (2013).

[16] Anders B Laursen, Søren Kegnæs, Søren Dahl, and Ib Chorkendorff, Energy & Environmental Science **5** (2), 5577 (2012).

[17] Weijia Zhou, Zongyou Yin, Yaping Du, Xiao Huang, Zhiyuan Zeng, Zhanxi Fan, Hong Liu, Jiyang Wang, and Hua Zhang, small **9** (1), 140 (2013).

[18] Kun Chang and Weixiang Chen, ACS nano **5** (6), 4720 (2011).

[19] Shujiang Ding, Jun Song Chen, and Xiong Wen Lou, Chemistry–A European Journal **17** (47), 13142 (2011).

[20] Yun-Xiao Wang, Shu-Lei Chou, David Wexler, Hua-Kun Liu, and Shi-Xue Dou, Chemistry–A European Journal **20** (31), 9607 (2014).

[21] Fei Zhou, Sen Xin, Hai-Wei Liang, Lu-Ting Song, and Shu-Hong Yu, Angewandte Chemie International Edition **53** (43), 11552 (2014).

[22] Liang Cheng, Jingjing Liu, Xing Gu, Hua Gong, Xiaoze Shi, Teng Liu, Chao Wang, Xiaoyong Wang, Gang Liu, and Huaiyong Xing, Advanced materials **26** (12), 1886 (2014).

[23] Stanley S Chou, Bryan Kaehr, Jaemyung Kim, Brian M Foley, Mrinmoy De, Patrick E Hopkins, Jiaxing Huang, C Jeffrey Brinker, and Vinayak P Dravid, Angewandte Chemie International Edition **52** (15), 4160 (2013).

[24] Teng Liu, Chao Wang, Xing Gu, Hua Gong, Liang Cheng, Xiaoze Shi, Liangzhu Feng, Baoquan Sun, and Zhuang Liu, Advanced materials **26** (21), 3433 (2014).

[25] Wenyan Yin, Liang Yan, Jie Yu, Gan Tian, Liangjun Zhou, Xiaopeng Zheng, Xiao Zhang, Yuan Yong, Juan Li, and Zhanjun Gu, ACS nano **8** (7), 6922 (2014).

[26] Jong-Seon Kim, Hae-Wook Yoo, Hyung Ouk Choi, and Hee-Tae Jung, Nano letters **14** (10), 5941 (2014).

[27] F Keith Perkins, Adam L Friedman, Enrique Cobas, PM Campbell, GG Jernigan, and Berend T Jonker, Nano letters **13** (2), 668 (2013).

[28] Yang Tan, Ruiyun He, Chen Cheng, Dong Wang, Yanxue Chen, and Feng Chen, Scientific reports **4**, 7523 (2014).

[29] Zongyou Yin, Hai Li, Hong Li, Lin Jiang, Yumeng Shi, Yinghui Sun, Gang Lu, Qing Zhang, Xiaodong Chen, and Hua Zhang, ACS nano **6** (1), 74 (2011).

[30] Zhiyuan Zeng, Zongyou Yin, Xiao Huang, Hai Li, Qiyuan He, Gang Lu, Freddy Boey, and Hua Zhang, Angewandte Chemie International Edition **50** (47), 11093 (2011).

[31] Changfeng Zhu, Zhiyuan Zeng, Hai Li, Fan Li, Chunhai Fan, and Hua Zhang, Journal of the American Chemical Society **135** (16), 5998 (2013).

[32] Rudren Ganatra and Qing Zhang, ACS nano **8** (5), 4074 (2014).

[33] Xiao Huang, Zhiyuan Zeng, and Hua Zhang, Chemical Society Reviews **42** (5), 1934 (2013).

[34] Kangho Lee, Hye-Young Kim, Mustafa Lotya, Jonathan N Coleman, Gyu-Tae Kim, and Georg S Duesberg, Advanced materials **23** (36), 4178 (2011).

[35] Juqing Liu, Zhiyuan Zeng, Xiehong Cao, Gang Lu, Lian-Hui Wang, Qu-Li Fan, Wei Huang, and Hua Zhang, Small **8** (22), 3517 (2012).

[36] Yi-Hsien Lee, Xin-Quan Zhang, Wenjing Zhang, Mu-Tung Chang, Cheng-Te Lin, Kai-Di Chang, Ya-Chu Yu, Jacob Tse-Wei Wang, Chia-Seng Chang, and Lain-Jong Li, Advanced materials **24** (17), 2320 (2012).

[37] Jianping Shi, Donglin Ma, Gao-Feng Han, Yu Zhang, Qingqing Ji, Teng Gao, Jingyu Sun, Xiuju Song, Cong Li, and Yanshuo Zhang, ACS nano **8** (10), 10196 (2014).

[38] Yongjie Zhan, Zheng Liu, Sina Najmaei, Pulickel M Ajayan, and Jun Lou, Small **8** (7), 966 (2012).

[39] Yu-Chuan Lin, Wenjing Zhang, Jing-Kai Huang, Keng-Ku Liu, Yi-Hsien Lee, Chi-Te Liang, Chih-Wei Chu, and Lain-Jong Li, Nanoscale **4** (20), 6637 (2012).

[40] Xi Ling, Yi-Hsien Lee, Yuxuan Lin, Wenjing Fang, Lili Yu, Mildred S Dresselhaus, and Jing Kong, Nano letters **14** (2), 464 (2014).

[41] Steven M George, Chemical reviews **110** (1), 111 (2009).

[42] Hyungjun Kim, Journal of Vacuum Science & Technology B: Microelectronics and Nanometer Structures Processing, Measurement, and Phenomena **21** (6), 2231 (2003).

[43] Hugh O Pierson, *Handbook of chemical vapor deposition: principles, technology and applications*. (William Andrew, 1999).

[44] TW Scharf, SV Prasad, MT Dugger, PG Kotula, RS Goeke, and RK Grubbs, Acta Materialia **54** (18), 4731 (2006).

[45] TW Scharf, Somuri V Prasad, TM Mayer, RS Goeke, and MT Dugger, Journal of materials research **19** (12), 3443 (2004).

[46] Robert Browning, Prasanna Padigi, Raj Solanki, Douglas J Tweet, Paul Schuele, and David Evans, Materials Research Express **2** (3), 035006 (2015).

[47] Stéphane Cadot, Olivier Renault, Mathieu Frégnaux, Denis Rouchon, Emmanuel Nolot, Kai Szeto, Chloé Thieuleux, Laurent Veyre, Hanako Okuno, and François Martin, Nanoscale **9** (2), 538 (2017).

[48] Thi Anh Ho, Changdeuck Bae, Seonhee Lee, Myungjun Kim, Josep M Montero-Moreno, Jong Hyeok Park, and Hyunjung Shin, Chemistry of Materials **29** (17), 7604 (2017).

[49] Yujin Jang, Seungmin Yeo, Hyungjun Kim, and Soo-Hyun Kim, Applied Surface Science **365**, 160 (2016).

[50] Zhenyu Jin, Seokhee Shin, Do Hyun Kwon, Seung-Joo Han, and Yo-Sep Min, Nanoscale **6** (23), 14453 (2014).

[51] Titel Jurca, Michael J Moody, Alex Henning, Jonathan D Emery, Binghao Wang, Jeffrey M Tan, Tracy L Lohr, Lincoln J Lauhon, and Tobin J Marks, Angewandte Chemie International Edition **56** (18), 4991 (2017).

[52] Steven Letourneau, Matthias J Young, Nicholas M Bedford, Yang Ren, Angel Yanguas-Gil, Anil U Mane, Jeffrey W Elam, and Elton Graugnard, ACS Applied Nano Materials **1** (8), 4028 (2018).

[53] Anil U Mane, Steven Letourneau, David J Mandia, Jian Liu, Joseph A Libera, Yu Lei, Qing Peng, Elton Graugnard, and Jeffrey W Elam, Journal of Vacuum Science & Technology A: Vacuum, Surfaces, and Films **36** (1), 01A125 (2018).

[54] Miika Mattinen, Timo Hatanpää, Tiina Sarnet, Kenichiro Mizohata, Kristoffer Meinander, Peter J King, Leonid Khriachtchev, Jyrki Räisänen, Mikko Ritala, and Markku Leskelä, Advanced Materials Interfaces **4** (18), 1700123 (2017).

[55] Dip K Nandi, Uttam K Sen, Devika Choudhury, Sagar Mitra, and Shaibal K Sarkar, Electrochimica Acta **146**, 706 (2014).

[56] Seokhee Shin, Zhenyu Jin, Do Hyun Kwon, Ranjith Bose, and Yo-Sep Min, Langmuir **31** (3), 1196 (2015).

[57] Lee Kheng Tan, Bo Liu, Jing Hua Teng, Shifeng Guo, Hong Yee Low, and Kian Ping Loh, Nanoscale **6** (18), 10584 (2014).

[58] Arturo Valdivia, Douglas J Tweet, and John F Conley Jr, Journal of Vacuum Science & Technology A: Vacuum, Surfaces, and Films **34** (2), 021515 (2016).

[59] D. Elliott Simon, Semiconductor Science and Technology **27** (7), 074008 (2012).

[60] Liang Huang, Bo Han, Bing Han, Agnes Derecskei-Kovacs, Manchao Xiao, Xinjian Lei, Mark L O'Neill, Ronald M Pearlstein, Haripin Chandra, and Hansong Cheng, Physical Chemistry Chemical Physics **16** (34), 18501 (2014).

[61] Juan Radilla, Guillermo E Negrón-Silva, Manuel Palomar-Pardavé, Mario Romero-Romo, and Marcelo Galván, Electrochimica Acta **112**, 577 (2013).

[62] Shuzheng Shi, Shuo Qian, Xiaojuan Hou, Jiliang Mu, Jian He, and Xiujian Chou, Advances in Condensed Matter Physics **2018**, 7598978 (2018).

[63] Charmaine Chia, Max M. Shulaker, J. Provine, Stefanie S. Jeffrey, and Roger T. Howe, ACS applied materials & interfaces **11** (29), 26082 (2019).

[64] Xuhui Feng, Fuping Pan, Huilei Zhao, Wei Deng, Peng Zhang, Hong-Cai Zhou, and Ying Li, Applied Catalysis B: Environmental **238**, 274 (2018).

[65] M Shirazi, WMM Kessels, and AA Bol, Physical Chemistry Chemical Physics **20** (24), 16861 (2018).

[66] Mahdi Shirazi, Wilhelmus Kessels, and Ageeth A Bol, Physical Chemistry Chemical Physics (2018).

[67] Yong-Chan Jeong, Seung-Bin Baek, Dae-Hee Kim, Ji-Su Kim, and Yeong-Cheol Kim, Applied Surface Science **280**, 207 (2013).

[68] Atashi B. Mukhopadhyay, Javier Fdez Sanz, and Charles B. Musgrave, Chemistry of Materials **18** (15), 3397 (2006).

[69] Jie Ren, Applied surface science **255** (11), 5742 (2009).

[70] Mahdi Shirazi and Simon D Elliott, Chemistry of Materials **25** (6), 878 (2013).

[71] G Kresse, Phys. Rev. B **54**, 11 (1996).

[72] John P Perdew, Kieron Burke, and Matthias Ernzerhof, Physical review letters **77** (18), 3865 (1996).

[73] Lu LI, Yi LI, Xin GUO, Yong-Fan ZHANG, and Wen-Kai CHEN, Acta Physico-Chimica Sinica **29** (5), 937 (2013).

[74] F Eskandari, SB Porter, M Venkatesan, P Kameli, K Rode, and JMD Coey, Physical Review Materials **1** (7), 074413 (2017).

[75] H-J Freund, Niklas Nilius, Thomas Risse, and Swetlana Schauermann, Physical Chemistry Chemical Physics **16** (18), 8148 (2014).

[76] Ashley R Head and Joachim Schnadt, JOM **68** (12), 3070 (2016).

[77] Jarosław Handzlik and Philippe Sautet, Journal of Catalysis **256** (1), 1 (2008).

[78] Aditya Shankar Sandupatla, Konstantinos Alexopoulos, Marie-Françoise Reyniers, and Guy B Marin, The Journal of Physical Chemistry C **119** (23), 13050 (2015).

[79] Koichi Momma and Fujio Izumi, Journal of applied crystallography **44** (6), 1272 (2011).

[80] AI Liechtenstein, VI Anisimov, and J Zaanen, Physical Review B **52** (8), R5467 (1995).

[81] W Tang, E Sanville, and G Henkelman, Journal of Physics: Condensed Matter **21** (8), 084204 (2009).

[82] M Scheffler and C Stampfl, Electronic structure **2**, 286 (2000).

[83] M Shirazi, WMM Kessels, and AA Bol, APL Materials **6** (11), 111107 (2018).

CHAPTER SIX: UNDERSTANDING ALD-GROWN MOS_2 BY COMBINING EXPERIMENTAL MEASUREMENTS AND FIRST-PRINCIPLES CALCULATIONS

In this work, we combine first-principles and experimental methods to investigate how the hydroxyl concentration affects atomic layer deposition (ALD) of MoS_2 using MoF_6 and H_2S on Al_2O_3. Density functional theory (DFT) was used to calculate adsorption energies, bond lengths, Bader charges, and reaction energy barriers. In conjunction, experimental measurements using quartz crystal microbalance (QCM), x-ray photoelectron spectroscopy (XPS), and residual gas analysis (RGA) were combined with the first-principles methods. The combination of DFT and experiment uncovered that hydroxyl groups play an import role during ALD of MoS_2 on Al_2O_3 because they promote the formation of highly ionic AlF_3. No gaseous byproducts are identified by both DFT and experiment during the first half-cycle of MoF_6, suggesting a two-part nucleation mechanism for MoS_2. This work leverages both DFT and experiment to understand and explain ALD of MoS_2.

*6.*1. Introduction

The nanoscale features and reduced working dimensionality of advanced electronic devices are driving factors for new materials and process development in the semiconductor industry[1]. Two-dimensional (2D) semiconducting materials, such as transition metal dichalcogenides (TMDs), are a viable option in new technologies[2]. For example, monolayer MoS_2 possesses a direct band gap of 1.8 eV, whereas the bulk phase possesses an indirect band gap of 1.3 eV[2,3]. The reduced dimensionality of MoS_2

provides novel physical and chemical properties, leading to a wide range of applications[4] such as electrocatalysis[5-8], photocatalysis[9-12], batteries[13-16], biological applications[17-20], sensors[21-26], and electronic devices[2,27-30]. 2D-MoS_2 can be exfoliated[24,31-33] or grown at the high temperatures using chemical vapor deposition[34-38] (CVD), but these methods cannot be implemented efficiently in the modern semiconductor industry due to either the relatively low yield of exfoliation or operation restrictions resulting from high substrate temperatures during CVD. To address these integration issues new processing methods such as atomic layer deposition (ALD) are being investigated.

ALD is a bottom-up growth technique that exploits the volatility of its precursors to grow high quality films at the nanoscale at the lower operation temperatures. ALD is a subset of CVD, however, unlike CVD the chemical precursors are never introduced simultaneously in the reactor[39]. The ALD reaction is characterized by two half-reactions created by the gas phase precursors and their respective surface. The first half-reaction occurs when the first precursor is introduced into the chamber and reacts with the bare substrate depositing a new thin film. The second half-reaction occurs when the second precursor is introduced into the chambers and reacts with the newly deposited film. ALD is a self-limiting process, because the gas phase precursors only react once with an available surface site resulting in precise atomic layer control[39]. TMDs such as MoS_2 and WS_2 have been grown via ALD by a wide range of precursors[40-54]. One specific chemistry used to grow amorphous MoS_2 is MoF_6 and H_2S at 200 °C[48,49], making this chemistry a potential candidate for low-temperature large-scale growth[48]. In order to form 2D-MoS_2 via ALD each half cycle of MoF_6 and H_2S must be thoroughly studied. Our previous first-principles work has identified the improved reactivity of MoF_6 on

hydroxylated alumina[55], prompting further studies to understand how MoF_6 deposition can be controlled.

ALD experiments suggested that hydroxyl groups (OH) could control deposition. X-ray photoelectron spectroscopy (XPS) is a surface characterization technique that analyzes the chemical composition of thin films. This tool is commonly used to validate the purity of ALD films[48,49], but has also identified hydroxyl groups on substrates by deconvoluting the oxygen peaks. Specifically, XPS has been used for precursor pulses to identify a change in hydroxyl concentration during the ALD process[56-60]. These studies indicated that incoming precursor molecules react with the substrate by removing hydroxyl groups at the surface. Fourier-transform infrared spectroscopy (FTIR) has been also utilized to explore hydroxyl groups on surfaces before deposition and has shown that the hydroxyl groups are removed when the first half-cycle of precursors are introduced in the chamber, and then replenished after the second half-cycle of precursors during many oxide ALD processes[61-64]. Hydroxyl groups are known to be important for many ALD process, and some studies have found links between hydroxyl concentration and film quality[59,63,65]. One reason for the important role of hydroxyl groups during some ALD processes is the ligand-exchange reaction mechanism that can occur between the precursor and hydroxylated surfaces. Typically, the ligand-exchange process is modeled as:

$$MX_y + |\text{-}OH \rightarrow |\text{-}MX_{y-1} + XH, \qquad (1)$$

where M = inorganic metal, X = ligand, and y = 1, 2, 3…. This mechanism successfully depicts a large number of thin film deposition processes; however, many ALD chemistries are not well modeled as ligand exchange reactions. If the MoF_6 precursor

does not undergo a ligand-exchange process, F may remain on the surface and subsequently at the interface between the substrate and grown film. F at the interface would ultimately impact the properties of the interface and film. Therefore, it is imperative to understand the nucleation mechanics during the initial stages for not only ALD of MoS_2, but also all other chemistries that might not follow the ligand-exchange process presented in Eq 1.

It is not trivial to monitor the ALD process *in-situ*, making it difficult to capture the fundamental phenomena. Density functional theory (DFT) uses first-principles methods to model and infer information that is not easily accessible in experiment. DFT can determine the possible reaction coordinates and transition states by calculating their underlying thermodynamics and energy barriers[66-73]. The precursor orientations, preferred bonding sites, and potential chemistries on a variety of substrates can also be calculated using DFT[74-91]. Our prior work studied the role of hydroxyl groups in the first half-cycle deposition of MoS_2 on three substrates Al_2O_3, HfO_2, and MgO using an MoF_6 precursor[55]. We found that hydroxyl groups facilitated chemical bonds forming between the surface and MoF_6 precursor, and thermodynamically drove the formation of MF_x (M = Al, Hf, and Mg) compounds. In this work, we present a comprehensive study combining computational and experimental work to understand the nucleation process for ALD of MoS_2. We uncover that there are different nucleation mechanisms during ALD of MoS_2. In the first half-cycle of MoF_6, the precursor dissociates onto the surface, and at higher hydroxyl concentrations forms AlF_3. The second half-cycle with H_2S undergoes a ligand-exchange process creating gaseous byproducts. This work highlights how the nucleation mechanisms for ALD of MoS_2 changes throughout the process.

6.2 Methods

6.2.1 DFT Methods

We employed DFT calculations using the Vienna Ab initio Simulation Package (VASP)[92] and Perdew-Burke-Enzerhof (PBE)[93] pseudopotentials with the generalized gradient approximation (GGA) exchange correlation functions. To accurately characterize the system, a cut-off energy of 400 eV was chosen, residual forces were reduced to 0.01 eV/atom, and an energy convergence of $1x10^{-4}$ was achieved. The surfaces were cleaved from a relaxed alumina unit cell, and 2x2x1 supercells were created to increase surface area. A Monkhorst pack 5x5x1 k-point mesh was chosen for the surface supercells, and a vacuum greater than 15 Å was introduced to mitigate spurious interactions. To reduce computational effort, the bottom three layers were frozen using selective dynamics, while the top three layers had no restraints.

The alumina surface supercell in Figure 6.1 serves as a template for creating the morphologies with varying hydroxyl concentrations. In this study, a fully hydroxylated alumina surface has twelve hydroxyl groups, and those random potential positions are denoted with an "X" symbol in Figure 6.1. We investigated the hydroxyl concentration between 0-15.35 OH/nm^2 to understand the effect of surface chemistry on deposition. This hydroxyl concentration range corresponds to 0-12 OH groups per unit cell of the Al_2O_3 surface. For each hydroxyl concentration, three different morphologies were generated, where the positions of the hydroxyl groups were randomized to prevent any local effects. Only one structure was generated for twelve hydroxyl groups, because the surface was fully saturated. A total of thirty-four morphologies were created, and each system underwent a full geometry optimization to account for any surface reconstruction.

After each surface was relaxed, a single MoF_6 or H_2S precursor was then introduced at least 5 Å above each surface, and another geometry optimization was performed. The adsorption energies of the MoF_6 and H_2S above the alumina surfaces were calculated with the following formula:

$$E_{ads} = E_{total\ system} - E_{surface} - E_{precursor} \qquad (2)$$

The Al-O bond lengths were measured when MoF_6 was above the surface. The Bader charge analysis[94] was calculated to understand charge transfer[77,95]. The possible chemical compounds were analyzed.

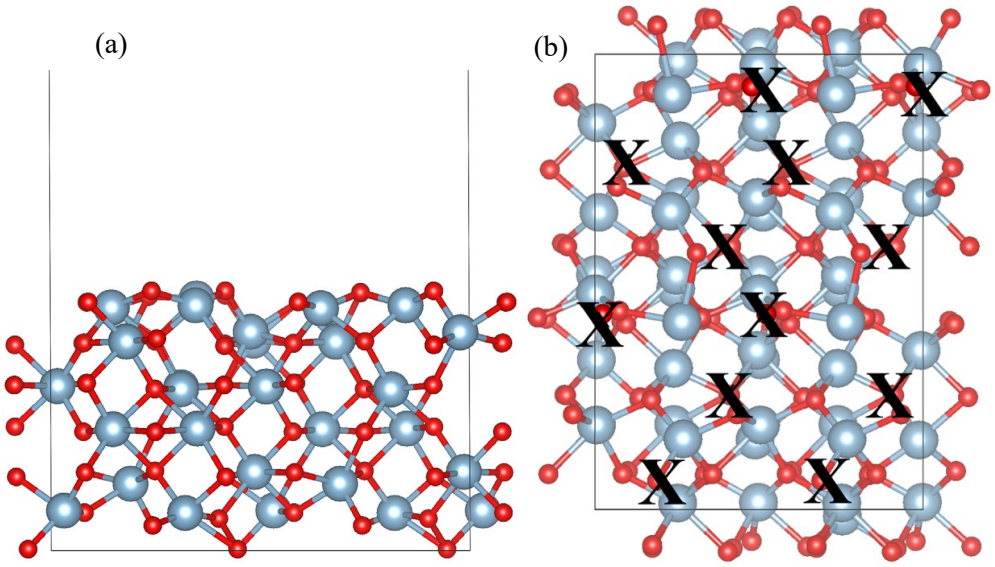

Figure 6.1. Cross section (a) and top town (b) view of the alumina surface supercell where the black "X" denotes one of the twelve possible locations for a hydroxyl group. Red atoms represent O while light blue atoms represent Al. (Color online)

Finally, four MoF_6 precursors were introduced above a hydroxylated alumina surface and the reaction barrier for the H_2S half-cycle was calculated. With the hydroxyl concentration fixed at 6.4 OH/nm^2, our MoF_6 precursors were used to match the mass

gain registered with the quartz crystal microbalance (QCM). After geometry optimization, the charge density difference (ρ_{diff}) was calculated using the following equation:

$$\rho_{diff} = \rho_{total\ system} - \rho_{surface} - \rho_{MoF_6}, \quad (3)$$

where the $\rho_{total\ system}$, $\rho_{surface}$, and ρ_{MoF_6} terms are the charge densities of the total system, surface, and MoF_6 precursors respectively. The ρ_{diff} provides insight into the chemical bonding between the precursors and alumina substrate. After the alumina surface was saturated with MoF_6 precursors, the ρ_{diff} was calculated in the presence of a single H_2S molecule. A geometry optimization was performed, and four reaction pathways were found. The lowest energy barrier suggested the most favorable reaction pathway for the ALD of MoS_2.

6.2.2 Experimental Methods

Experimental studies were conducted in a home-built tube furnace ALD reactor. The system operated under free flow with a constant flow of high purity N_2 to keep a steady chamber pressure at ~1.13 Torr. Tube furnace process temperature was held at 200 °C. MoF_6 (Synquest Labratories, Molybdenum Hexafluoride, 99%) and H_2S (Sigma Aldrich, Hydrogen Sulfide, 99.5%) were used as precursors for both experiments. Both precursors were regulated and metered using 200 μm orifices to yield partial pressures of ~0.1 Torr.

Hydrogen sulfide dosing on alumina surfaces was monitored *in situ* using an Inficon ALD quartz crystal microbalance (QCM). RC cut crystals with an alloy coating (Phillip Technologies) were used in the QCM, which was purged with N_2 to prevent deposition on the backside of the crystal during experiments. The backside purge N2 flow

was adjusted to yield a ~10% increase in the system base pressure. Prior to QCM measurements, the reactor temperature was allowed to stabilize for several hours to reduce any frequency drift of the crystal. To ensure stable measurements, Al_2O_3 ALD was performed until an optimal mass gain of 40 ng/cyc was achieved for the trimethylaluminum (TMA Sigma-Aldrich, 97% purity) and H_2O process. Chamber pressure was 1.8 Torr and a 200 ºC temperature was maintained during QCM measurements.

For X-ray photoelectron spectroscopy (XPS) studies, an initial deposition was performed on SiO_2 coupons that were diced into ~1x1 cm. pieces. Prior to deposition, coupons were cleaned in a fuming sulfuric dip, rinsed with nanopure water and then N_2 dried. Roughly 10 nm of alumina was deposited onto SiO_2 coupons with TMA and water. After alumina deposition, a single 60 mTorr MoF_6 dose was introduced for surface chemical modification investigation. The system then purged with N_2 before the temperature was ramped down to 30 °C for the sample to cool. A transfer bag filled with N_2 was used to carry the coupon to the XPS to reduce contamination and excessive exposure to atmosphere. XPS measurements were performed with a Physical Electronics ESCA 5600 using an Al k_α excitation source. Low resolution survey scans of the surface were performed initially. Next, high resolution scans of the Mo 3d, Al 2p, F1s, and C1s were obtained for chemical analysis and bonding information. Data was analyzed with MultiPack 5.1 software, and all spectra were referenced to the C 1s peak (284.8 eV) of adventitious carbon. Peak fitting on the high-resolution spectra utilized a Gaussian-Lorentzian fit with a Sherly background.

Byproducts from the reaction of MoF_6 with hydroxylated alumina surfaces were measured with an ExTorr XT200 residual gas analyzer (RGA). The RGA was connected downstream of ALD process tube during sampling to ensure detection of all appropriate byproducts. Mass/charge ratios of 18, 20, and 38 amu were monitored and assigned to water, HF and F_2, respectively. RGA was controlled by ExTorr Vacuum Plus 1.0.40 software. Prior to RGA measurements, the ALD tube furnace was coated with ~10 nm of alumina with a final H_2O pulse to form the hydroxylated surface of interest. RGA scans were performed during dosing and purging of MoF_6 and H_2S. MoF_6 and H_2S exposure times were both 1.5 s each followed by 15 s purges.

6.3 Results

6.3.1 Comparing between MoF_6 and H_2S adsorptions

During the ALD of MoS_2 with MoF_6 and H_2S, MoF_6 is typically the first precursor introduced into the chamber, but processes could begin with H_2S. We combined DFT calculations and experimental measurement to assess the interactions of the precursors with hydroxylated Al_2O_3 surfaces. In the DFT calculations, we introduced a single MoF_6 molecule or a single H_2S molecule above alumina surfaces at varying hydroxyl concentrations. We then calculated the average adsorption energies of MoF_6 and H_2S using Equation (2), which are plotted in Figure 6.2 (a). A positive adsorption energy indicates a lack of chemical bonding, suggesting that the precursor will not bond to the surface, while a negative adsorption energy indicates chemical bonding, i.e., chemisorption. The adsorption energy for H_2S is positive at all hydroxyl concentrations, thus confirming that H_2S is not reactive with a hydroxylated alumina surface. Conversely, the adsorption energy for MoF_6 above the alumina surface is negative at all hydroxyl

concentrations, indicating that MoF_6 chemisorbs to the alumina surface. In Figure 6.2 (b), three 1.5 second doses of H_2S were introduced after a hydroxylated alumina surface had been deposited. There was a 15 second purge step in between each dose to allow for QCM frequency response. QCM revealed no net mass gain after the subsequent precursor exposures. The experimental results validate the DFT prediction, showing no reaction between hydroxylated alumina and H_2S.

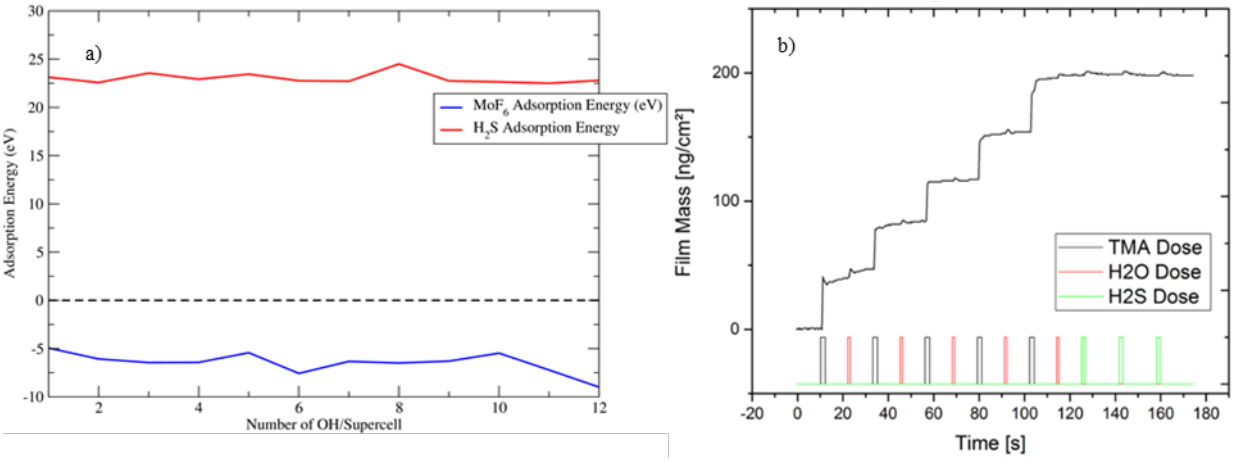

Figure 6.2 Calculated adsorption energies (a) for MoF_6 and H_2S above hydroxylated alumina. A positive adsorption energy indicates a lack of chemical bonding, while a negative adsorption energy indicates strong bonds. DFT calculates show that H_2S does not readily bond to a hydroxylated alumina substrate. To verify the DFT predictions the corresponding mass gain (b) from QCM at 200 ºC is provided for only the H_2S precursor. No net mass gain was recorded indicating a lack of H_2S deposition on an alumina substrate.

6.3.2 Surface Morphology

ALD is a chemically sensitive process, therefore it is imperative to understand if surface morphology can control deposition. So far, the majority of DFT studies[74-91] on ALD have focused on thermodynamic barriers and potential reaction pathways. However, the intricacies of the surface-precursor mechanisms remain unknown. To fill this knowledge gap, the hydroxyl concentration on alumina supercell surfaces was varied to investigate the role of surface chemistry and morphology on ALD nucleation reactions.

The measured bond lengths between the Al-O atoms of the alumina substrate provide insight into the surface morphology. Changes in bond lengths and electron charge localization could also reveal the relationship between surface chemistry and ALD.

In our study, the bond length between Al and O atoms were measured in three different fashions to fully address the role of hydroxyl groups before and after the MoF_6 precursor was introduced. Figure 6.3 is a cross section of an alumina surface, including three regions. For a consistent analysis, a central Al atom was chosen as a reference atom and the distance to its neighboring O atoms was measured. The surface, intermediate, and bulk Al atoms are labeled with a “1”, “2”, and “3” respectively. A configuration for each type of Al atom bonding to O atoms is also shown. The average Al-O bond lengths for the three regions are measured for all 34 hydroxyl morphologies and tabulated in Tables 1 and 2.

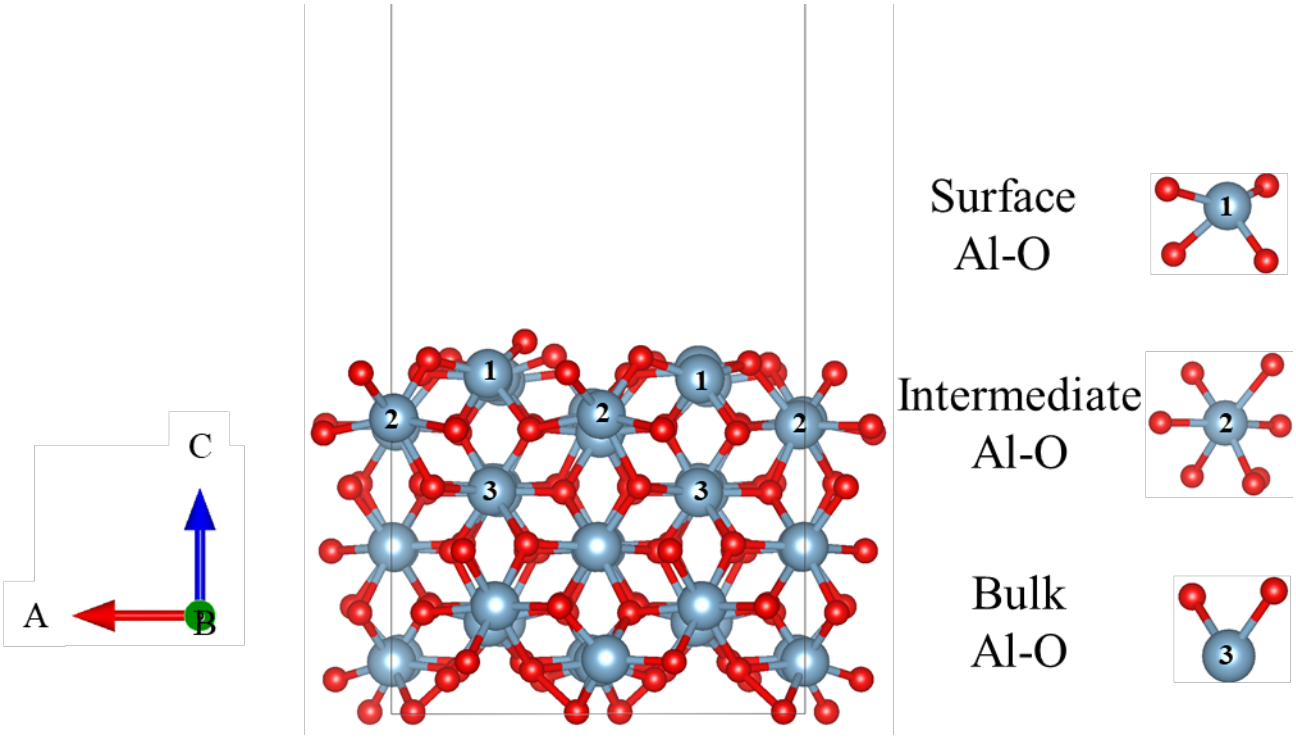

Figure 6.3. Cross section of the alumina surface where the red atoms are O and the light blue atoms are Al. The numbers "1", "2", and "3" correspond to different sections of the surface, including the surface, intermediate, and bulk regions, respectively. Examples of the number of bond lengths measured in each region are also provided.

The bond lengths between all three regions varied as a function of hydroxyl concentration before and after the MoF_6 precursor was introduced, as shown in Table 6.1. The Al-O bond lengths are separated into two categories, Al-OH and Al-O. If an Al-O bond is terminated with a hydroxyl group, it is denoted as Al-OH. The average Al-O bond length was calculated by including both Al-OH and Al-O bonds. Without the MoF_6 precursor, the average surface Al-O bond lengths increased as a function of hydroxyl concentration from 1.80 Å (~10% shorter than the bulk Al-O bond length) to 2.19 Å at 12.79 OH/nm^2, and then dropped to 2.07 Å at 15.35 OH/nm^2. A similar trend was observed after introducing the MoF_6 precursor as the average surface Al-O bond length increased from 1.82 Å to 2.29 Å at 14.07 OH/nm^2, followed by a decrease to 2.07 Å

when fully saturated. Without and with the presence of the MoF_6 precursor, hydroxyl groups stretched the bonds at the surface, resulting in the longer bond lengths. The average Al-O bond increased as a function of hydroxyl concentration, suggesting the sensitivity of the surface chemistry. We also compared the lengths of the Al-OH and Al-O bonds. Before adding the precursor, the Al-OH bond length spiked from 1.80 Å to 2.51 Å at 3.84 OH/nm^2, and then gradually decreased to 2.03 Å when the surface was fully hydroxylated. When the surface was fully hydroxylated, the Al-OH bonds were slightly shorter than the average Al-O bond lengths. A similar trend was observed after introducing the MoF_6 precursor, where the surface Al-OH bond lengths spiked to 2.47 Å at 2.56 OH/nm^2, dropped to 2.10 Å at 7.68 OH/nm^2, and subsequentially increased again to 2.22 Å at 14.07 OH/nm^2. Before including the MoF_6 molecule, the surface Al-O bonds without hydroxyl groups were shorter than Al-OH bonds until 11.51 OH/nm^2. The difference between Al-OH and Al-O bond lengths could stem from a pseudo steric effect, where a high number of hydroxyls leads to a densely packed surface. As hydroxyl concentration is greater than 11.51 OH/nm^2, surface Al-O bonds without a hydroxyl group become the longest and could be the potential surface sites for deposition. Our computational results indicate that hydroxyls have a localized structural effect, and later sections address how the surface chemistry changes.

Table 6.1. The average Al-O bond lengths for the surface region.

	Before MoF_6 Precursor			After MoF_6 Precursor		
OH Concentration (OH/nm^2)	All Surface Al-O	Surface Al-OH	Surface Al-O No H	All Surface Al-O	Surface Al-OH	Surface Al-O No H
0	1.8	1.8	1.8	1.82	1.82	1.82
1.28	1.83	2.01	1.84	1.85	1.84	1.85
2.56	1.88	2.01	1.89	1.98	2.47	1.96
3.84	2.03	2.51	2.08	2.04	2.44	1.99
5.12	1.97	2.2	1.99	1.96	2.17	1.91
6.4	2.04	2.3	1.97	2.04	2.25	2.00
7.68	2.01	2.11	1.98	2.02	2.1	1.99
8.95	2.05	2.15	2.01	2.1	2.1	2.1
10.23	2.09	2.15	2.06	2.22	2.29	2.18
11.51	2.11	2.06	2.14	2.3	2.31	2.29
12.79	2.19	2.11	2.25	2.25	2.18	2.29
14.07	2.14	2.05	2.2	2.29	2.22	2.35
15.35	2.07	2.03	2.11	2.07	2.02	2.12

The average Al-O bond lengths for the intermediate section before and after introducing the MoF_6 precursor are contained in Table 6.2. Unlike the surface region, without and with the presence of the MoF_6 precursor, the average intermediate Al-O bond length decreased slightly from 1.98 Å without hydroxyl groups to 1.94 Å with a fully saturated surface. Before the MoF_6 precursor, the intermediate Al-O bonds were longer than surface Al-O bonds until 3.84 OH/nm^2, which implies that surface chemistry

sensitivity does not permeate deeply into the substrate or significantly change the bonding structure. This trend was also observed after including the precursor. The bulk Al-O bonds are located in the region approximately 3 Å deep into the surface. Finally, we found that the presence of the hydroxyl groups did not affect the bulk Al-O bond lengths. Our computational results suggest three scenarios: (1) The surface Al-O bond lengths are sensitive to hydroxyl concentration, because their lengths change as a function of hydroxyl concentration. We believe that this behavior is attributed to the dangling surface bonds that are unsatisfied without hydroxyls in the computational model. (2) Surface Al-OH bond lengths become shorter when compared to the Al-O bonds at higher hydroxyl concentrations. We suspect that this could stem from a steric effect or changes in electrostatic forces at the surface. (3) Unlike the surface regions, the intermediate and bulk regions are unchanged due to the stable 6-fold coordination of the Al atoms.

Table 6.2. The bond lengths of the Al-O atoms in the intermediate and bulk regions.

	Before MoF_6 Precursor			After MoF_6 Precursor		
All OH Concentration (OH/nm^2)	All Intermediate Al-O	Intermediate Al-OH	Intermediate Al-O No H	All Intermediate Al-O	Intermediate Al-OH	Intermediate Al-O No H
0	1.98	1.98	1.98	1.98	1.98	1.98
1.28	1.98	1.96	1.98	1.99	2.07	1.99
2.56	1.98	2.01	1.98	1.98	1.98	1.98
3.84	1.99	1.97	1.99	1.98	2.06	1.97
5.12	1.98	2.07	1.99	1.98	2.08	1.97
6.4	1.98	2.06	1.96	1.98	2.14	1.95
7.68	1.96	2.02	1.95	1.96	2.04	1.95
8.95	1.96	2.03	1.94	1.97	2.1	1.94
10.23	1.95	1.99	1.94	1.96	2.05	1.94
11.51	1.95	2.03	1.93	1.97	2.1	1.93
12.79	1.95	2.02	1.93	1.98	2.11	1.93
14.07	1.95	2.01	1.92	1.97	2.07	1.92
15.35	1.94	1.96	1.93	1.94	2	1.92

OH Concentration (OH/nm^2)	All Bulk Al-O	All Bulk Al-O
0	2.02	1.99
1.28	1.99	1.99

2.56	1.99	1.99
3.84	1.98	1.98
5.12	1.97	1.98
6.4	1.97	1.96
7.68	1.96	1.97
8.95	1.95	1.96
10.23	1.96	1.96
11.51	1.96	1.96
12.79	1.95	1.95
14.07	1.94	1.96
15.35	1.96	1.96

6.3.3 Bader Charge Analysis

In order to further analyze the effect of hydroxyl concentration on the surface chemistry, we conducted Bader charge calculations[75, 93]. This method calculates the charge associated with an atom according to its Bader partitioning and with respect to the valence state of that atom. A positive Bader charge represents an atom accepting valence electrons to satisfy its outer orbital shell, while a negative Bader charge indicates an atom donating additional valence electrons from its outer orbital shell. For the Al_2O_3 substrate, the Al and O atoms have valence states of 3^+ and 2^- respectively, implying that Al donates valence electrons while O accepts. Therefore, the Bader charge for Al atoms should be negative. Figure 6.4 illustrates the sum Bader charge for the surface Al atoms as a function of hydroxyl concentration. For the 34 morphologies of interest, there are 8 Al atoms terminated at the surface, where each Al contains dangling bonds (note, the size

of the supercell will change the number of surface Al). The sum Bader charge for the surface Al atoms without hydroxyl groups was -19.4 *e*. As hydroxyl concentration increased, the sum Bader charge of the surface Al atoms increased linearly. With 15.35 OH/nm^2 the sum Bader charge of the surface Al atoms was -14.6 *e*, which demonstrates a change in surface electron density and chemistry.

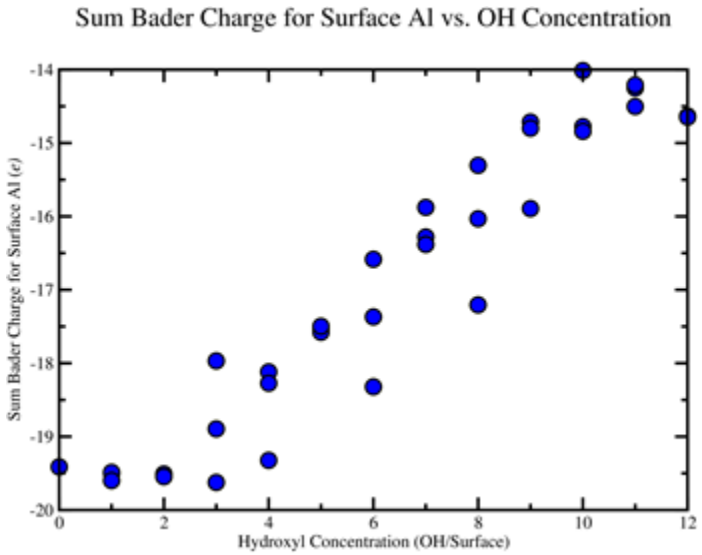

Figure 6.4. The sum Bader charge of the surface Al for all 34 morphologies. At each hydroxyl concentration there are sum Bader charge values, corresponding to each morphology.

As the hydroxyl concentration increased the surface Al atoms became more electropositive, and the bonds with the surrounding O atoms were weakened. This is derived from two factors. The first factor is an increase in the surface Al-O bond lengths. The longer surface Al-O bonds weaken the bond strengths. The second factor appears to be an accumulation of charge at the surface, which stems from the hydroxyls. Apparently, the surface Al atoms prefer to bond with the hydroxyl groups rather than the O atoms at the surface. Charge at the surface becomes more localized around the surface Al atoms

and their respective hydroxyl groups, providing favorable sites for deposition. As a result, the hydroxyl groups weaken surface bonds and facilitates deposition.

6.3.4 Observed Chemical Compounds

The relaxed MoF_6 precursor above the varying hydroxyl concentrations could result in ten different chemical compounds, as listed in Table 6.3. None of our DFT calculations demonstrated the ligand-exchange process or created an HF byproduct, which is not what we expected. Instead, we observed different nucleation mechanisms depending on the hydroxyl concentration. At lower hydroxyl concentrations, the MoF_6 precursor either remained intact, or dissociated into an MoF_4 or MoF_5 compound. The F atom(s) during dissociation left the precursor and adsorbed onto the surface. The dissociated F atom(s) do not break the surface Al-O bonds and were analogous to adatoms. As the number of hydroxyl groups increased, the precursor reacted differently with the alumina surface. The MoF_6 dissociated into a variety of compounds. At these higher hydroxyl concentrations, Al atoms were stripped from the surface and disrupted the Al-O bonds in order to form AlF_x compounds. Above 8.954 OH/nm^2 almost all of the surfaces contained an AlF_x compound.

We interpret the formation of ionic AlF_x compounds as evidence of the hydroxyl groups changing the surface chemistry. The Al-O bonds were weakened at the surface, leaving the surface Al atoms unsatisfied. As the surface Al atoms became electropositive, ionic bonds formed with the electronegative F atoms of the MoF_6 precursor. The unsatisfied surface Al atoms helped separate the F atoms from the MoF_6 precursor to form AlF_x compounds. We did find the formation of AlF_3 at 2.56 OH/nm^2, but we attribute this to a localized hydroxyl effect. At 15.35 OH/nm^2 there were no AlF_3

compounds, and this could indicate a maximum hydroxyl concentration that hinders deposition. This mechanism of forming highly ionic species on the surface appears to thermodynamically drive the ALD process for MoF_6 rather than the expected ligand-exchange process. During the first half-cycle of MoF_6, dissociation appears to be the nucleation mechanism, and the surface hydroxyl concentration will dictate how the precursor dissociates. These DFT insights are further supported by RGA and XPS measurements, discussed in the next section.

Table 6.3. Observed chemical compounds as the hydroxyl concentration increases.

OH Concentration	Observed Chemical Compounds		
(OH/nm^2)	Morphology 1	Morphology 2	Morphology 3
1.28	MoF_6	MoF_6	MoF_5
2.56	$MoF_6 + AlF_3$	MoF_6	MoF_5
3.84	MoF_5	MoF_4	MoF_6
5.12	MoF_4	MoF_5	MoF_6
6.40	MoF_6	MoF_6	$MoF_6 + AlF$
7.68	MoF_3	$MoF_4 + AlF_2$	MoF_4
8.95	MoF_5	MoF_6	$MoF_5 + AlF$
10.23	$MoF_5 + AlF_3$	$MoF_4 + AlF_2$	$MoF_5 + AlF$
11.51	$MoF_5 + AlF$	MoF_6	$MoF_4 + AlF$
12.79	$MoF_5 + AlF_3$	$MoF_6 + Al$	$MoF_4 + AlF_2$
14.07	$MoF_4 + AlF$	MoF_5	MoF_4
15.35	MoF_4	MoF_4	MoF_4

6.3.5 Experimental characterization of MoF_6 exposure on alumina

DFT calculations predict that hydroxyl groups on an alumina surface play an important role during the first half-cycle of MoF_6. Before introducing the precursor, the surface bond lengths change as a function of hydroxyl concentration. After introducing the MoF_6, the precursor undergoes a dissociation process where the compounds formed are dependent on the hydroxyl concentration. To validate that MoF_6 does not undergo a ligand-exchange process, RGA was performed to capture any potential byproducts during three MoF_6 and H_2S cycles.

RGA intensities after three MoF_6 and H_2S cycles give insight to the initial reactions with the alumina surface. Figure 6.5 shows the RGA data for the H_2O, F_2, and HF byproduct species with black and red tick marks representing the MoF_6 and H_2S pulses respectively. Following the initial pulse of MoF_6, as marked in the plot, a small H_2O signal was observed, but negligible HF or F_2. The H_2O signature suggests that surface OH groups undergo chemical rearrangement, breaking hydroxyl- aluminum bonds, and influencing the MoF_6 bonding to the alumina surface. The overall lack of byproducts, specifically HF, supports the DFT calculations that during the first half-cycle, MoF_6 dissociates rather than following a ligand-exchange mechanism. It should be observed that primary byproducts are not observed until the H_2S precursor is introduced to the system. The increases in the partial pressures of H_2O, HF, and F_2 are clearly observed during the second half-cycle of the reaction. Thus, the H_2S precursor experiences a ligand exchange mechanism and creates H_2O and HF byproducts.

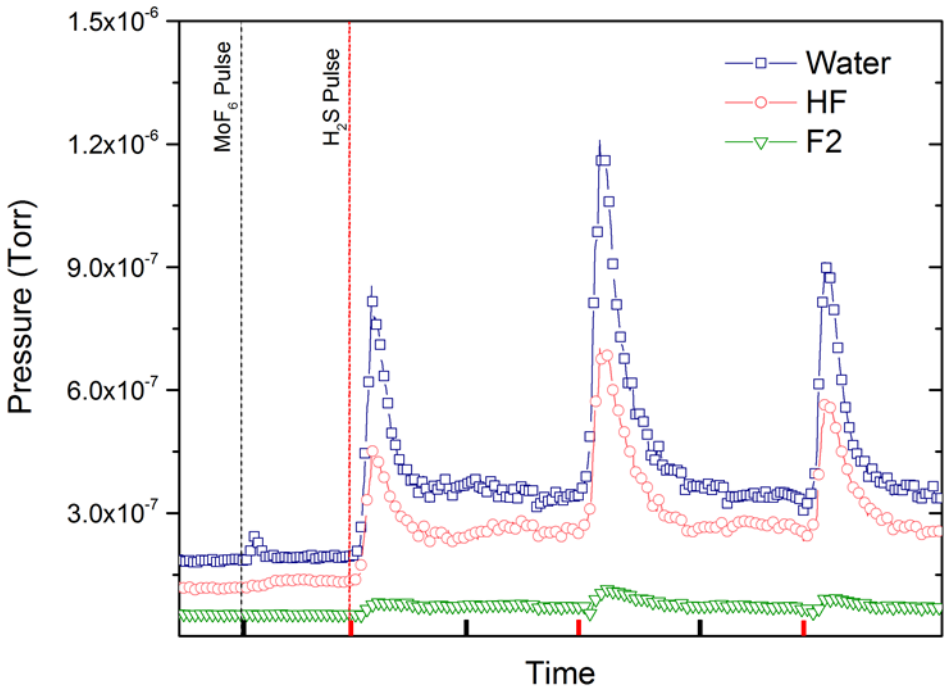

Figure 6.5. Residual gas analysis of first three ALD cycles of MoS_2 grown on Al_2O_3 at 200 °C. There are no significant byproducts created during the first half-cycle of MoF_6, while the second half-cycle of H_2S creates water and HF byproducts. The results are consistent with DFT calculations.

RGA confirmed the DFT predictions that the first half-cycle of MoF_6 does not undergo a ligand-exchange process and no significant gaseous byproducts are created. The next step is to confirm the DFT predictions that AlF_3 forms during MoF_6 dissociation. XPS analysis taken on both a control and a MoF_6-exposed Al_2O_3 film revealed a clear change in surface chemistry after the MoF_6 exposure. The low-resolution survey spectra are shown in Figure 6.6. This survey displays the difference in elemental constituents between an alumina control sample in Figure 6.6(a) and the resulting surface spectra after a single MoF_6 pulse in Figure 6.6(b). Both spectra contain C 1s peak, which we attribute to adventitious carbon. As compared with the control, the emergence of the Mo 3p, Mo 3d, as well as F 1s clearly indicate the presence of Mo and F on the surface of the sample. High resolution scans of individual elemental peaks F 1s and Al 2p were

performed for chemical bonding analysis. Figure 6.7(a) shows the Al 2p region. Slight shouldering of the Al 2p peak can be observed, indicating the presence of additional Al chemical bonding. Peak fitting allowed the deconvolution of the Al 2p peak, revealing AlF_3 at 76.3 eV, as shown in green and the expected primary Al_2O_3 peak at 74.7 eV, shown in red. These binding energies are consistent with literature values[96] and support the DFT findings. Lastly, a high-resolution scan of the F 1s peak was also acquired and is shown in Figure 6.7(b). This spectrum shows the primary F 1s peak at 686.5 eV, which has been assigned to an $AlF_{3.3}H_2O$ bond[97]. However, this binding energy is also very close to the F 1s AlF_3 bond at 687.5 eV[98,99]. In either case, the data support Al-F bonding, and the H_2O could either reflect a contribution of the hydroxylated surface or H_2O adsorbed during transfer from the ALD to the XPS. Lastly, there is a secondary peak at 684.02 eV, which could be due to Mo-F bonding in MoF_x species.

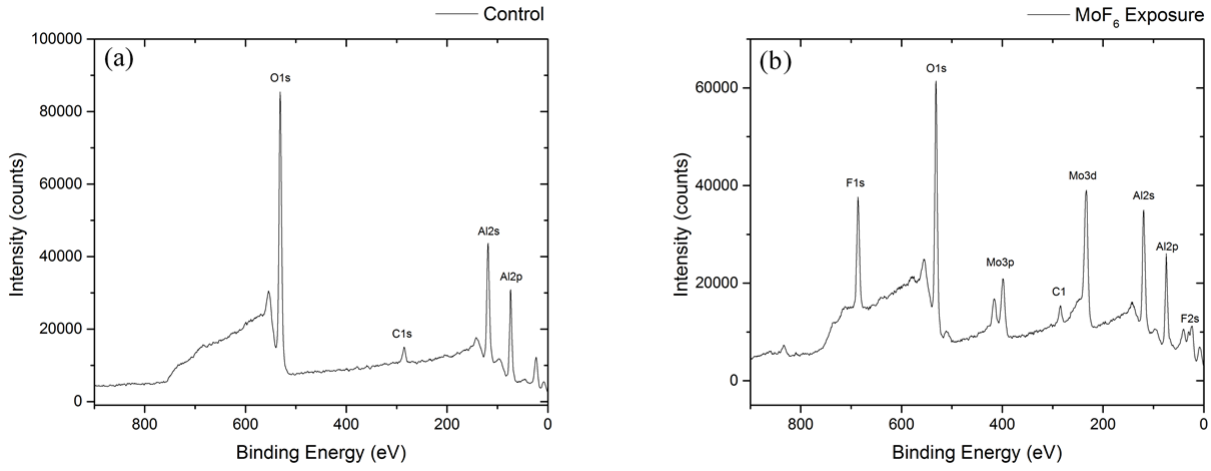

Figure 6.6. Low resolution XPS scan for (a) control Al_2O_3 sample and (b) MoF_6 exposed sample.

Experimental analysis using both XPS and RGA support the DFT predictions that the first half-cycle of MoF_6 undergoes a dissociation process. RGA data show that there

is little to no gaseous byproduct formation during the first half-cycle of the ALD process. Coupled with the Bader charge analysis, it is proposed that the MoF_6 dissociates onto the surface without creating volatile byproducts. XPS supports this claim by showing both Mo and F species remaining on the surface after MoF_6 interaction. Lastly, XPS results are consistent with the observed DFT chemical compounds by showing the formation of AlF_3 after an alumina surface is exposed to MoF_6. These results imply that the OH concentration is larger than the 2.5 OH/nm^2 limit for Al-F formation, but below the upper limit of 15.35 OH/nm^2. Future work will examine how to control the hydroxyl concentration in an ALD chamber.

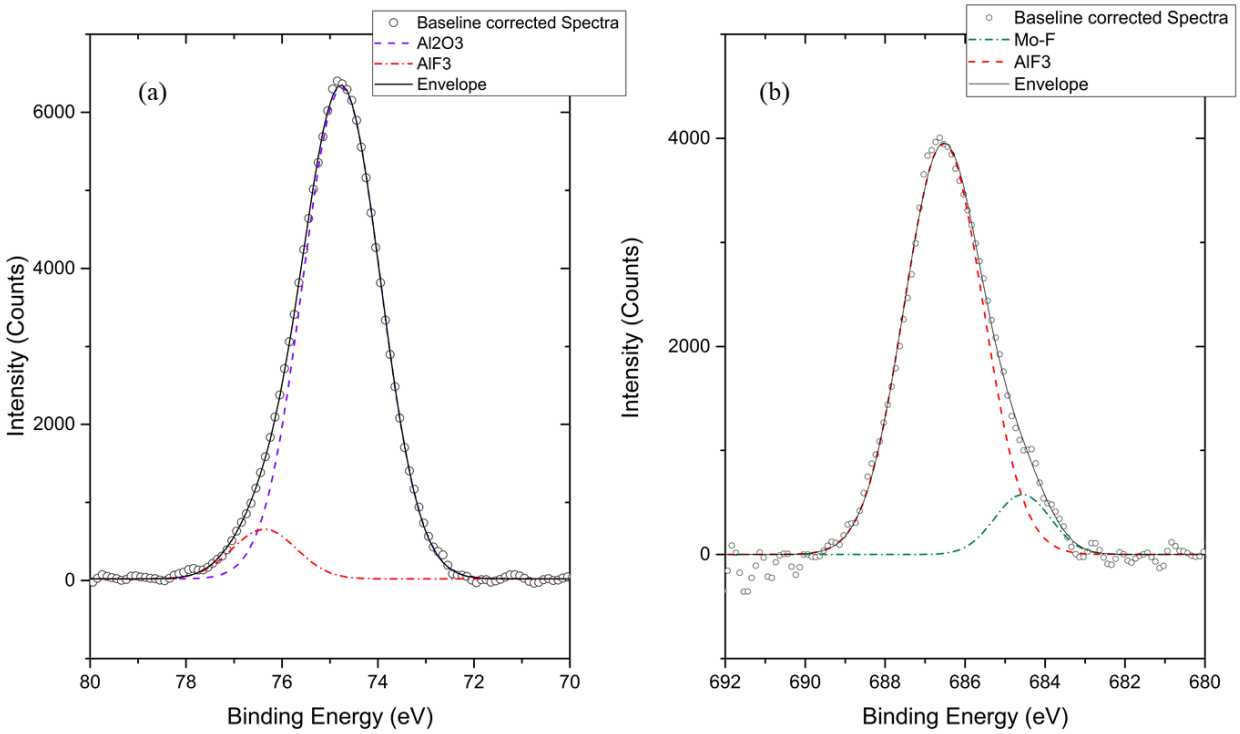

Figure 6.7. High resolution XPS scan of (a) Al 2p and (b) F 1s peak of MoF_6 exposed sample.

6.3.6 DFT on fully saturated MoF_6 and H_2S

DFT calculations and experimental measurements both indicate the presence of ionic Al-F bonds and the lack of gaseous byproducts during the first half-cycle of MoF_6. Figure 6.8(a) illustrates how the four MoF_6 molecules saturate the surface and form a variety of bonds, including several AlF_x compounds and one Mo-O bond. Again, DFT calculations do not support the ligand-exchange mechanism, and the precursors dissociate onto the surface. The charge density difference is shown in Figure 6.8(b) where blue and yellow isosurfaces indicate a gain or loss of electrons, respectively. The collection of blue isosurface below the four MoF_6 indicate chemical bonding between the precursors and the surface. Al-F and Mo-O bonds form between the precursors and the hydroxylated alumina surface, highlighting the variability during the first half-cycle. Hydroxyl groups remain on the surface and appear to be relatively unreactive with the precursors. In order to understand the initiation of the second half-cycle with H_2S, potential reaction pathways were investigated.

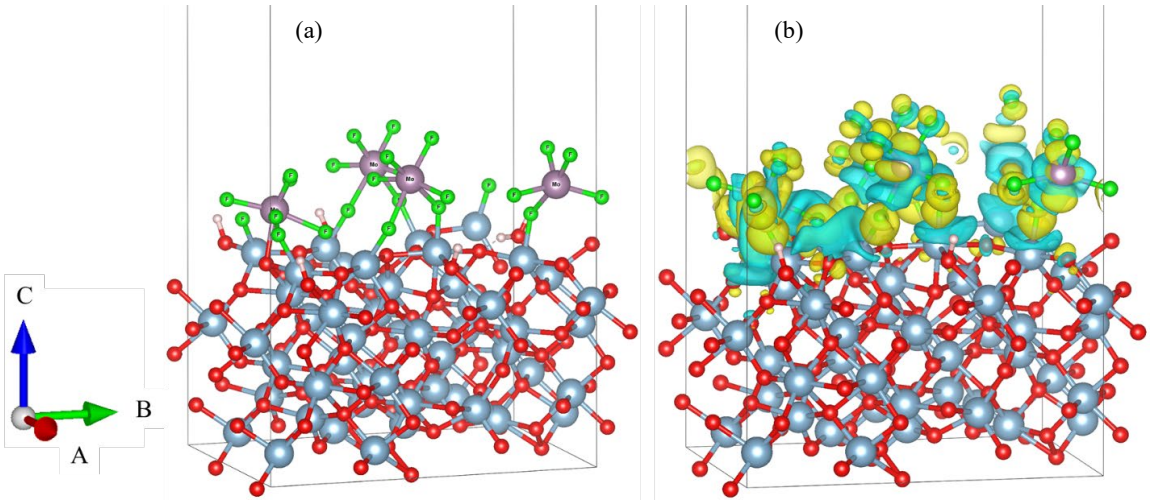

Figure 6.8. Atomic structure (a) of four MoF_6 precursors above an alumina surface with five hydroxyl groups in the supercell (6.4 OH/cm^2), and the corresponding charge density difference (b) where blue and yellow isosurfaces indicate a gain and loss of electrons respectively.

So far, *in-situ* experimental characterization of how S from the H_2S precursor bonds to the film has been limited. Experimental work suggests that H_2S undergoes a ligand exchange process unlike the MoF_6. To gain computational insights into the second half-cycle for ALD of MoS_2, DFT calculations were used to determine the reaction barriers for ligand-exchange processes for H_2S with the MoF_x/AlF_x surface. Although there are numerous potential reaction pathways, this work first compares the reaction barriers for two gaseous byproducts: HF and H_2O, which were both observed in RGA experiments. We aim to understand which byproduct is most likely to form first. The following reactions are modelled using DFT:

$$MoF_6 + H_2S \rightarrow HF + SH + MoF_5 \rightarrow HF + MoSHF_5 \qquad (2)$$

$$MoF_6 + H_2S \rightarrow H_2O + SH + MoF_5 \rightarrow H_2O + HF + MoSF_5 \qquad (3)$$

The byproducts could form when the H_2S precursor approaches the surface and loses one H atom to form an HF from an adsorbed MoF_6 precursor. Conversely, the H_2S could form an H_2O by reacting with a surface hydroxyl. The resulting HS molecule could

then bond to the metal Mo at the top of the precursor or at the precursor/substrate interface. For these reasons four potential reaction pathways were calculated, as shown in Figure 6.9, to understand the formation of a Mo-S bond and its gaseous byproducts. Figure 6.9 also demonstrates the relative locations on the surface where the reactions occur. Figure 6.10 then demonstrates the reaction barriers calculated in this work, which are numbered from smallest to largest reaction barriers.

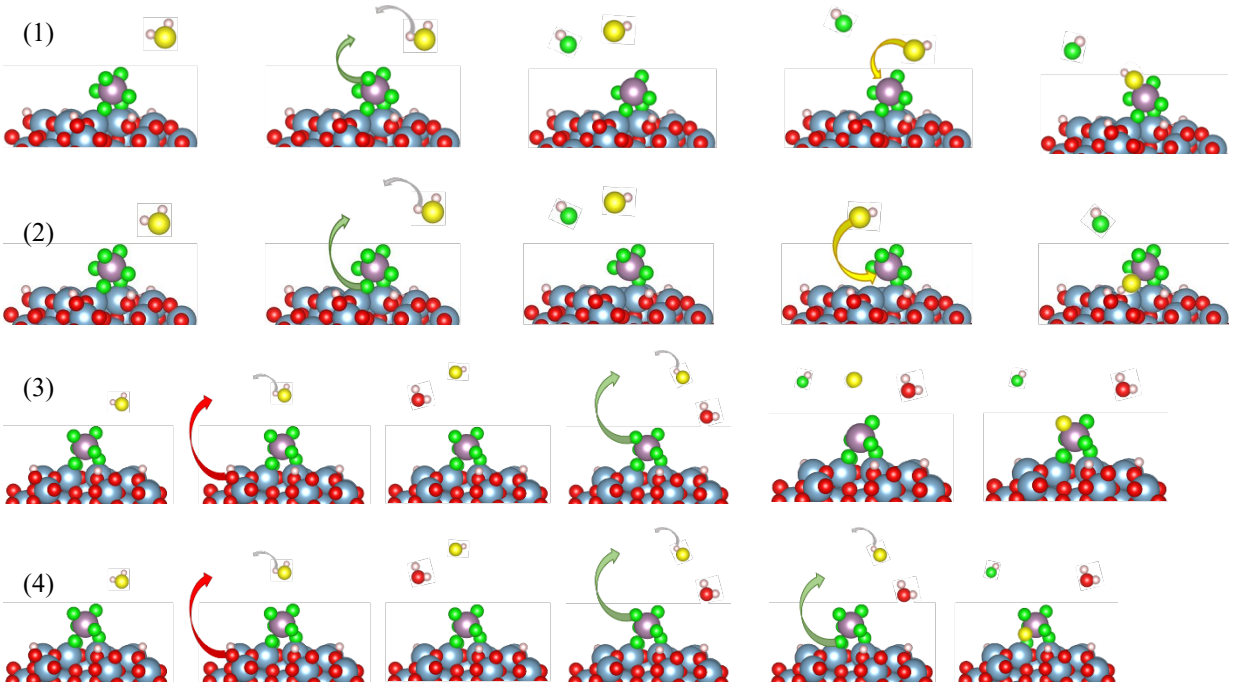

Figure 6.9. Four reactions pathways for the ligand-exchange mechanism for H_2S on MoFx/AlF_x surfaces studied in this work. For clarity, this image does not show the actual orientations and concentration of MoF_6 precursors and should be used as a schematic. Mo(purple), F(green), S(yellow), H(white), O(red), and Al(teal) atoms.

First, we examined the reaction barriers for forming HF as a byproduct. The F could come from several portions of the MoF_6 precursor, but we investigated F from the "top" of the precursor (1) and at the interface between the precursor and the alumina substrate (2). The energy barriers to first create an HF byproduct was 0.65 eV (1) and 1.65 eV (2), however, where the F dissociated from the MoF_6 played an important role.

When the F atom is pinned between the precursor and the surface the energy barrier increased to 1.65 eV. This barrier is larger when compared to the barrier of dissociating the F atom from the "top" of the precursor in pathway (1). The larger dissociation energy is expected due to the strong ionic Al-F bonds we identified in previous sections. The next step in the reaction was forming the Mo-S bond from the ensuing SH species. For both pathways (1) and (2) there is a negative energy for forming the Mo-S bond, which indicated a thermodynamically driven process. Interestingly, the location of the Mo-S bond did not play a significant role in the thermodynamics of the reaction. The Mo-S bond can form at the "top" of the precursor (1) or at the precursor-substrate interface (2) at relatively similar energies, as seen in Figure 6.10. However, the energy penalty for dissociating an F atom from the precursor-substrate interface to form the HF byproduct is too large. Therefore, our calculations indicated reaction pathway (1) will most likely occur when HF is the first byproduct.

The RGA data also indicated that H_2O is a byproduct, so the next step in the calculations was to determine that energy barriers for pathways (3) and (4) in Figure 6.9. Here, an H_2O molecule formed before the HF byproduct. We wanted to know if the H_2O readily forms first in the reaction. In Figure 6.10, the reaction barrier for forming an H_2O byproduct was 1.46 eV, which is much higher than initially forming an HF byproduct. Furthermore, there was ensuing reaction barrier for forming an HF byproduct. Forming an HF byproduct required more energy depending on the location of the F (0.84 eV and 1.67 eV). Again, when the F is pinned between the dissociated MoF_6 precursor and the surface (4) the energy penalty is larger. The total reaction barrier for forming an H_2O molecule and HF molecule was 2.3 eV for pathway (3) and 3.13 eV for pathway (4).

Finally, forming an Mo-S bond was calculated. There was a negative energy for forming an Mo-S bond which again, indicated a favorable reaction. The reaction barriers calculated in Figure 6.10 are important, because they provide insight into the possible reaction pathways and model the ligand exchange process for H_2S.

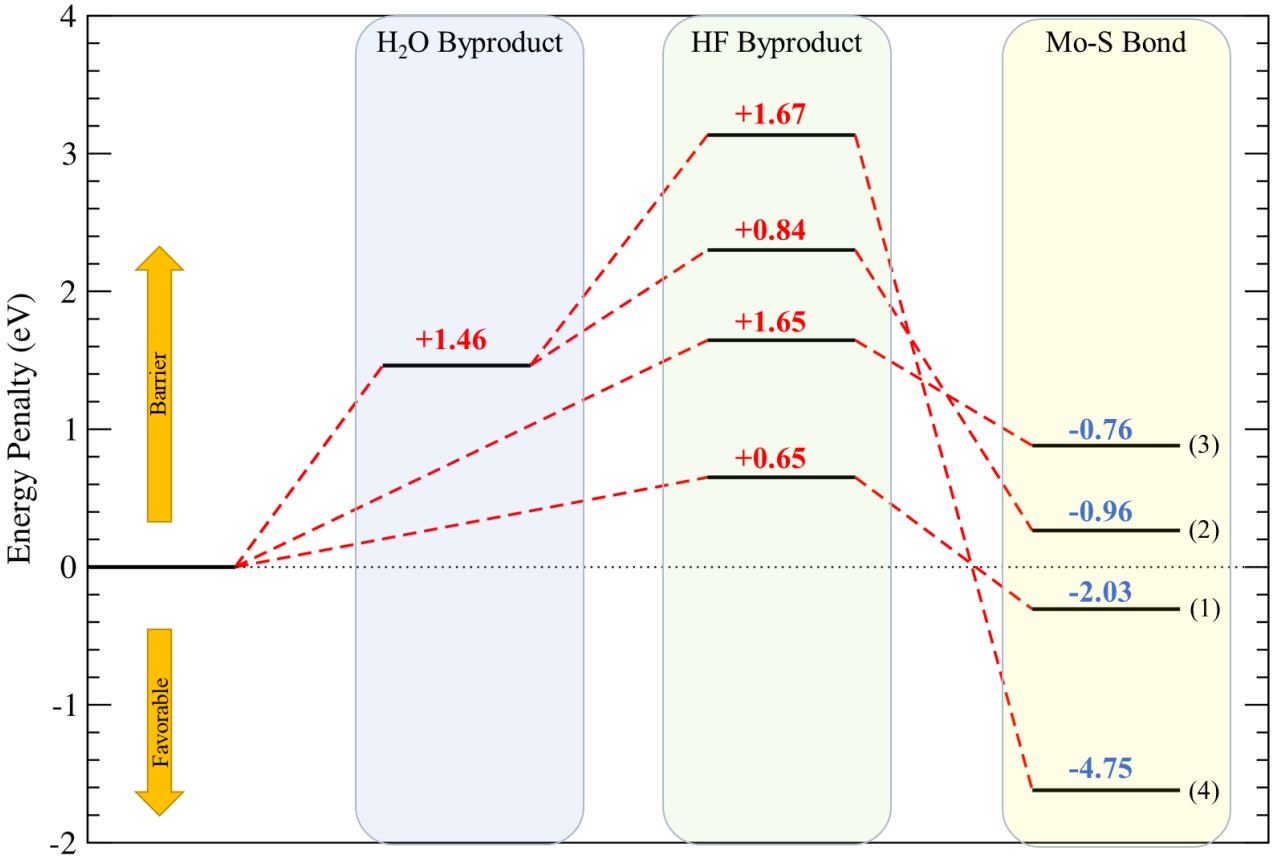

Figure 6.10. Calculated energy barriers for the ligand-exchange mechanism for H_2S. Four potential reaction pathways were calculated, and the formation energies for H_2O and HF byproducts were calculated. DFT calculations suggest the smallest reaction barrier for these four mechanisms is pathway (1).

6.4 Discussion

DFT calculations and experimental measurements indicate that during the first half-cycle, MoF_6 must be introduced first for ALD of MoS_2. Subsequently, during the first half-cycle of MoF_6 precursor, no HF byproducts are formed. The MoF_6 precursor dissociates during the first half-cycle and does not undergo a ligand-exchange

mechanism. The surface hydroxyl concentration can facilitate the formation of ionic AlF_x compounds. During the precursor-substrate interaction, AlF_x compounds are thermodynamically favorable to drive the reaction. Hydroxyl groups may catalyze this process because they perturb the surface chemistry and facilitate the reaction. This result agrees with our previous study[55] that compared a non-hydroxylated and fully hydroxylated surface. Hydroxyls serve an important role during deposition because they appear to alter how the MoF_6 precursor dissociates. RGA confirmed the lack of byproducts during the first half-cycle, and XPS measurements identified Al-F bonds were. The nucleation mechanism for H_2S is different than MoF_6. During the second half-cycle for ALD of MoS_2 the H_2S precursor forms water and HF as byproducts, which is expected in a ligand-exchange mechanism. DFT calculated the reaction barriers for this ligand-exchange mechanism and revealed a small energy penalty to form an HF byproduct. Once the HF byproduct is created forming the Mo-S bond is favorable. This work reveals the first full cycle for ALD of MoS_2 has two distinct nucleation mechanisms. First, a dissociation process for MoF_6, and a ligand-exchange mechanism for H_2S.

6.5 Conclusion

We have applied first-principles methods and experimental measurements to study the role that hydroxyl groups on an alumina surface play during the first half-cycle of MoF_6. The hydroxyl concentration varies from 0 to15.35 OH/nm^2. The surface Al-O bond lengths are sensitive to the varying hydroxyl concentrations without and with the presence of the MoF_6 molecule. However, this behavior is not observed in the intermediate or bulk region of the substrate. The Bader charge analysis reveals that

hydroxyl groups change the surface chemistry by manipulating the surface Al atoms to be more electropositive, resulting in ionic AlF_x compounds on the surface. Experimental RGA confirms the DFT prediction that using MoF_6 as a precursor on alumina substrates undergoes a dissociation process. A high-resolution XPS scan after the first half-cycle of MoF_6 on alumina revealed ionic AlF_x surface species in agreement with DFT findings. This work not only suggests that surface chemistry could be controlled via hydroxyl groups, but also demonstrated different dissociation pathways for MoF_6 depending on hydroxyl concentration. Manipulating the surface chemistry through hydroxyl concentration needs to be further investigated. The ligand-exchange mechanism is observed for the second half-cycle, which highlights the complex chemical reactions that occur during the nucleation of MoS_2.

We believe that this precursor/substrate combination is not the only ALD chemistry that exhibits multiple types of nucleation mechanisms. Inorganic metallic complexes similar to MoF_6 might also undergo a dissociation step during the first half-cycle. The next work should include a detailed investigation during the growth regime for ALD of MoS_2. In this work, it is not initially clear if MoF_6 will shift from a dissociation process to ligand-exchange mechanism. We suspect that during bulk growth of ALD the MoF_6 precursor could form HF byproducts. In conclusion, our work provides additional insight in the ALD of MoS_2 using MoF_6 and H_2S as precursors.

References

1 Bernd Hoefflinger, NANO-CHIPS 2030: On-Chip AI for an Efficient Data-Driven World, 9 (2020).

2 Qing Hua Wang, Kourosh Kalantar-Zadeh, Andras Kis, Jonathan N Coleman, and Michael S Strano, Nature nanotechnology **7** (11), 699 (2012).

[3] Manish Chhowalla, Hyeon Suk Shin, Goki Eda, Lain-Jong Li, Kian Ping Loh, and Hua Zhang, Nature chemistry **5** (4), 263 (2013).

[4] Xiao Zhang, Zhuangchai Lai, Chaoliang Tan, and Hua Zhang, Angewandte Chemie International Edition **55** (31), 8816 (2016).

[5] Min-Rui Gao, Maria KY Chan, and Yugang Sun, Nature communications **6**, 7493 (2015).

[6] Jakob Kibsgaard, Zhebo Chen, Benjamin N Reinecke, and Thomas F Jaramillo, Nature materials **11** (11), 963 (2012).

[7] Junfeng Xie, Hao Zhang, Shuang Li, Ruoxing Wang, Xu Sun, Min Zhou, Jingfang Zhou, Xiong Wen Lou, and Yi Xie, Advanced materials **25** (40), 5807 (2013).

[8] Shengjie Xu, Dian Li, and Peiyi Wu, Advanced Functional Materials **25** (7), 1127 (2015).

[9] Junze Chen, Xue-Jun Wu, Lisha Yin, Bing Li, Xun Hong, Zhanxi Fan, Bo Chen, Can Xue, and Hua Zhang, Angewandte Chemie International Edition **54** (4), 1210 (2015).

[10] Yang Hou, Zhenhai Wen, Shumao Cui, Xiaoru Guo, and Junhong Chen, Advanced materials **25** (43), 6291 (2013).

[11] Anders B Laursen, Søren Kegnæs, Søren Dahl, and Ib Chorkendorff, Energy & Environmental Science **5** (2), 5577 (2012).

[12] Weijia Zhou, Zongyou Yin, Yaping Du, Xiao Huang, Zhiyuan Zeng, Zhanxi Fan, Hong Liu, Jiyang Wang, and Hua Zhang, small **9** (1), 140 (2013).

[13] Kun Chang and Weixiang Chen, ACS nano **5** (6), 4720 (2011).

[14] Shujiang Ding, Jun Song Chen, and Xiong Wen Lou, Chemistry–A European Journal **17** (47), 13142 (2011).

[15] Yun-Xiao Wang, Shu-Lei Chou, David Wexler, Hua-Kun Liu, and Shi-Xue Dou, Chemistry–A European Journal **20** (31), 9607 (2014).

[16] Fei Zhou, Sen Xin, Hai-Wei Liang, Lu-Ting Song, and Shu-Hong Yu, Angewandte Chemie International Edition **53** (43), 11552 (2014).

[17] Liang Cheng, Jingjing Liu, Xing Gu, Hua Gong, Xiaoze Shi, Teng Liu, Chao Wang, Xiaoyong Wang, Gang Liu, and Huaiyong Xing, Advanced materials **26** (12), 1886 (2014).

[18] Stanley S Chou, Bryan Kaehr, Jaemyung Kim, Brian M Foley, Mrinmoy De, Patrick E Hopkins, Jiaxing Huang, C Jeffrey Brinker, and Vinayak P Dravid, Angewandte Chemie International Edition **52** (15), 4160 (2013).

[19] Teng Liu, Chao Wang, Xing Gu, Hua Gong, Liang Cheng, Xiaoze Shi, Liangzhu Feng, Baoquan Sun, and Zhuang Liu, Advanced materials **26** (21), 3433 (2014).

[20] Wenyan Yin, Liang Yan, Jie Yu, Gan Tian, Liangjun Zhou, Xiaopeng Zheng, Xiao Zhang, Yuan Yong, Juan Li, and Zhanjun Gu, ACS nano **8** (7), 6922 (2014).

[21] Jong-Seon Kim, Hae-Wook Yoo, Hyung Ouk Choi, and Hee-Tae Jung, Nano letters **14** (10), 5941 (2014).

[22] F Keith Perkins, Adam L Friedman, Enrique Cobas, PM Campbell, GG Jernigan, and Berend T Jonker, Nano letters **13** (2), 668 (2013).

[23] Yang Tan, Ruiyun He, Chen Cheng, Dong Wang, Yanxue Chen, and Feng Chen, Scientific reports **4**, 7523 (2014).

[24] Zongyou Yin, Hai Li, Hong Li, Lin Jiang, Yumeng Shi, Yinghui Sun, Gang Lu, Qing Zhang, Xiaodong Chen, and Hua Zhang, ACS nano **6** (1), 74 (2011).

[25] Zhiyuan Zeng, Zongyou Yin, Xiao Huang, Hai Li, Qiyuan He, Gang Lu, Freddy Boey, and Hua Zhang, Angewandte Chemie International Edition **50** (47), 11093 (2011).

[26] Changfeng Zhu, Zhiyuan Zeng, Hai Li, Fan Li, Chunhai Fan, and Hua Zhang, Journal of the American Chemical Society **135** (16), 5998 (2013).

[27] Rudren Ganatra and Qing Zhang, ACS nano **8** (5), 4074 (2014).

[28] Xiao Huang, Zhiyuan Zeng, and Hua Zhang, Chemical Society Reviews **42** (5), 1934 (2013).

[29] Kangho Lee, Hye-Young Kim, Mustafa Lotya, Jonathan N Coleman, Gyu-Tae Kim, and Georg S Duesberg, Advanced materials **23** (36), 4178 (2011).

[30] Juqing Liu, Zhiyuan Zeng, Xiehong Cao, Gang Lu, Lian-Hui Wang, Qu-Li Fan, Wei Huang, and Hua Zhang, Small **8** (22), 3517 (2012).

[31] Stanley S Chou, Bryan Kaehr, Jaemyung Kim, Brian M Foley, Mrinmoy De, Patrick E Hopkins, Jiaxing Huang, C Jeffrey Brinker, and Vinayak P Dravid, Angewandte Chemie **125** (15), 4254 (2013).

[32] Goki Eda, Hisato Yamaguchi, Damien Voiry, Takeshi Fujita, Mingwei Chen, and Manish Chhowalla, Nano letters **11** (12), 5111 (2011).

[33] Hai Li, Jumiati Wu, Zongyou Yin, and Hua Zhang, Accounts of chemical research **47** (4), 1067 (2014).

[34] Yi-Hsien Lee, Xin-Quan Zhang, Wenjing Zhang, Mu-Tung Chang, Cheng-Te Lin, Kai-Di Chang, Ya-Chu Yu, Jacob Tse-Wei Wang, Chia-Seng Chang, and Lain-Jong Li, Advanced materials **24** (17), 2320 (2012).

[35] Yu-Chuan Lin, Wenjing Zhang, Jing-Kai Huang, Keng-Ku Liu, Yi-Hsien Lee, Chi-Te Liang, Chih-Wei Chu, and Lain-Jong Li, Nanoscale **4** (20), 6637 (2012).

[36] Xi Ling, Yi-Hsien Lee, Yuxuan Lin, Wenjing Fang, Lili Yu, Mildred S Dresselhaus, and Jing Kong, Nano letters **14** (2), 464 (2014).

[37] Jianping Shi, Donglin Ma, Gao-Feng Han, Yu Zhang, Qingqing Ji, Teng Gao, Jingyu Sun, Xiuju Song, Cong Li, and Yanshuo Zhang, ACS nano **8** (10), 10196 (2014).

[38] Yongjie Zhan, Zheng Liu, Sina Najmaei, Pulickel M Ajayan, and Jun Lou, Small **8** (7), 966 (2012).

[39] Steven M George, Chemical reviews **110** (1), 111 (2009).

[40] TW Scharf, SV Prasad, MT Dugger, PG Kotula, RS Goeke, and RK Grubbs, Acta Materialia **54** (18), 4731 (2006).

[41] TW Scharf, Somuri V Prasad, TM Mayer, RS Goeke, and MT Dugger, Journal of materials research **19** (12), 3443 (2004).

[42] Robert Browning, Prasanna Padigi, Raj Solanki, Douglas J Tweet, Paul Schuele, and David Evans, Materials Research Express **2** (3), 035006 (2015).

[43] Stéphane Cadot, Olivier Renault, Mathieu Frégnaux, Denis Rouchon, Emmanuel Nolot, Kai Szeto, Chloé Thieuleux, Laurent Veyre, Hanako Okuno, and François Martin, Nanoscale **9** (2), 538 (2017).

[44] Thi Anh Ho, Changdeuck Bae, Seonhee Lee, Myungjun Kim, Josep M Montero-Moreno, Jong Hyeok Park, and Hyunjung Shin, Chemistry of Materials **29** (17), 7604 (2017).

[45] Yujin Jang, Seungmin Yeo, Hyungjun Kim, and Soo-Hyun Kim, Applied Surface Science **365**, 160 (2016).

[46] Zhenyu Jin, Seokhee Shin, Do Hyun Kwon, Seung-Joo Han, and Yo-Sep Min, Nanoscale **6** (23), 14453 (2014).

[47] Titel Jurca, Michael J Moody, Alex Henning, Jonathan D Emery, Binghao Wang, Jeffrey M Tan, Tracy L Lohr, Lincoln J Lauhon, and Tobin J Marks, Angewandte Chemie International Edition **56** (18), 4991 (2017).

[48] Steven Letourneau, Matthias J Young, Nicholas M Bedford, Yang Ren, Angel Yanguas-Gil, Anil U Mane, Jeffrey W Elam, and Elton Graugnard, ACS Applied Nano Materials **1** (8), 4028 (2018).

[49] Anil U Mane, Steven Letourneau, David J Mandia, Jian Liu, Joseph A Libera, Yu Lei, Qing Peng, Elton Graugnard, and Jeffrey W Elam, Journal of Vacuum Science & Technology A: Vacuum, Surfaces, and Films **36** (1), 01A125 (2018).

[50] Miika Mattinen, Timo Hatanpää, Tiina Sarnet, Kenichiro Mizohata, Kristoffer Meinander, Peter J King, Leonid Khriachtchev, Jyrki Räisänen, Mikko Ritala, and Markku Leskelä, Advanced Materials Interfaces **4** (18), 1700123 (2017).

[51] Dip K Nandi, Uttam K Sen, Devika Choudhury, Sagar Mitra, and Shaibal K Sarkar, Electrochimica Acta **146**, 706 (2014).

[52] Seokhee Shin, Zhenyu Jin, Do Hyun Kwon, Ranjith Bose, and Yo-Sep Min, Langmuir **31** (3), 1196 (2015).

[53] Lee Kheng Tan, Bo Liu, Jing Hua Teng, Shifeng Guo, Hong Yee Low, and Kian Ping Loh, Nanoscale **6** (18), 10584 (2014).

[54] Arturo Valdivia, Douglas J Tweet, and John F Conley Jr, Journal of Vacuum Science & Technology A: Vacuum, Surfaces, and Films **34** (2), 021515 (2016).

[55] Matthew Lawson, Elton Graugnard, and Lan Li, Applied Surface Science, 148461 (2020).

[56] Qiang Fu, Thomas Wagner, and Manfred Rühle, Surface science **600** (21), 4870 (2006).

[57] Igor Iatsunskyi, Mateusz Kempiński, Mariusz Jancelewicz, Karol Załęski, Stefan Jurga, and Valentyn Smyntyna, Vacuum **113**, 52 (2015).

[58] Ofer Sneh and Steven M George, The Journal of physical chemistry **99** (13), 4639 (1995).

[59] J Van den Brand, WG Sloof, H Terryn, and JHW De Wit, Surface and Interface Analysis: An International Journal devoted to the development and application of techniques for the analysis of surfaces, interfaces and thin films **36** (1), 81 (2004).

[60] Li Zheng, Xinhong Cheng, Duo Cao, Gang Wang, Zhongjian Wang, Dawei Xu, Chao Xia, Lingyan Shen, Yuehui Yu, and Dashen Shen, ACS applied materials & interfaces **6** (10), 7014 (2014).

[61] Anand Deshpande, Ronald Inman, Gregory Jursich, and Christos Takoudis, Microelectronic engineering **83** (3), 547 (2006).

[62] Mark Q Snyder, Svetlana A Trebukhova, Boris Ravdel, M Clayton Wheeler, Joseph DiCarlo, Carl P Tripp, and William J DeSisto, Journal of power sources **165** (1), 379 (2007).

[63] Y Wang, M Dai, M-T Ho, LS Wielunski, and YJ Chabal, Applied physics letters **90** (2), 022906 (2007).

[64] Y Wang, M-T Ho, LV Goncharova, LS Wielunski, S Rivillon-Amy, YJ Chabal, Torgny Gustafsson, N Moumen, and M Boleslawski, Chemistry of materials **19** (13), 3127 (2007).

[65] Riikka L Puurunen, Journal of applied physics **95** (9), 4777 (2004).

[66] Min Dai, Jinhee Kwon, Mathew D. Halls, Roy G. Gordon, and Yves J. Chabal, Langmuir **26** (6), 3911 (2010).

[67] Maxim Deminsky, Andrei Knizhnik, Ivan Belov, Stanislav Umanskii, Elena Rykova, Alexander Bagatur'yants, Boris Potapkin, Matthew Stoker, and Anatoli Korkin, Surface Science **549** (1), 67 (2004).

[68] Gangotri Dey and Simon D Elliott, Theoretical Chemistry Accounts **133** (1), 1416 (2014).

[69] Wonyoung Lee, Neil P. Dasgupta, Orlando Trejo, Jung-Rok Lee, Jaeeun Hwang, Takane Usui, and Fritz B. Prinz, Langmuir **26** (9), 6845 (2010).

[70] Kejing Li, Shenggang Li, Ning Li, David A. Dixon, and Tonya M. Klein, The Journal of Physical Chemistry C **114** (33), 14061 (2010).

[71] Magdalena Siodmiak, Gernot Frenking, and Anatoli Korkin, The Journal of Physical Chemistry A **104** (6), 1186 (2000).

[72] Yuniarto Widjaja and Charles B. Musgrave, Applied Physics Letters **80** (18), 3304 (2002).

[73] Ye Xu and Charles B Musgrave, Surface science **591** (1-3), L280 (2005).

[74] Simon D Elliott, Computational materials science **33** (1-3), 20 (2005).

[75] Simon D Elliott and Henry P Pinto, Journal of electroceramics **13** (1-3), 117 (2004).

[76] S. D. Elliott, G. Scarel, C. Wiemer, M. Fanciulli, and G. Pavia, Chemistry of Materials **18** (16), 3764 (2006).

[77] Liang Huang, Bo Han, Bing Han, Agnes Derecskei-Kovacs, Manchao Xiao, Xinjian Lei, Mark L O'Neill, Ronald M Pearlstein, Haripin Chandra, and Hansong Cheng, Physical Chemistry Chemical Physics **16** (34), 18501 (2014).

[78] Yong-Chan Jeong, Seung-Bin Baek, Dae-Hee Kim, Ji-Su Kim, and Yeong-Cheol Kim, Applied Surface Science **280**, 207 (2013).

[79] Dae-Hee Kim, Seung-Bin Baek, and Yeong-Cheol Kim, Applied Surface Science **258** (1), 225 (2011).

[80] Dae-Hee Kim, Seung-Bin Baek, Hwa-Il Seo, and Yeong-Cheol Kim, Applied Surface Science **257** (15), 6326 (2011).

[81] Kyungtae Lee, Woojin Lee, Hyo Sug Lee, Jaikwang Shin, Jieun Park, Seongsuk Lee, Samjong Choi, Sueryeon Kim, Jinseong Kim, and Youngseon Shim, Physical Chemistry Chemical Physics **18** (42), 29139 (2016).

[82] Atashi B. Mukhopadhyay, Javier Fdez Sanz, and Charles B. Musgrave, Chemistry of Materials **18** (15), 3397 (2006).

[83] Hwanyeol Park, Sungwoo Lee, Ho Jun Kim, Daekwang Woo, Jong Myeong Lee, Euijoon Yoon, and Gun-Do Lee, RSC Advances **8** (68), 39039 (2018).

[84] Aditya Shankar Sandupatla, Konstantinos Alexopoulos, Marie-Françoise Reyniers, and Guy B Marin, The Journal of Physical Chemistry C **119** (32), 18380 (2015).

[85] Aditya Shankar Sandupatla, Konstantinos Alexopoulos, Marie-Françoise Reyniers, and Guy B Marin, The Journal of Physical Chemistry C **119** (23), 13050 (2015).

[86] Mahdi Shirazi and Simon D Elliott, Chemistry of Materials **25** (6), 878 (2013).

[87] Mahdi Shirazi and Simon D Elliott, Nanoscale **7** (14), 6311 (2015).

[88] M Shirazi, WMM Kessels, and AA Bol, APL Materials **6** (11), 111107 (2018).

[89] M Shirazi, WMM Kessels, and AA Bol, Physical Chemistry Chemical Physics **20** (24), 16861 (2018).

[90] D. Elliott Simon, Semiconductor Science and Technology **27** (7), 074008 (2012).

[91] Aleksandra Zydor, Vadim G Kessler, and Simon D Elliott, Physical Chemistry Chemical Physics **14** (22), 7954 (2012).

[92] G Kresse, Phys. Rev. B **54**, 11 (1996).

[93] John P Perdew, Kieron Burke, and Matthias Ernzerhof, Physical review letters **77** (18), 3865 (1996).

[94] W Tang, E Sanville, and G Henkelman, Journal of Physics: Condensed Matter **21** (8), 084204 (2009).

[95] Juan Radilla, Guillermo E Negrón-Silva, Manuel Palomar-Pardavé, Mario Romero-Romo, and Marcelo Galván, Electrochimica Acta **112**, 577 (2013).

[96] G. E. McGuire, G. K. Schweitzer, and Thomas A. Carlson, Inorganic Chemistry **12** (10), 2450 (1973).

[97] V. I. Nefedov, Yu V. Kokunov, Yu A. Buslaev, M. A. Poraj-Koshits, M. P. Gustyakova, and E. G. Il'in, Zhurnal Neorganicheskoj Khimii **18** (4), 931 (1973).

[98] E. Kemnitz, A. Kohne, I. Grohmann, A. Lippitz, and W. E. S. Unger, Journal of Catalysis **159** (2), 270 (1996).

[99] A. Hess, E. Kemnitz, A. Lippitz, W. E. S. Unger, and D. H. Menz, Journal of Catalysis **148** (1), 270 (1994).

CHAPTER SEVEN: SUPPLEMENTARY/SECONDARY WORK

This chapter includes several works I lead or contributed to during my PhD studies. Although most of these studies do not directly relate or contribute to the ALD research, I believe they provide an important illustration on my technical approach on how to leverage DFT. This chapter is structured as follows: Title of the publication, a quick executive summary and broader impact of the work, and finally my personal contributions to the work. Permissions from each journal have been obtained to reproduce any images.

7.1. Porous MnO_2 Octahedral Molecular Sieve OMS-5

First-principles study of carbon capture and storage properties of porous MnO_2 octahedral molecular sieve OMS-5

M. Lawson[a], Jarod Horn[b], Winnie Wong-Ng[b], Laura Espinal[b], Saul H. Lapidus[c], Huong Giang Nguyen[b], Yongtao Meng[d], Steven L. Suib[d], James A. Kaduk[e], and Lan Li[a, f]

[a]*Micron School of Materials Science and Engineering,*

Boise State University, Boise, ID 83706

[b]*Materials Measurement Science Division, National Institute of Standards and Technology, Gaithersburg, MD 20899*

[c]*Department of Chemistry, Illinois Institute of Technology,*

Chicago, IL 60616

[d] *Institute of Materials Science, University of Connecticut,*

Storrs, CT 06269

[e]*Advanced Photon Source, Argonne National Laboratory,*

Argonne, IL 60439

[f]*Center for Advanced Energy Studies,*

Idaho Falls, ID 83401

Reproduced from *Power Diffraction*, **34**, 0885-7156, (2019) with permission of Cambridge University Press.

7.1.1. Executive Summary

Based on the experimentally determined framework structure of porous MnO2 octahedral molecular sieve (OMS)-5, we used density functional theory-based calculations to evaluate the effect of Na^+ cation on pore dimensionality and structural stability, and the interaction between CO_2 and OMS-5. We quantified the formation energy of one CO_2/unit tunnel and two CO_2/unit tunnel and projected the electronic density of states on the OMS-5 framework, CO_2 molecules, and Na^+ cations to reveal their individual contributions and bonding nature. Partial charge densities were also calculated to investigate CO_2 adsorption behavior in the OMS-5. Our studies predict the initial stage and driving force for the adsorption of CO_2 in the OMS-5, guiding the OMS material design for carbon capture and storage applications.

7.1.2. Personal Contributions

DFT was implemented to determine the effect of Na^+ cation concentration on OMS-5. Three scenarios, including without Na^+, low concentrations of Na^+, and high concentrations of Na^+, were studied. The chemical formulas are $Mn_{96}O_{192}$, $Mn_{96}O_{192}Na_4$, and $Mn_{96}O_{192}Na_8$ respectively. We found that incorporating Na^+ could increase the pore size therefore improving the ability for uptake and release CO_2 with a small energy penalty. Formation energies for Na^+ were calculated, and pore dimensions were measured. The lattice dimensions of OMS-5 demonstrate very minor changes in length. The pore volumes decrease slightly by 0.3% and 0.7% with the incorporation of low and high concentrations of Na^+, respectively.

CO_2 molecules were next introduced into the pores of OMS-5 to understand the effect of Na^+ concentration on CO_2 adsorption. Three different CO_2 adsorption

mechanisms were investigated at the three different Na^+ concentrations. First, a single CO_2 molecule was placed in each pore. Second, two CO_2 molecules were placed in each pore in a linear fashion and referred as "Head-to-Head". Third, two CO_2 molecules in each pore were stacked with one another, referred as "Stacking". Figure 7.1 demonstrates the "Head-to-Head" and "Stacking" orientations. The formation energies for CO_2, local density of states (LDoS), and partial charge densities were calculated for all types of CO_2 orientations.

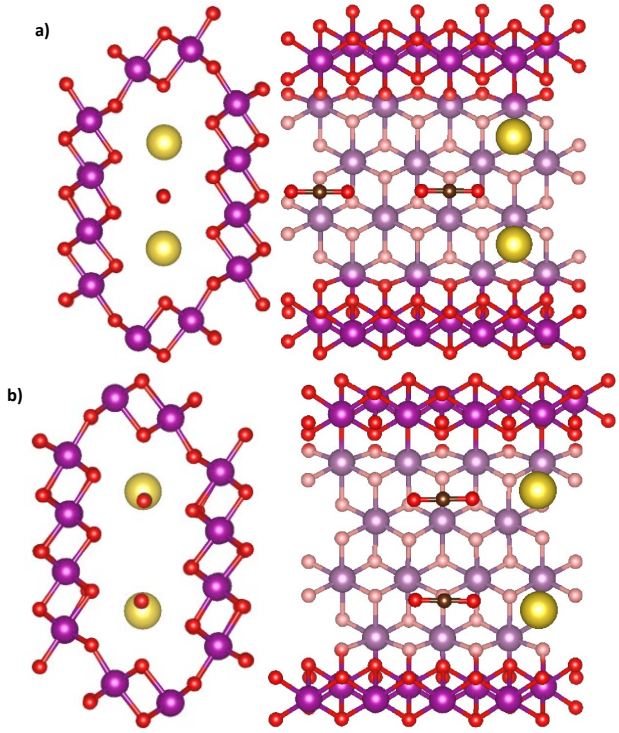

Figure 7.1 Two different CO_2 orientations: (a) head-to-head and (b) stacking in a single OMS-5 pore. Purple, red, yellow, and black spheres represent Mn, O, Na, and C, respectively.

Formation energies for CO_2 are analogous to the strength of the CO_2 bond to the OMS-5 structure and are tabulated in Table 7.1. As the formation energy becomes more negative the strength of the bond increases. The formation energies for all CO_2 orientations are negative at all Na^+ concentrations, indicating that CO_2 adsorption is

energetically favorable. However, the strength of CO_2 adsorption varies across the Na^+ concentrations and CO_2 orientations. Generally, the bond between the CO_2 and OMS-5 framework decreases as the number of CO_2 molecules increases. This implies that OMS-5 can uptake a fixed amount of CO_2 molecules until a "saturation limit" is reached. The low concentration of Na^+ provides the strongest bonds between the CO_2 molecules and OMS-5 framework. The high concentration of Na^+ reduces CO_2 adsorption due to spatial confinement. We also found that the "Head-to-Head" orientation is energetically more favorable than the "Stacking" orientation.

Table 7.1. The calculated formations energies of Na^+ and CO_2 in OMS-5

	Formation Energy of Na^+ (eV/Na^+)
Scenario II: $Mn_{96}O_{192}Na_4$	-2.10
Scenario III: $Mn_{96}O_{192}Na_8$	0.44

	Formation Energy of CO_2 (eV/CO_2)
Scenario II: $Mn_{96}O_{192}Na_4 + 4CO_2$	-1.01
Scenario II: $Mn_{96}O_{192}Na_4 + 8CO_2$ "Head-to-Head"	-1.31
Scenario II: $Mn_{96}O_{192}Na_4 + 8CO_2$ "Stacking"	-1.19
Scenario III: $Mn_{96}O_{192}Na_8 + 4CO_2$	-1.01
Scenario III: $Mn_{96}O_{192}Na_8 + 8CO_2$ "Head-to-Head"	-1.14
Scenario III: $Mn_{96}O_{192}Na_8 + 8CO_2$ "Stacking"	-0.78

Partial charge densities were calculated to demonstrate the electronic interactions between the CO_2 and OMS-5 framework. Figure 7.2 shows that charge densities are localized throughout the OMS-5 framework and at the CO_2 molecules, but not between

the bonds of CO_2 and OMS-5. CO_2 does not chemically bond to OMS-5 and is held in place by weaker van der Waals bonds.

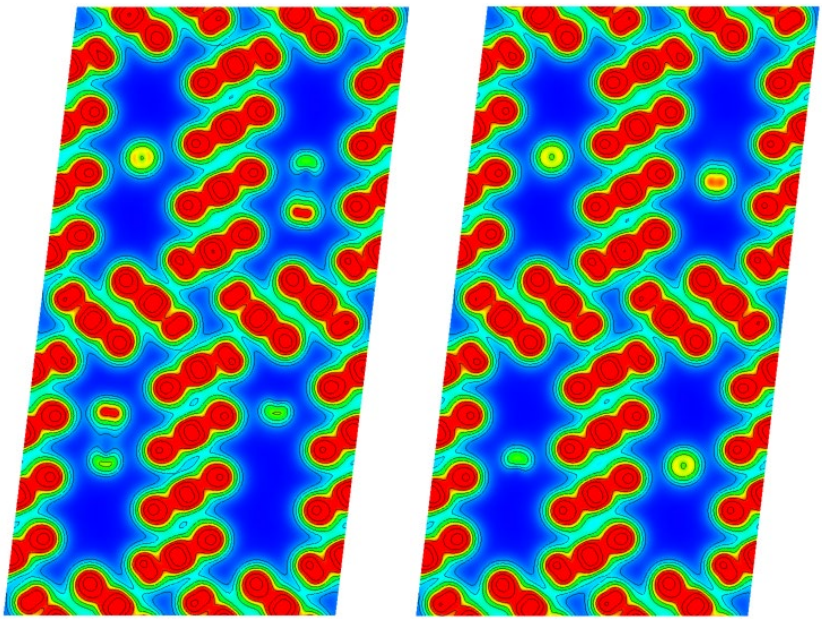

Figure 7.2. The calculated partial charge densities for OMS-5 with two different CO_2 orientations. Red indicates an increased partial charge density while blue indicates a lack partial charge density.

7.2. Metal Organic Framework (MOF) (Ni-4,4'azopyridine)[Ni(CN)4]

Synchotron crystal structure, sorption property, and electronic structure of flexible MOF, (Ni-4,4'azopyridine)[Ni(CN)4]

W. Wong-Ng [a], G. McCandless[b], J. Culp[c,d], M. Lawson[e], Y.S. Chen[f], D. W. Siderius[a], and L. Li[e]

[a]*Materials Measurement Science Division, National Institute of Standards and Technology, MD 20899*

[b]*Chemistry Department, University of Texas at Dallas, Richardson, TX 75080*

[c]*National Energy Technology Laboratory, Department of Energy, P.O. Box 10940, Pittsburgh, PA 15236*

[d]*AECOM, Pittsburgh, PA 15236*

[e]*Materials Science and Engineering Department, Boise State University, Boise, ID 83725*

[f]*ChemMatCARS, University of Chicago, Argonne, IL 60439*

Under review in Solid State Sciences (**2021**) with permission from Elsevier

7.2.1. Executive Summary

We collaborated with NIST on the Ni-based flexible metal organic frameworks (MOF) $(Ni(L)[Ni(CN)_4]_n$ where L = 1,4-Bis(4-pyridyl) benzene), or more simply, Ni-dpbz. Similar to the OMS systems (see section 7.1), Ni-dpbz has an ability to capture CO_2 due to a semiporous network of ligands. Incorporating Ni creates two different types of bonding configurations between the Ni and the organic framework. The 5-fold and 6-fold Ni-N bonds occupy different states in the valence and conduction bands. We found that conduction occurs through the 6-fold Ni-N coordination and this is where CO_2 adsorption is most likely to occur.

7.2.2. Personal Contributions

VASP calculations were implemented to understand the electronic structure for Ni-N bonding configurations. The LDoS in Figure 7.3 was calculated to understand the differences between the 5-fold and 6-fold Ni-N coordination. The blue 5-fold Ni-N coordination occupies states in the valence band. In comparison, the 6-fold Ni-N coordination in red contains states in both the valence and conduction bands. This indicates that electron conduction occurs on the 6-fold Ni-N coordination, due to the lack of states in the conduction band from the 5-fold Ni-N coordination.

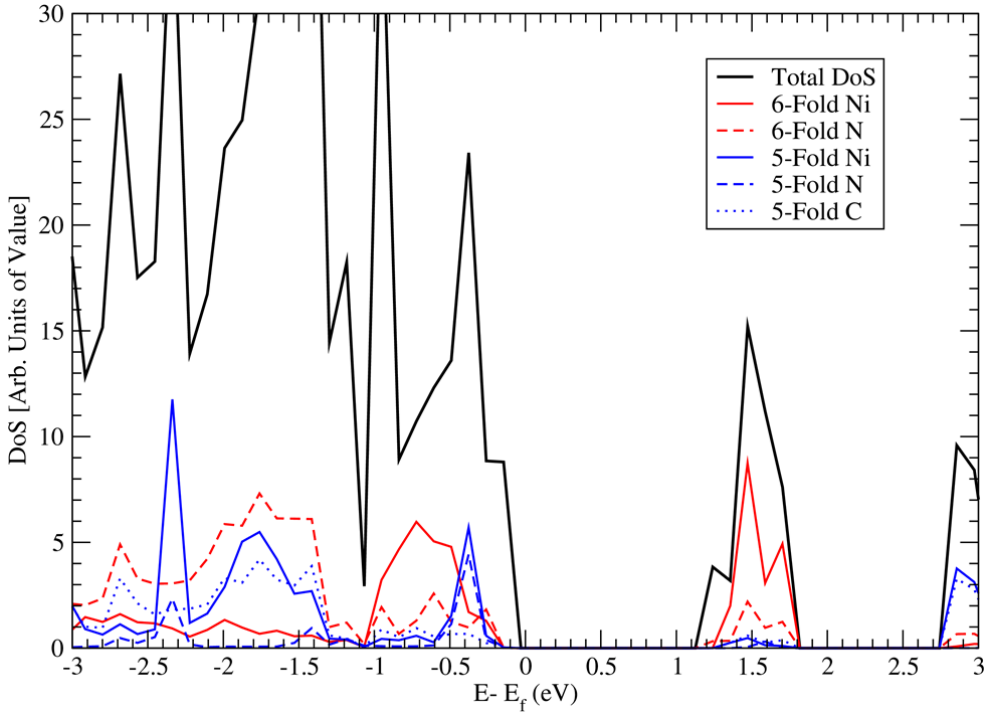

Figure 7.3. The calculated Local Density of States (LDoS) for the 5-fold and 6-fold N-Ni coordination.

7.3. Metal Organic Framework (MOF) $\{[Ni(dpbz)][Ni(CN)_4]\}_n$, dpbz = 1,4-bis(4-pyridyl)benzene

Electronic structure, pore size distribution, and sorption characterization of an unusual MOF, $\{[Ni(dpbz)][Ni(CN)_4]\}_n$, dpbz = 1,4-bis(4-pyridyl)benzene

Winnie Wong-Ng[a], Izaak Williamson[b], Matthew Lawson[b], Daniel W. Siderus[a], Jeffrey T. Culp[c,d], Yu-S. Chen[5], and Lan Li[b]

[a]*Materials Measurement Science Division, National Institute of Standards and Technology,*

Gaithersburg, Maryland 20899, USA

[b]*Department of Materials Science and Engineering, Boise State University,*

Boise, Idaho 83725, USA

[c]*National Energy Technology Laboratory, Department of Energy,*

P.O. Box 10940, Pittsburgh, Pennsylvania 15236, USA

[d]*AECOM, Pittsburgh, Pennsylvania 15236, USA*

[e]*ChemMatCARS, University of Chicago,*

Argonne, Illinois 60439, USA

Reproduced from *Journal of Applied Physics*, **123**, 245105, (2018) with permission of AIP Publishing

7.3.1. Executive Summary

Metal organic frameworks (MOFs) provide a feasible solution to carbon capture and storage due to the pore structure and unique chemical makeup. MOFs offer a precise control of the functionality, pore size, flexibility, and length, leading to a large range of potentially synthesizable materials. $\{[Ni(1,4\text{-bis}(4\text{-pyridyl})benzene)][Ni(CN)_4]\}_n$, or Ni-dpbz, was synthesized for its potential application in carbon capture. The dpbz ligands create two unique Ni sites that result in a 5-fold and 6-fold symmetry. In this work we refer to the 5-fold and 6-fold symmetry as Ni1 and Ni2, respectively. These two different forms of Ni symmetry could play an important role in the capture of CO_2 molecules. Therefore, DFT calculations were conducted to study different bonding characteristics between the 5-fold and 6-fold Ni atoms.

7.3.2. Personal Contributions

VASP was implemented to understand different electronic configurations of the 5-fold and 6-fold Ni. Figure 7.3 contains the calculated partial charge densities for the valence and conduction band edges, respectively, providing information on where electrons/charge would congregate during electron excitement. There are available states at the conduction band edge of Ni1 which is where electron conduction which would take place. The lack of available states on Ni2 suggest a stronger chemical bond forming around Ni2. Further analysis from the LDoS and charge transfer measurements supported this prediction through demonstrating that Ni1 has the stronger ionic bonds than Ni2.

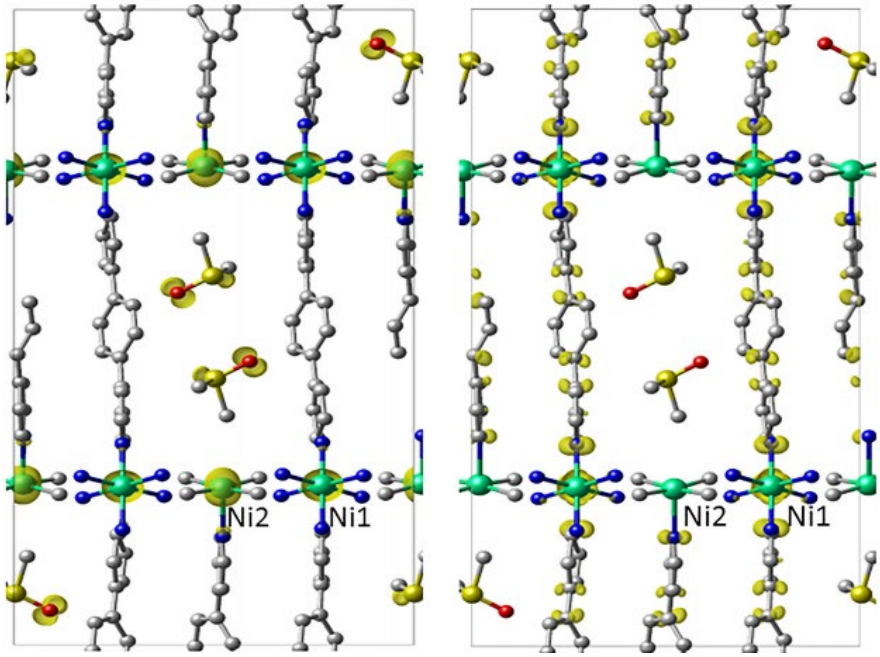

Figure 7.3. The calculated partial charge densities for the valence (a) and conduction (b) band edges of metal organic framework. Green, blue, grey, yellow, and red spheres represent Ni, N, C, S, and O, respectively.

7.4. Dopant Effect on 2D Transition Metal Dichalcogenides (TMDs)

Metal-site dopants in two-dimensional transition metal dichalcogenides

I. Williamson[a], M. Lawson[a], S. Li, Y. Chen[b], and L. Li[a,c]

[e]*Materials Science and Engineering Department, Boise State University, Boise, ID 83725*

[b]*Department of Mechanical Engineering, The University of Honk Kong, Pokfulam Road, Hong Kong SAR, China*

[c]*Center for Advanced Energy Studies, Idaho Falls, ID 83401*

Reproduced from WMED Conference Proceedings, DOI: 10.1109/WMED.2019.8714147 with permission from IEEE (2019).

7.4.1 Executive Summary

As mentioned in this dissertation there is significant interest in using TMDs in semiconducting manufacturing. Specifically, engineers and scientists have examined how to tailor TMD properties through doping. This could achieve desired materials properties at 2D, leading to massive applications. This work examined the effects of metal site dopants on the structural, electrical, and optical properties of 2D MoX_2 and WX_2 (X = S, Se, and Te) films. Six different transition metals (Mo, Ni, Sc, Ti, V, and W) were chosen, and DFT-based energetic, electronic and optical calculations were performed. The structural distortion was measured by calculating the X-X bond lengths and X-M-X bond angles (where X = chalcogen and M = transition metal). The binding energies were subsequently calculated to quantify the stability of the 2D film. The band gaps, formation energies, and phonon interactions were calculated and categorized. We found that using heavier chalcogenides decreases the stability of the films. Additionally, atomic stability is greater when not using Ni as the substitutional dopant.

7.4.2. Personal Contributions

Electronic structure for each metal site-doped TMD was calculated. We found that the larger size of the chalcogenide decreases the band gap. Furthermore, when doped with 2.083% transition metal most films would become metallic, as seen in Figure 7.4, indicating that 2D MoX_2 and WX_2 possess band gaps very sensitive to metallic site substitution. This significant change in electrical band gap plays an important role in the optical properties of the film. The optical conductivities of the films were also calculated. DFT calculations revealed an improvement in the photosensitivity and photoresponsivity of the films, stemming from the metallic behavior of the bandgap. In conclusion, DFT

calculations highlighted the sensitivity of 2D MoX_2 and WX_2 (X = S, Se, and Te) films to metal site dopants.

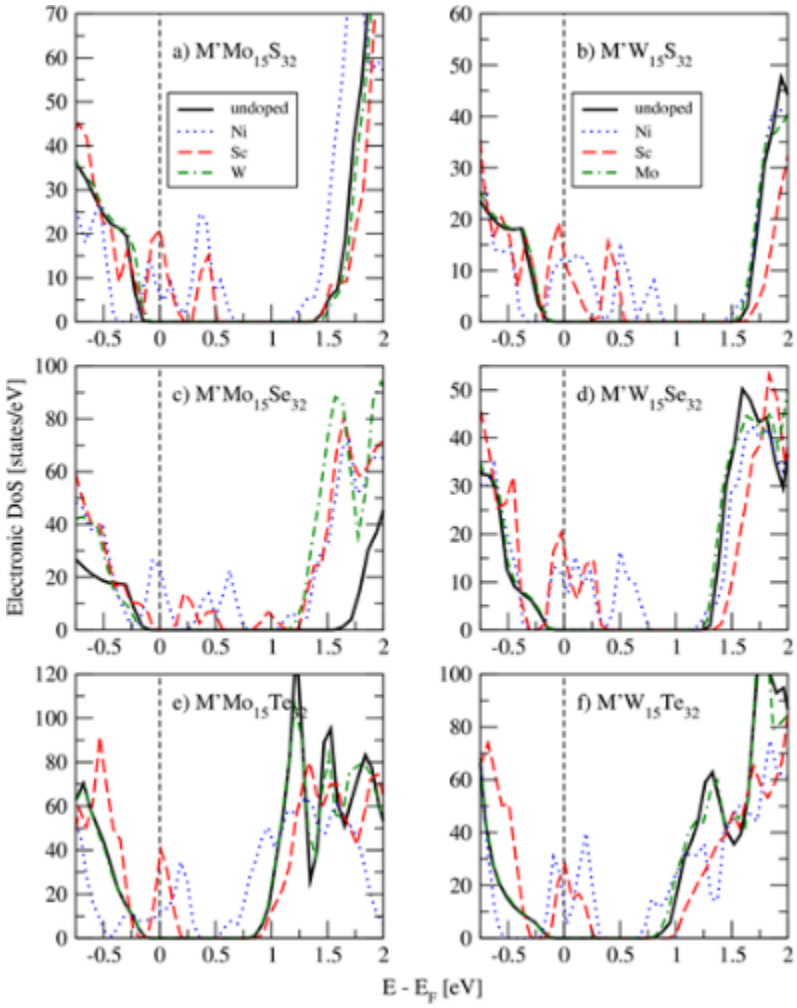

Figure 7.4. Calculated LDoS for doped MoX_2 and WX_2 thin films.

7.5. TiO_2 Nanotubes

Defect generation on TiO_2 nanotube anodes via heat treatment in various atmospheres for lithium-ion battiers

A. Savva[a], K. Smith[a], M. Lawson[a], S. Croft[a], A. Weltner[a], C. Jones[a], H. Bull[a], P. Simmonds[a], L. Li[a] and H. Xiong[a]

[a]*Micron School of Materials Science and Engineering, Boise State University, 1910 University Drive, Boise, ID 83725*

Reproduced in *Physical Chemistry Chemical Physics.*, **20**, (2018), 22537-22546 with permission from Royal Society of Chemistry

7.5.1. Executive Summary

As the global demand for energy continues to rise at impressive rates, substantial work has been done for energy storage. Batteries are rapidly becoming the new forefront for materials science in an effort to keep pace with global energy demands. The electrochemistry that drives batteries is comprised of four parts: the anode, cathode, electrode, and electrolyte. These four components are each separate materials which results in a high amount of design variability. One of those facets are anodes made of titanium dioxide (TiO_2). Lithium-based batteries pose a variety of safety concerns, while TiO_2 is a cheap, abundant, and possesses a comparable energy capacity to that of graphite. Initial work showed that different processing treatments could create point defects that alter the electrical transport properties of TiO_2. TiO_2 anodes were treated in the following atmospheres: O_2, Ar, N_2, and water vapor. These atmospheres could create either Ti or O vacancies. DFT was implemented to calculate how small vacancy concentrations change the electrical properties of TiO_2.

7.5.2. Personal Contributions

The first step in the DFT calculations was to construct atomistic models of the TiO_2 pristine anode, with a O vacancy, and with an Ti vacancy. The crystal lattice was calculated and compared with experimental measurements to validate the DFT models. The bandgap of the pristine anatase TiO_2 was calculated to be 3.2 eV in agreement with literature. Bandgaps of the O and Ti vacancies were subsequently calculated to understand the effect of the point defects. The presence of an O vacancy shifts the conduction band and creates mid gap states, altering electron conduction. This does not occur with the Ti vacancy. The presence of a Ti vacancy shifts the Fermi energy into the

valance band, resulting in *p*-type semiconducting behavior. Partial charge densities were also calculated, as shown in Figure 7.5. The partial charge densities of conduction and valence band edges indicated a change in electron conduction depending on the type of vacancy. O vacancies improve electron conduction in the TiO_2 lattice while Ti vacancies hinder electrical conductivity. TiO_2 anodes were subsequently synthesized and supported our DFT predictions about the improvement of electrical conductivity with O vacancies.

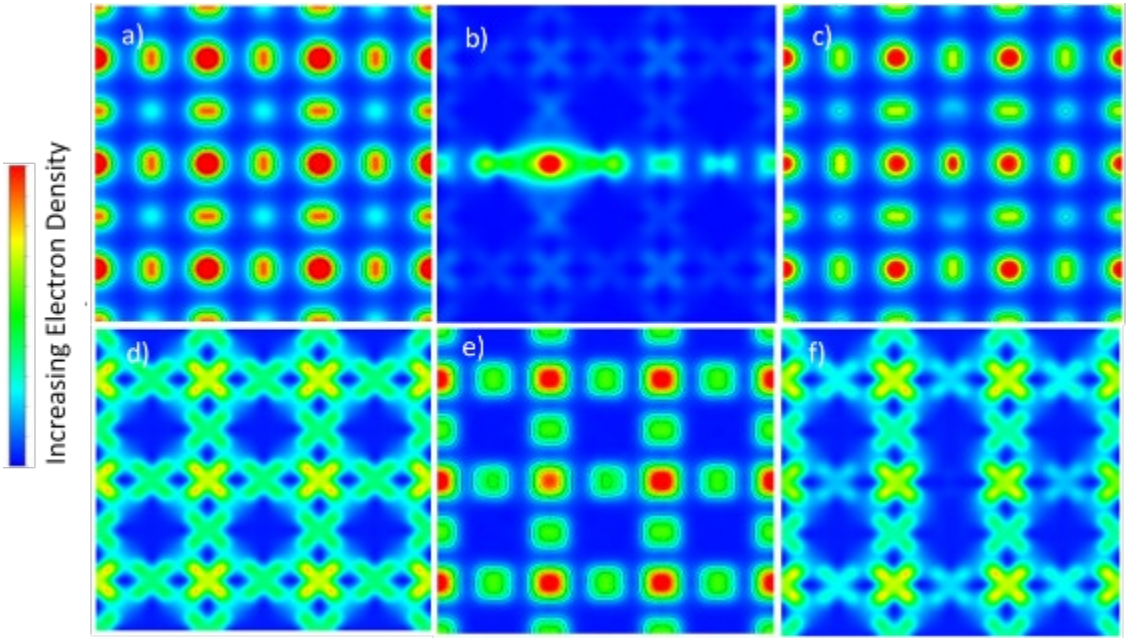

Figure 7.5. Partial charge calculations for (a) and (d) pristine anatase TiO_2, (b) and (e) anatase TiO_2 with O vacancy, (c) and (f) anatase TiO2 with Ti vacancy. Images a-c are the valence band models, d-f are the conduction band models.

7.6. ALD of MoS_2 on Metal Oxides

Nucleation and growth of Molybdenum Disulfide grown by Atomic Layer Deposition on Metal Oxides

J. Soares[a], S. Letourneau[a,b,], M. Lawson[a], A. Mane[b], J. Elam[b], and E. Graugnard[a]

[a]*Micron School of Materials Science and Engineering, Boise State University, 1910 University Drive, Boise, ID 83725*

[b]*Argonne National Laboratory, Energy Systems Division, 9700 S Cass Ave, Lemont, IL 60439, USA*

Will be submitted to the Journal of Vacuum Science and Technology

7.6.1. Executive Summary

Few-layer ALD of MoS_2 using MoF_6 and H_2S precursors was grown on oxide substrates. This work was the first study that demonstrated controllable few-layer growth of MoS_2 using MoF_6 and H_2S using a variety of experimental measurements. The growth mechanisms were subsequently studied to understand how few-layer growth was achievable. The number of ALD cycles was finely tuned to achieve 1, 2, and 3 layer MoS_2 growth. Due to the novel nature of the experiment atomic information was necessary to interpret the deposition process. Potential bonding mechanisms for MoF_6 molecules on an alumina substrate were studied using DFT.

7.6.2. Personal Contributions

Three MoF_6 precursors were introduced above a hydroxylated Al_2O_3 surface, and underwent a full geometry optimization using DFT. The residual charge densities were subsequently calculated, and both the geometry optimization and residual charge density are presented in Figure 7.6. We found that when multiple precursors begin to reach the surface, there is a cascading reaction. The introduction of a third MoF_6 precursor could help create a bridged Mo-O bond for precursor number 2, as shown in Figure 7.6. This prediction agrees well with FTIR data. The residual charge density difference demonstrates a gain or loss of electrons through blue and yellow isosurfaces, respectively. Charge congregates between Al-F surface bonds, as well as between the precursors, indicating that in-plane covalency occurs as the precursor concentration increases.

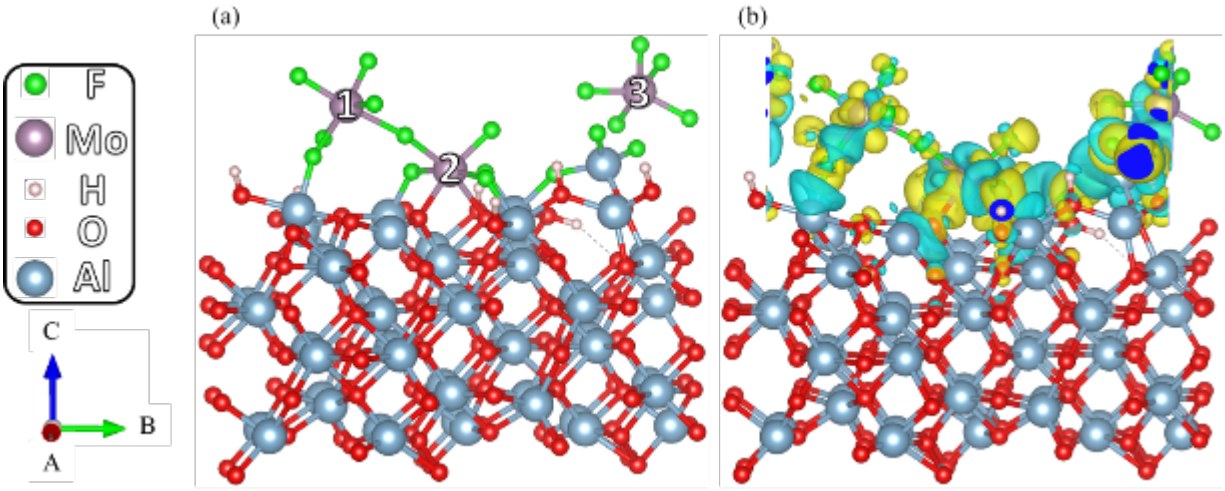

Figure 7.6. Image of (a) the relaxed structure and (b) charge density difference of an alumina surface with three MoF_6 precursors. The MoF_6 precursors are number 1, 2, and 3 to help distinguish how each reacts with the surface. Blue and yellow isosurfaces indicate a gain or loss of electrons, respectively.

CHAPTER EIGHT: CONCLUSION

The research goal of this dissertation is to implement first-principles methods to understand the nucleation of thin films by ALD, which poses a challenge in *in-situ* measurements. Computational efforts address the factors that control nucleation, and emphasize the complexity of ALD. A combination of DFT-based calculations and experimental measurements validate the predictions and provide detailed insight into the nucleation mechanism of ALD. This dissertation validates the hypothesis that surface chemistry and morphology are important factors that can control the nucleation mechanism during the ALD of thin films used in electronic devices. In addition, surface chemistry and morphology can be manipulated by hydroxyl groups, and the MoF_6 and H_2S precursors undergo different nucleation mechanisms during ALD of MoS_2.

Chapter one serves as an introduction to what thin films are and why miniaturization is directly linked the global economy. This chapter identifies several key advantages of ALD for thin films and why ALD is a rapidly growing field. Thus, research such as this dissertation can provide valuable insight into atomic-scale processes that cannot be studied *in-situ*. The four main objectives are outlined and the methodologies for achieving each objective is discussed.

Chapter two examines the up-to-date history of MoS_2, the advantageous properties it possesses, and why reducing the dimensionality is of great research interest. This chapter also examines various methods for depositing 2D-MoS_2, such as exfoliation and CVD, and the drawbacks of those methods. Thus, ALD is a viable alternative, and

this chapter provides detail on the ALD process. Various experimental and computational methods to examine and understand ALD are explained while the major knowledge gaps are addressed. Specifically, it is critical to understand how surface chemistry and morphology can be manipulated to form free standing 2D-MoS_2. Various bonds formed between the MoF_6 precursor and surface need to be studies in order to interpret experimental measurements. Furthermore, it remains unclear on how S from the H_2S precursor is deposited. These knowledge gaps can be addressed using DFT-based methods.

Chapter three explains the fundamental physics used in the first-principles calculations, and various methods implemented in this dissertation. This chapter demonstrates how DFT calculations use several assumptions and approximations to simplify the calculations of ground states and properties of materials. DFT-based methods such as the DoS, partial charge densities, Bader charge analysis, and charge density difference are all used in conjunction to understand the nucleation mechanism of MoS_2 during ALD in this research.

Chapter four investigates the electrical and thermal transport properties of lateral TMDs. This chapter focuses on the interface at MoS_2-WX_2 heterostructures where X= S or Se, and aims to understand how transport properties are affected by uniaxial strain testing. The 2D heterostructures underwent pseudo compressive and tensile testing from 0 – 10% at 2% intervals. The electronic and phonon DoS were calculated at each interval and compared with the unstrained heterostructure. Computational results highlighted how sensitive the MoS_2-WX_2 heterostructure interface is to small compressive and tensile forces.

Chapter five examines the effects of surface hydroxylation on three metal oxides (Al_2O_3, HfO_2, and MgO) during ALD of MoS_2. DFT calculations provided partial charge densities, LDoS, Bader charge analysis, adsorption energies, and charge density differences for non-hydroxylated and hydroxylated oxide surfaces. The findings indicated that hydroxyl groups lower the reaction barriers for the first half-cycle of MoF_6 by providing more electrons at the oxide surfaces to promote the reaction. Oxide surfaces without hydroxyls groups demonstrated van der Waals interactions, which are not strong enough for successful ALD. The hydroxylated surfaces promoted the formation of ionic MF_x (M = metal, x = 1, 2, 3) bonds at the oxide surfaces. We found that hydroxyl groups could alter the surface chemistry and provide enough surface electrons to facilitate the formation of strong chemical bonds during the first half-cycle of MoF_6. This chapter reinforces the importance of surface chemistry and how hydroxyl groups could dictate the nucleation of MoS_2 during ALD.

Chapter six combines first-principles and experimental methods to understand the nucleation for ALD of MoS_2 using MoF_6 and H_2S on Al_2O_3. This chapter bridges experimental measurements and computational results to explain the nucleation phenomena that occurs during ALD of MoS_2. QCM, XPS, and RGA measurements were combined with calculated adsorption energies, measured bond lengths, Bader charge analysis, charge density difference, and reaction barriers to validate the formation of ionic AlF_3 during the first half-cycle of MoF_6. The combined methods also uncovered that no gaseous byproducts are formed during MoF_6 exposure confirming the dissociation process. Reaction pathways for H_2S were calculated using the recommended byproducts

discovered in experiment. The results indicated two nucleation mechanisms of MoS_2 that varied between precursors.

Chapter seven contains a variety of research work I contributed to during my PhD candidacy. It includes carbon capture materials, battery anodes, and TMD-related work. I implemented a variety of first-principles methods in collaboration with experimentalists to reveal scientific phenomena. All these studies strengthened my computational and teamwork skills that benefited my PhD research in ALD and future career.

In this dissertation there are two major nucleation conclusions derived from the first-principles calculations. (1) Surface chemistry and morphology can be manipulated with hydroxyl groups to improve or hinder deposition depending on the application. (2) The precursor chemistry of MoF_6 and H_2S has two different nucleation mechanisms depending on the precursor. The first half-cycle of MoF_6 creates no gaseous byproducts and ionic AlF_3 forms on the surface. MoF_6 precursors will dissociate on the surface, and the type of dissociation is dependent on hydroxyl concentration. The second half-cycle of H_2S exhibits ligand-exchange behavior by creating water and HF as byproducts. This dissertation demonstrates that surface chemistry for ALD is not a simple process, and detailed work needs to be done on future chemistries. Simple thermodynamic equations cannot adequately explain nucleation during ALD, and first-principles methods offer a viable alternative. Furthermore, nucleation at the atomic level follows a variety of nucleation mechanisms which must be studied. The different nucleation mechanisms in this dissertation highlight the complexity for ALD of MoS_2.

Future work is predicated on understanding how or when the MoF_6 precursor shifts from dissociation to ligand-exchange. Initial experimental work indicates that in the

growth regime for ALD of MoS_2 the MoF_6 precursor begins to form HF byproducts. Detailed work must be done to understand how many cycles it takes before HF forms as a byproduct of the MoF_6 reaction. Additionally, more work should be done to better understand the second half-cycle of H_2S. More reaction pathways should be considered, and my calculations did not incorporate temperature. First-principles molecular dynamics could uncover important entropic information that occurs at elevated temperatures. Finally, this work could be easily replicated using precursors like WF_6 to deposit WS_2. This future work could compare the nucleation mechanisms between two similar precursors during the ALD of TMDs.

APPENDIX A

Supplementary Information for Chapter 5

First-principles studies of MoF_6 absorption on hydroxylated and non-hydroxylated metal oxide surfaces and implications for atomic layer deposition of MoS_2

Matthew Lawson[1], Elton Graugnard[1], and Lan Li[1,2]

[1]*Micron School of Materials Science and Engineering, Boise State University, Boise, ID 837062*
[2]*Center for Advanced Energy Studies, Idaho Falls, ID 83401*

Optimized Surface Structures

The surfaces used in this study were generated from bulk structures with terminating metal and O atoms. Table A.S1 contains the dimensions for the surfaces. There was no significant change in surface dimensions when hydroxyls groups were added, because the volume of the cell was fixed to maintain a vacuum. Figures A.S1 and A.S2 show the relaxed surfaces without and with hydroxyl groups.

Table A.S1. Dimensions of Al_2O_3, HfO_2, and MgO surfaces

	Al_2O_3	HfO_2	MgO
a (Å)	9.60	10.78	8.36
b (Å)	13.27	14.42	8.36
Surface Area (nm^2)	1.27	1.55	0.70
Vacuum Length (Å)	24.49	20.95	20.44

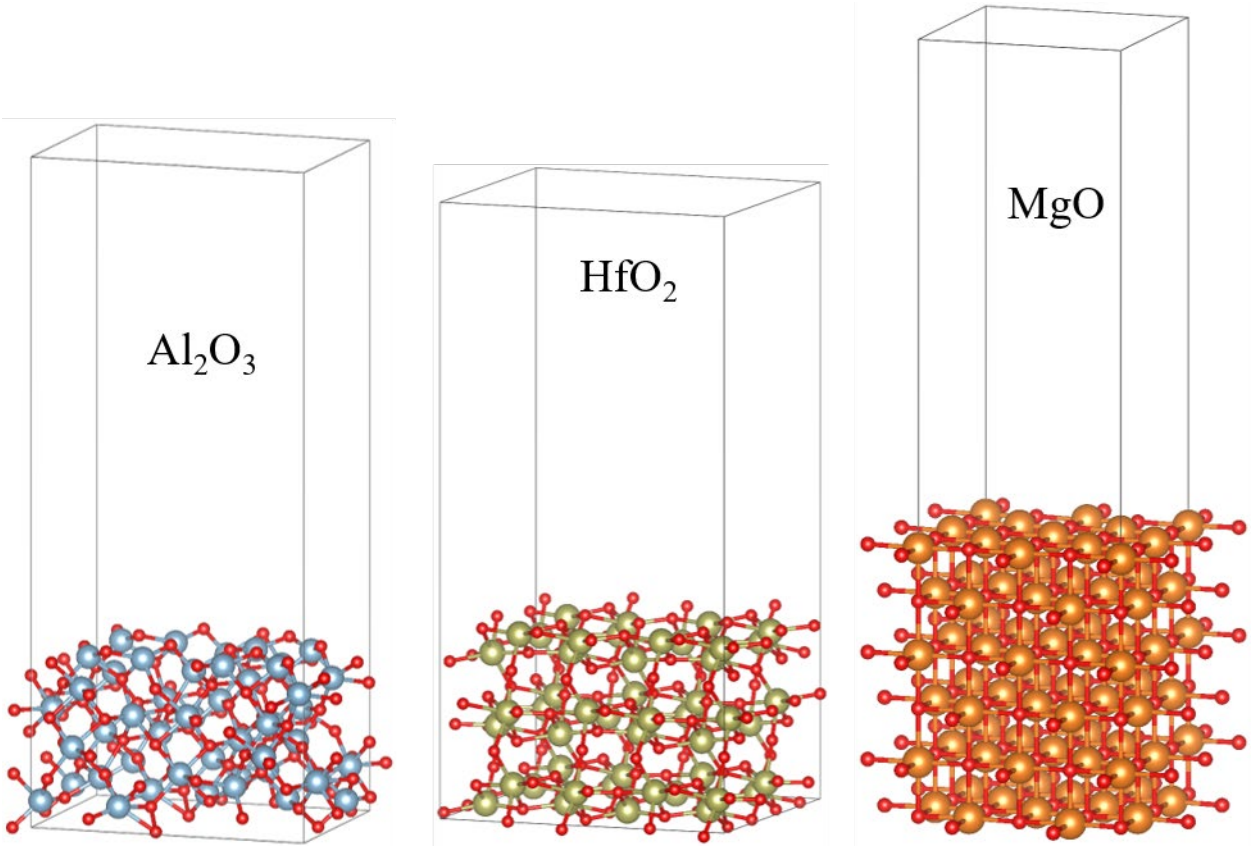

Figure A.S1. Ground-state non-hydroxylated substrates. The blue, yellow, orange, red, and white atoms are Al, Hf, Mg, and O, respectively.

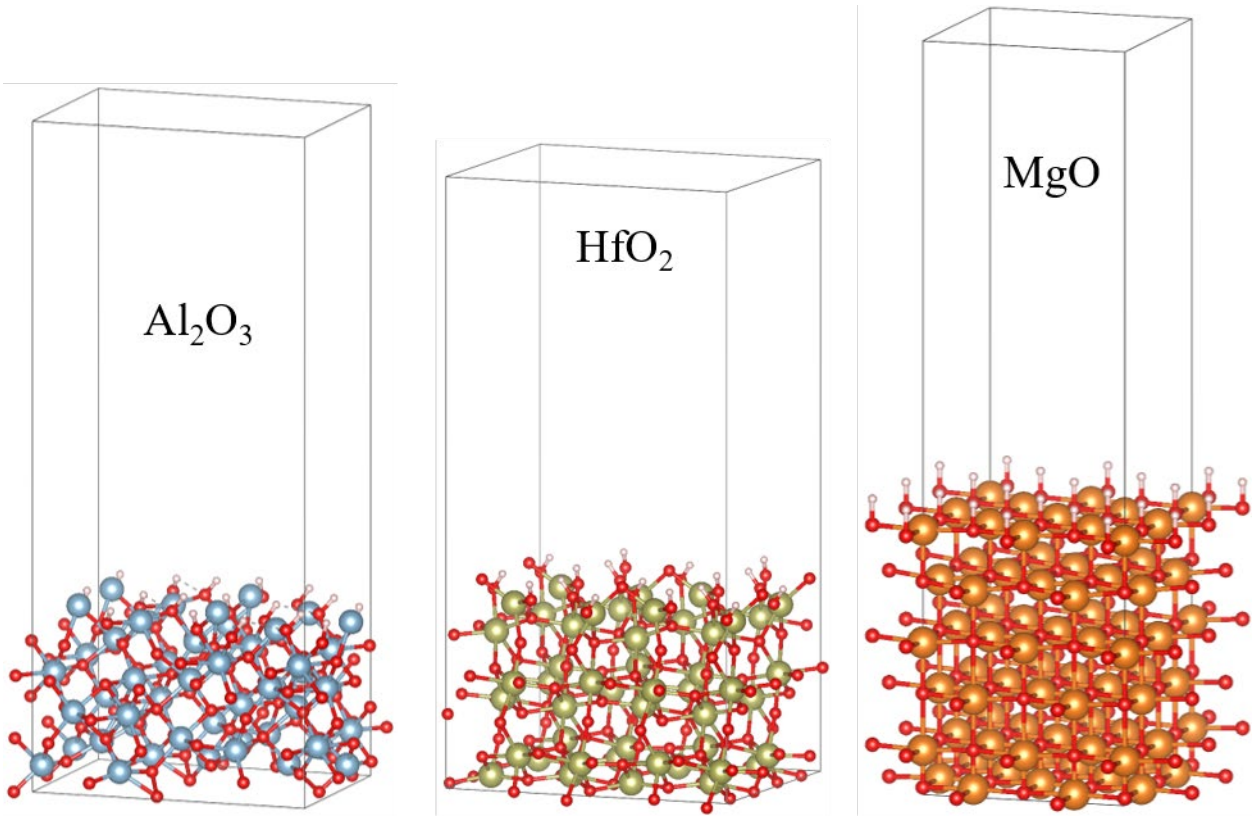

Figure A.S2. Ground-state hydroxylated substrates. The blue, yellow, orange, red, and white atoms are Al, Hf, Mg, O, and H, respectively.

Optimized Surface with MoF_6

A single MoF_6 precursor was added above the relaxed surfaces in Figure A.S1, and the ground state was then calculated. Figures A.S3 and A.S4 show the ground-state of the MoF_6 precursor above the non-hydroxylated and hydroxylated surfaces, respectively. On the non-hydroxylated substrates, the MoF_6 precursor was re-oriented, but it maintained its structure. On the hydroxylated substrates, there were some notable changes. Above the hydroxylated Al_2O_3 surface the MoF_6 precursor lost two F atoms that bonded to Al on the surface while H_2 gas was formed above the hydroxylated MgO surface. Table A.S2 shows the changes in the bond lengths and angles of the MoF_6 precursor on the non-hydroxylated and hydroxylated substrates.

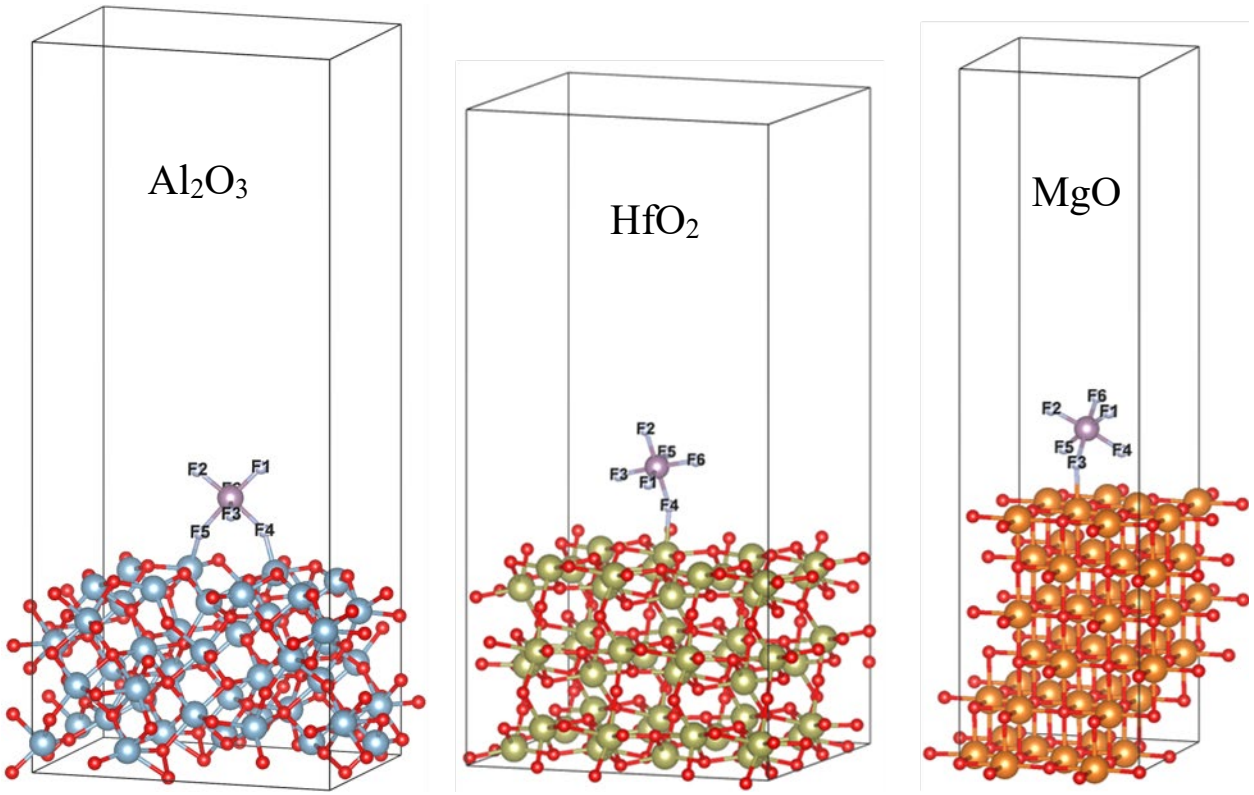

Figure A.S3. Images of MoF_6 deposition on non-hydroxylated. The blue, yellow, orange, red, purple, and teal atoms are Al, Hf, Mg, O, H, Mo, and F, respectively.

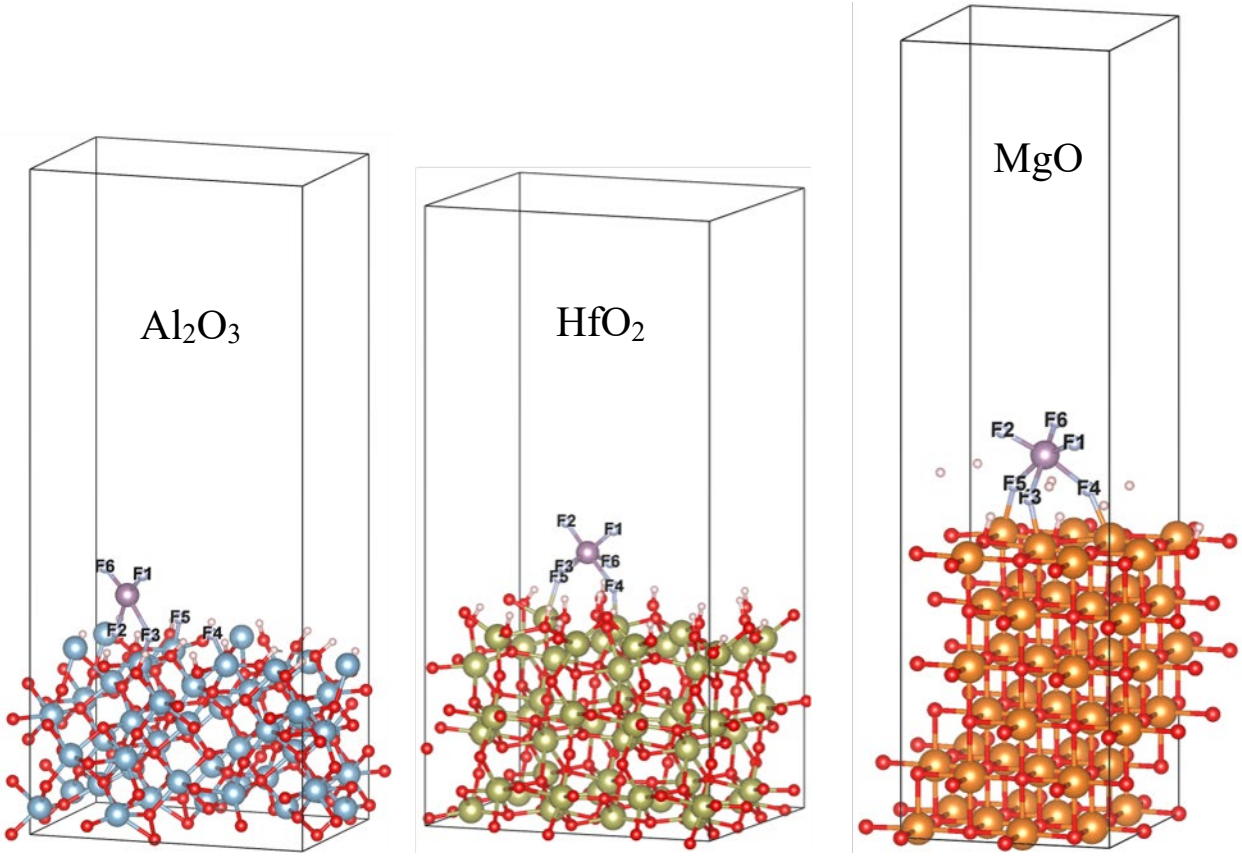

Figure A.S4. Images of MoF_6 deposition on hydroxylated substrates. The blue, yellow, orange, red, white, purple, and teal atoms are Al, Hf, Mg, O, H, Mo, and F, respectively.

Table A.S2. Mo-F bond lengths and F-Mo-F bond angles for MoF_6 on the non-hydroxylated and hydroxylated Al_2O_3, HfO_2, and MgO substrates. Dissociated represents that a F atom is dissociated from MoF_6 and then bonded to the substrate.

	Non-hydroxylated			Hydroxylated		
	Al_2O_3	HfO_2	MgO	Al_2O_3	HfO_2	MgO
Bonds	Bond Lengths (Å)			Bond Lengths (Å)		
Mo-F_1	1.86	1.86	1.87	1.92	1.93	1.89
Mo-F_2	1.86	1.86	1.87	2.29	1.92	1.92
Mo-F_3	1.84	1.88	1.93	2.24	2.04	2.10
Mo-F_4	2.05	1.96	1.91	Dissociated	2.23	2.19
Mo-F_5	2.03	1.87	1.91	Dissociated	2.20	2.10
Mo-F_6	1.85	1.87	1.87	1.92	2.07	1.89
Atoms	Bond Angles (degree)			Bond Angles (degree)		
F_1-Mo-F_2	93.02	91.68	92.03	161.29	95.08	102.61
F_1-Mo-F_3	94.12	91.26	90.19	92.97	100.03	85.56
F_1-Mo-F_4	91.67	88.22	88.93	Dissociated	82.29	82.96
F_1-Mo-F_5	175.53	176.44	176.23	Dissociated	177.37	160.85
F1-Mo-F_6	93.07	89.53	92.11	105.74	101.52	103.72
F_2-Mo-F_3	94.91	91.84	90.18	68.36	103.00	90.87
F_2-Mo-F_4	175.28	179.85	176.17	Dissociated	177.36	171.56
F_2-Mo-F_5	91.28	91.88	88.90	Dissociated	83.86	86.24
F_2-Mo-F_6	94.78	91.79	92.17	92.97	100.18	90.95
F_3-Mo-F_4	85.29	88.28	86.12	Dissociated	77.57	83.19
F_3-Mo-F_5	86.74	88.76	86.15	Dissociated	82.56	77.27
F_3-Mo-F_6	167.60	176.26	176.65	161.05	146.60	169.90

F_4-Mo-F_5	84.02	88.22	89.90	Dissociated	98.77	86.60
F_4-Mo-F_6	84.41	88.09	91.49	Dissociated	80.39	93.88
F_5-Mo-F_6	85.34	90.24	91.51	Dissociated	76.35	92.94

Charge Density Difference Calculations

The charge density difference ρ_{diff} was calculated by taking the charge density of the optimized MoF_6/substrate system $\rho_{total\ system}$ and subtracting the individual charge density contributions of the surface $\rho_{surface}$ and MoF_6 precursor ρ_{MoF_6}:

$$\rho_{diff} = \rho_{total\ system} - \rho_{surface} - \rho_{MoF_6}$$

The resulting figure contains the residual charge density which isolates the electrons participating in adsorption. Figures A.S5, A.S6 and A.S7 show the charge density difference for the non-hydroxylated and hydroxylated MoF_6/substrate systems, where the blue and yellow isosurfaces indicate a gain and loss of electrons respectively.

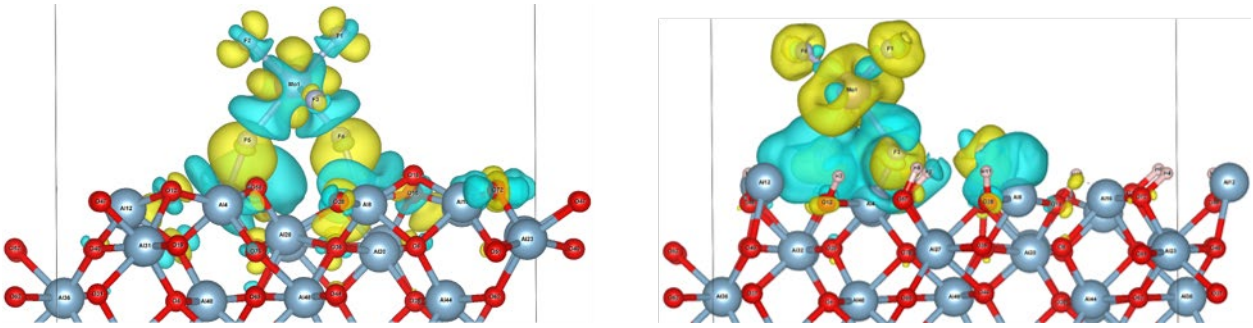

Figure A.S5. Charge density difference for the non-hydroxylated (left) and hydroxylated (right) Al_2O_3 with MoF_6. The yellow and blue regions indicate a loss and gain of electrons, respectively.

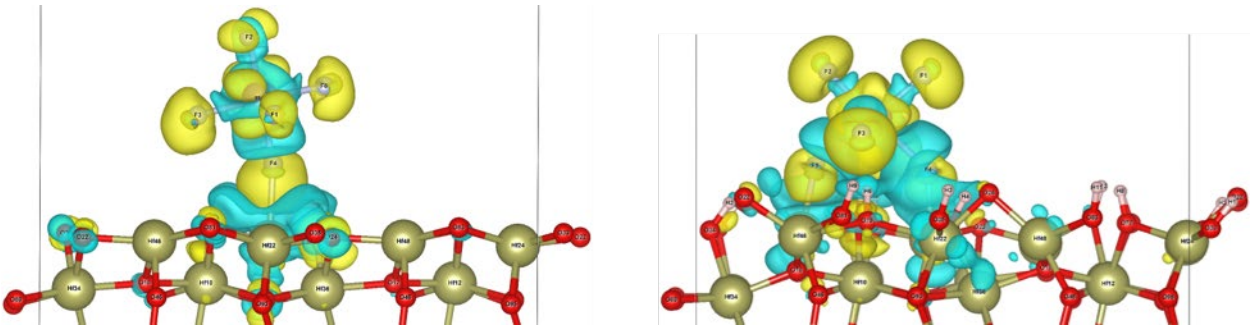

Figure A.S6. Charge density difference for the non-hydroxylated (left) and hydroxylated (right) HfO_2 with MoF_6. The yellow and blue regions indicate a loss and gain of electrons, respectively.

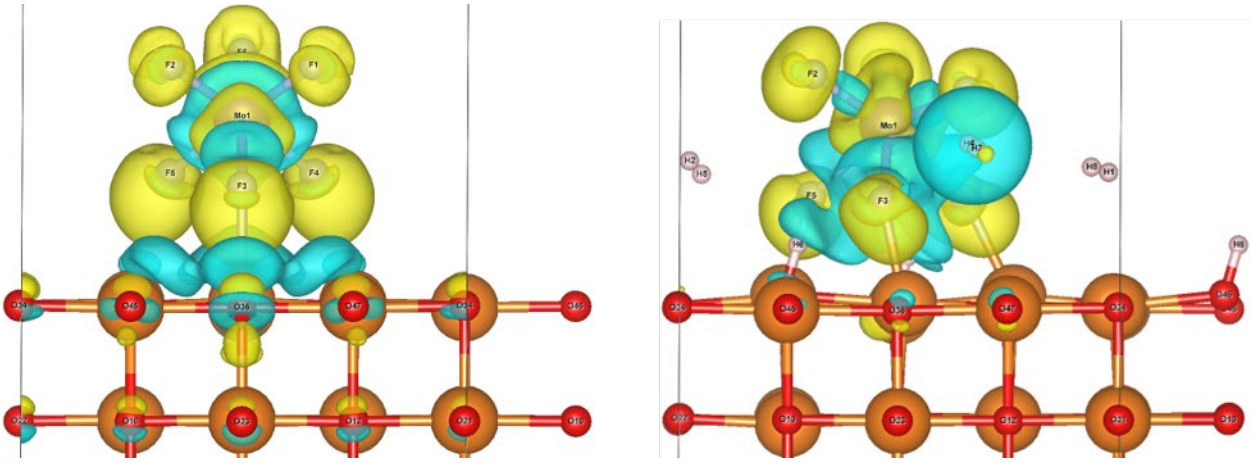

Figure A.S7. Charge density difference for the non-hydroxylated (left) and hydroxylated (right) MgO with MoF_6. The yellow and blue regions indicate a loss and gain of electrons, respectively.

APPENDIX B

Supplementary Information for Chapter 6

Understanding ALD-grown MoS_2 by combining experimental measurements and first-principles calculations

Matthew Lawson[1], Jake Soares[1], Sean Martin[1], Elton Graugnard[1] and Lan Li[1,2]

[1]*Micron School of Materials Science and Engineering, Boise State University, Boise, ID 837062*
[2]*Center for Advanced Energy Studies, Idaho Falls, ID 83401*

Examples of hydroxylated surfaces

Figure B.S1 contains three example alumina morphologies with a hydroxyl concentration of 6.4 OH/nm^2. From the surfaces it is possible to see the differences in locations of the hydroxyl groups. The locations were randomized and the all the subsequent data (adsorption energies, bond lengths, and Bader charge) was average to mitigate anomalies. These anomalies could stem from localized effects, such as two hydroxyl groups located close to each other. The surface areas and vacuum lengths remained constant throughout the different morphologies.

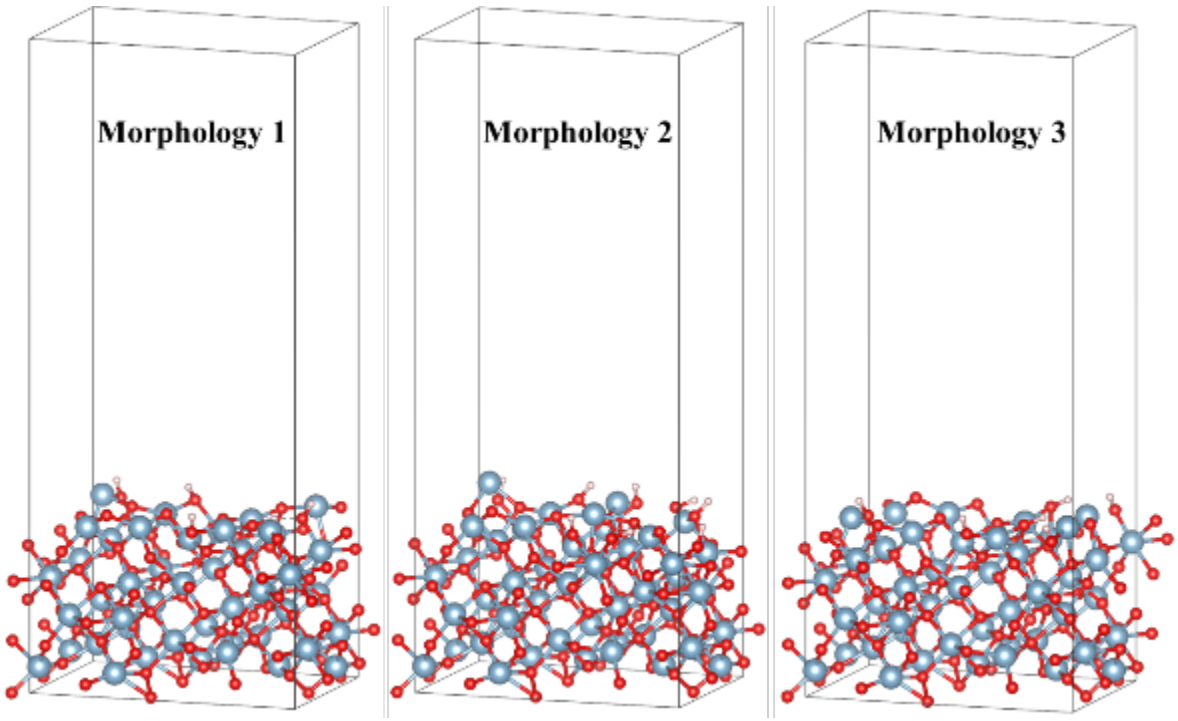

Figure B.S1. Atomic structures of the hydroxylated alumina surfaces demonstrating the three different morphologies at the same hydroxyl concentration.